PHOTONUCLEAR STUDIES OF ^{241}Am BETWEEN 5 AND 10 MeV

S. J. Watson

Thesis submitted for the degree of Doctor of Philosophy

University of Edinburgh

1990

Ars longa vita brevis

Abstract

The ^{241}Am photofission and photoneutron cross section, the mean number of prompt neutrons per fission $\bar{\nu}$ and the delayed neutron yield have been measured between 5 and 10 MeV. The photofission cross section has been measured over a wider range and with better resolution than any previous data. The photoneutron cross section, $\bar{\nu}$ and the delayed neutron yield had not been measured before.

The experiment was performed using bremsstrahlung radiation produced by the 136 MeV Harwell electron linac HELIOS. Fission neutrons and photoneutrons from the ^{241}Am target were detected by an oil-moderated tank containing fifty-six $^{10}BF_3$ proportional counters arranged in five concentric rings. For each run, the events associated with each beam burst were recorded as a multiplicity distribution. The end-point energy was cycled between two neighbouring energy points during the run to give difference yields in order to minimise the effects of energy drifting.

The data were corrected, fitted and bremsstrahlung unfolded to give both the photofission and photoneutron cross sections as well as $\bar{\nu}$ and an upper limit for the delayed neutron yield. The results were then compared with other data.

Calculations were performed to see if any resonances might be present close to the fission threshold. Some calculated structure was indicated at 6.0 MeV. A suggestion of a change in slope in the experimental data was observed at this energy but there is no evidence for any other structure because of the statistical scatter of the data. Cross sections were also calculated for the other actinides studied experimentally at Harwell, namely ^{232}Th and ^{238}U.

Acknowledgements

The work that I have carried out would not have been possible without the help of many people in and around Building 418, Harwell Laboratory and Edinburgh University. Most of all, I would like to thank my Harwell supervisor Dr. David Findlay for his expertise and guidance in all matters throughout the three years of this project and for helping to run the experiment. Thanks also to Dr. Martyn Sené for advice (moral and otherwise) and help in running the experiment; likewise to Mark Bailey.

I am very grateful to Dave Webb for his help in solving various computing problems with tireless efficiency. Many thanks are due to all the shift teams on the Harwell electron linac, past and present, and the project engineer, Dr. John Down who have provided beam in the most difficult of circumstances. I should also like to extend my thanks to all the workshop and engineering staff who have never failed to produce items of equipment of the highest quality without which the experiment would have been made very difficult.

I am most grateful to Dr. Birger B. Back for providing me with information concerning the quasi-particle states of ^{241}Am.

Thanks must also go to Dr. A.T.G. Ferguson and Dr. M.S. Coates for giving me the opportunity to carry out my research work at Harwell. Finally, I am grateful to Prof. A.C. Shotter for his interest and support in the project.

Contents

1 Introduction 11

1.1 A Brief History of Fission 11

1.1.1 The Liquid Drop Model 11

1.1.2 Influence of the Shell Model 12

1.1.3 Symmetric and Asymmetric Deformations 16

1.2 Rationale Behind Photon-Induced Fission 17

1.2.1 A Comparison of Various Fission Inducing Reactions . 17

1.2.2 Producing γ-rays for Use in Photonuclear Studies . . . 18

1.2.3 The Channel Theory of Fission 20

1.3 The Layout of this Thesis 20

2 Experimental Method 23

2.1 The Purpose of the Experiment 23

2.2 A Résumé of the Experiment 23

2.3 The Linac 24

2.3.1 The Low Energy Line 24

2.4 The Target 29

2.4.1 General Description 29

2.4.2 The Target Mounting 29

2.4.3 Analysis of the Target 32

2.5 The Detector 39

2.5.1 The Detector Electronics 41

2.5.2 The Detector Response 45

2.6 The P2 Chamber 47

2.7 Experimental Running 49
2.7.1 Two-Energy Magnet Cycling 49
2.7.2 Data Acquisition 52
2.7.3 The P2 Background 55
2.7.4 Data Collection Inhibits 56
2.7.5 Energy Calibration 56
2.7.6 Magnet Field Stabilisation 58
2.7.7 The Effect of the γ-Flash 58
2.7.8 The Background 58
2.7.9 Typical Signal-to-Noise Rates 59

3 Analysis **64**
3.1 An Outline of the Analysis 64
3.2 Details of the Corrections 66
3.2.1 Philosophy of the Corrections 66
3.2.2 Background Correction 66
3.2.3 Dead-Time Correction 68
3.2.4 Overlap Correction 69
3.2.5 Atmospheric Correction to P2 Chamber Response . . . 70
3.2.6 Target Attenuation of Beam 71
3.2.7 Effective Target Thickness 72
3.3 Calculating the Errors 73
3.4 Fitting the Data 73
3.4.1 The Terrell Distribution 74
3.4.2 The Truncated Renormalised Gaussian Distribution . . 76
3.4.3 The Truncated Renormalised Double Gaussian Distribution 76
3.4.4 Efficiency Correcting the TRDG 77
3.4.5 Data Fitting 78
3.4.6 Errors on the Fits 79
3.4.7 Fixing Parameters During Fits 79

3.4.8 Calculating $\overline{\nu}$, the Number of Fissions and the Number of Photoneutron Events 79
3.5 Unfolding the Cross Sections 81
3.5.1 The Shape of the Bremsstrahlung Spectrum 82
3.5.2 The Mathematics of Unfolding 82
3.5.3 Unfolding the Energy Pair Data 88
3.5.4 Anomalies in Unfolding when Starting from Different Yield Points 88
3.5.5 Interlacing Data Runs 89
3.5.6 Normalisation of Yields 90
3.6 The Delayed Neutron Yield 90
3.6.1 A Description of Delayed Neutrons and their Importance 90
3.6.2 Detection of the Delayed Neutrons 92
3.6.3 Calculation of the Delayed Neutron Yield 92

4 Results **96**
4.1 A Summary 96
4.2 The Results for $\sigma_{\gamma f}$, $\sigma_{\gamma n}$, $\overline{\nu}$ and the Delayed Neutron Yield . . . 96
4.2.1 $\sigma_{\gamma f}$ 96
4.2.2 $\sigma_{\gamma n}$ 105
4.2.3 $\overline{\nu}$ 107
4.2.4 The Delayed Neutron Yield 109

5 Theory **112**
5.1 Introduction 112
5.2 The Fission Process 112
5.2.1 Decay of an Excited Actinide Nucleus 112
5.2.2 The Compound Nucleus 114
5.2.3 Low-Lying Even-Even Nuclei Fission Channels 115
5.2.4 Low-Lying Odd-Even Nuclei Fission Channels 117
5.2.5 Fission Channels Above the Pairing Gap 120
5.2.6 A Note on the Addition of Fission Channels 123

5.2.7 Barrier Penetration 124
5.2.8 Structure in the Cross Section 126
5.2.9 The Complete Damping Limit 132
5.2.10 Photon Absorption Cross Section 132
5.2.11 The γ Transmission Coefficient 134
5.2.12 The Neutron Transmission Coefficient 135
5.3 Modelling the Cross Sections 137
5.3.1 ^{232}Th Photofission Cross Section 137
5.3.2 ^{238}U Photofission Cross Section 141
5.3.3 ^{241}Am Photofission Cross Section 144

6 Conclusions and Discussions **150**
6.1 The Experimental Set-up 150
6.2 The Measured Cross Sections 151
6.2.1 The Photofission Cross Section 151
6.2.2 The Photoneutron Cross Section 152
6.2.3 $\overline{\nu}$ 154
6.3 Fission Barrier Analysis 155
6.3.1 The Shape of the Fission Barrier 155
6.3.2 The Damping of Resonances 156
6.3.3 The Density of States at the Saddle Point and in the Residual $A-1$ Nucleus 156
6.3.4 Normalisation of the Calculated Cross Sections 157

A Tabulations of the Experimental Data **158**
A.1 The $\sigma_{\gamma f}$ Cross Sections 158
A.2 The $\sigma_{\gamma n}$ Cross Sections 158
A.3 The $\overline{\nu}$ Data 160

Bibliography **165**

List of Figures

1.1 Potential energy contours as a function of quadrupole(β_2) and hexadecapole(β_4) deformations. 13
1.2 Potential energy of the nucleus as a function of deformation. . 13
1.3 Shell correction potential. 15
1.4 Sum of LDM potential and shell correction potential. 15
1.5 Split in the GDR for the deformed nucleus ^{238}U [Berm 75]. . . 21
1.6 The relative intensities of compound nuclear angular momenta excited by various reactions [Zhuc 78]. 22

2.1 HELIOS:The Harwell Electron Linear accelerator for the Investigation Of neutron and radiation Science. 25
2.2 Electrons being accelerated by a travelling wave. 27
2.3 The Low Energy line. 28
2.4 γ-spectrum of ^{241}Am Target. 33
2.5 The set-up to produce a T.A.C. spectrum. 36
2.6 T.A.C. spectrum from ^{241}Am/B source. 37
2.7 T.A.C. spectrum from ^{241}Am target. 38
2.8 The "lead pin-hole camera." 38
2.9 The film after exposure to the ^{241}Am target. 39
2.10 Schematic of the neutron detector. 42
2.11 The detector electronics. 43
2.12 A typical pulse height spectrum for a ring of $^{10}BF_3$ counters. . 44
2.13 The gates used to detect neutron pulses. 45
2.14 The efficiency of the detector. 46
2.15 The capture time distribution. 48

2.16 Drift in the yield for two different energies. 50

2.17 Drift in the yield for two different energies a fixed distance apart. 51

2.18 The magnet set-up. 53

2.19 A beam energy calibration graph. 57

3.1 The bremsstrahlung spectrum calculated by Tseng and Pratt (dotted line) and Findlay (solid line). 83

3.2 Oscillations in the Penfold-Leiss weighting function as the function is forced to go through the midpoint of each bin between i and $i+1$. 86

3.3 The bremsstrahlung weighting function with λ factor changed from 1/2 to 3/2. 87

3.4 Fission fragment decay towards the Z-N stability curve (schematic representation). 91

3.5 The change in the background count rate with increasing net spectrum count rate. 93

4.1 The photofission cross section from the '88 data. 97

4.2 The photofission cross section between 5.6 and 8.0 MeV from the '88 data. 98

4.3 The photofission cross section between 5.6 and 8.0 MeV from the '90 data. 99

4.4 The raw yield differences from the 50 keV data. 101

4.5 The photofission cross section from the 50 keV data. 102

4.6 The photofission cross section from the '88 data compared with Zhuchko *et al.* 103

4.7 The photofission cross section from the '90 data compared with Zhuchko *et al.* 104

4.8 The fissility from the '88 data compared with that of Zhuchko *et al.* and Back *et al.* 106

4.9 The photoneutron cross section obtained from the '88 and '90 data. 107
4.10 $\overline{\nu}$ obtained from the '88 and '90 data. 109
4.11 Comparison of the delayed neutron yield of ^{241}Am with other actinides. 111

5.1 Competing processes in the decay of an excited actinide nucleus. 113
5.2 K: The projection of J onto the fission axis. 116
5.3 The spectrum of fission channels for an even-even nucleus. . . 116
5.4 Proton single-particle levels. 118
5.5 Neutron single-particle levels. 119
5.6 Spectrum of fission channels for ^{241}Am. 121
5.7 Comparison of a continuous level density approximation with discrete low-lying levels for ^{241}Am[Back 74b]. 122
5.8 A potential step. 125
5.9 Barrier approximated by steps. 126
5.10 A double-humped barrier. 127
5.11 Transmission of the barrier in Fig. 5.10. 128
5.12 Imaginary potential in the second well to emulate damping. . 129
5.13 Comparison of double-humped barrier transmission with 50 keV damping (full curve) and without damping (dashed curve). . . 131
5.14 The tail of the GDR compared with experimental photon elastic scattering cross section for ^{238}U. 133
5.15 Decay of a nucleus of mass A by neutron emission. 136
5.16 The ^{232}Th cross section compared with Harwell data [Find 86]. 139
5.17 As Fig. 5.16 but the theoretical cross section has 80 keV smearing. 140
5.18 The ^{238}U cross section compared with Harwell data [Find 87]. 142
5.19 As Fig. 5.18 but the theoretical cross section has 80 keV smearing. 143
5.20 The ^{241}Am cross section compared with Harwell '88/'90 data and the Zhuchko data [Zhuc 78]. 146

5.21 As Fig. 5.20 but the theoretical cross section has 220 keV smearing. 147

5.22 As Fig. 5.20 but with uniform damping of 300 keV in the second well (W_{im0}=300 keV, W_{im1}=0 keV). 148

5.23 As Fig. 5.22 but the theoretical cross section has 220 keV smearing. 149

5.24 *Possible* resonances in the Zhuchko data. 149

6.1 Neutron emission to fission width plotted as a function of fissionability. The present data point is an average of data at bremsstrahlung end-points between 8 and 10 MeV. 153

6.2 Neutron emission to fission width plotted as a function of mass number. The present data point is shown as a solid triangle with error bars. 154

List of Tables

2.1 The accelerator specifications. 26

2.2 Operating conditions for the present experiment. 26

2.3 Spark source mass spectrographic analysis of high purity americium oxide used for americium metal preparation. . . . 30

2.4 Spark source spectrographic analysis of americium metal prepared by reduction-distillation process. 31

3.1 The resolutions appropriate to each value of λ used to unfold in the present experiment. 85

5.1 Energies of low-lying even-even fission channels above ground state barrier. 120

5.2 Parameters used to generate the ^{232}Th cross section. 138

5.3 Fission barriers used to generate the ^{232}Th cross section. . . . 138

5.4 Parameters used to generate the ^{238}U cross section. 141

5.5 Fission barriers used to generate the ^{238}U cross section. 142

5.6 Parameters used to generate the ^{241}Am cross section. 144

5.7 Fission barriers used to generate the ^{241}Am cross section. . . . 145

A.1 The $\sigma_{\gamma f}$ 100 keV data (2-fold interlaced) 159

A.2 The '90 $\sigma_{\gamma f}$ 50 keV data (2-fold interlaced) 161

A.3 The $\sigma_{\gamma n}$ 100 keV data (2-fold interlaced) 162

A.4 The 100 keV $\overline{\nu}$ data 163

A.5 The '90 $\overline{\nu}$ 50 keV data 164

A.6 The '88 $\overline{\nu}$ 500 keV data 164

List of Plates

1 The target can 60
2 An inside view of the detector 61
3 The 56 $^{10}BF_3$ counters 62
4 The detector with the P2 chamber in position. 63

Chapter 1

Introduction

1.1 A Brief History of Fission

Since the discovery of fission in the 1930's, many questions about the behaviour of the nucleonic system remain unanswered. Due to the many-bodied nature of the nucleus, one can only make an approximation to the systematics of a nucleus torn into two, governed by the competing electromagnetic and strong interactions.

1.1.1 The Liquid Drop Model

One of the first attempts to begin explaining the radical behaviour of fission was made by Meitner and Frisch [Meit 39] in 1939. They proposed that the nucleus be thought of in terms of a drop of liquid: just as an unstable drop of water can fragment into two or more droplets,[1] so a drop of unstable "nuclear fluid" might split or *fission* into two or more fragments. This idea was taken up by Bohr and Wheeler [Bohr 39] who studied it in great detail.

The liquid drop model (henceforth referred to as the LDM) describes the potential energy associated with the deformation of the nuclear fluid due to the competition between "surface tension" and Coulomb effects. By studying

[1]Indeed, as long ago as 1878, Lord Rayleigh [Rayl 78] showed that a long homogeneous liquid jet, confined by surface tension, is unstable with respect to droplet formation.

different drop shapes described by a series of Legendre polynomials,

$$R(\theta) = \frac{R_0}{\lambda}[1 + \sum_{n=1}^{\infty} \beta_n P_n(\cos\theta)] \quad (1)$$

(λ being a volume normalisation term.)

one should be able to investigate the potential energy paths to fission and hopefully gain insight into fission barrier parameters (*eg.* height and curvature). In practice, only the terms involving $n = 2$ and $n = 4$ are considered, higher terms being neglected.

Liquid drop deformations have been studied in great detail for fissility parameters,

$$X = \frac{E_{Coulomb}}{2E_{Surface}} \sim 0.7 - 0.8 \quad (2)$$

where a value of $X > 1$ indicates instability for a spherical liquid drop. Fig. 1.1 (adapted from Bjørnholm and Lynn [Bjor 80]) shows the potential energy contour surface for two of the most important deformation parameters, β_2 and β_4. The path to fission is shown with the highest barrier point or *saddle* denoted "S". The figure below (Fig. 1.2) shows the associated potential energy along the path to fission as a function of elongation of the nucleus. Myers and Swiatecki [Myer 69] and Myers [Myer 77] produced a very comprehensive description of nuclear properties within the framework of the LDM.

1.1.2 Influence of the Shell Model

However, problems with this simple formalism started to become apparent: the discovery of fissioning *isomers* - excited states of nuclei which stay in these excited states for a very long time compared with the nuclear transition time before fissioning (Polikanov *et al.* [Poli 62] and Flerov and Polikanov [Fler 64]); the observation of intermediate structure in the fission cross-section; and the inexplicable tendency to asymmetric fission for the actinides - all deformations of the LDM suggest that fission should be symmetric.

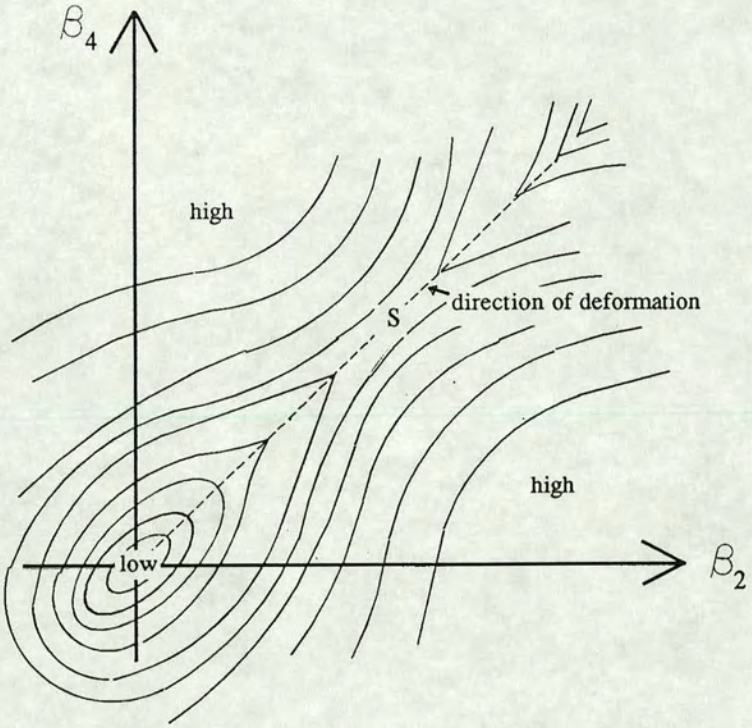

Figure 1.1: Potential energy contours as a function of quadrupole(β_2) and hexadecapole(β_4) deformations.

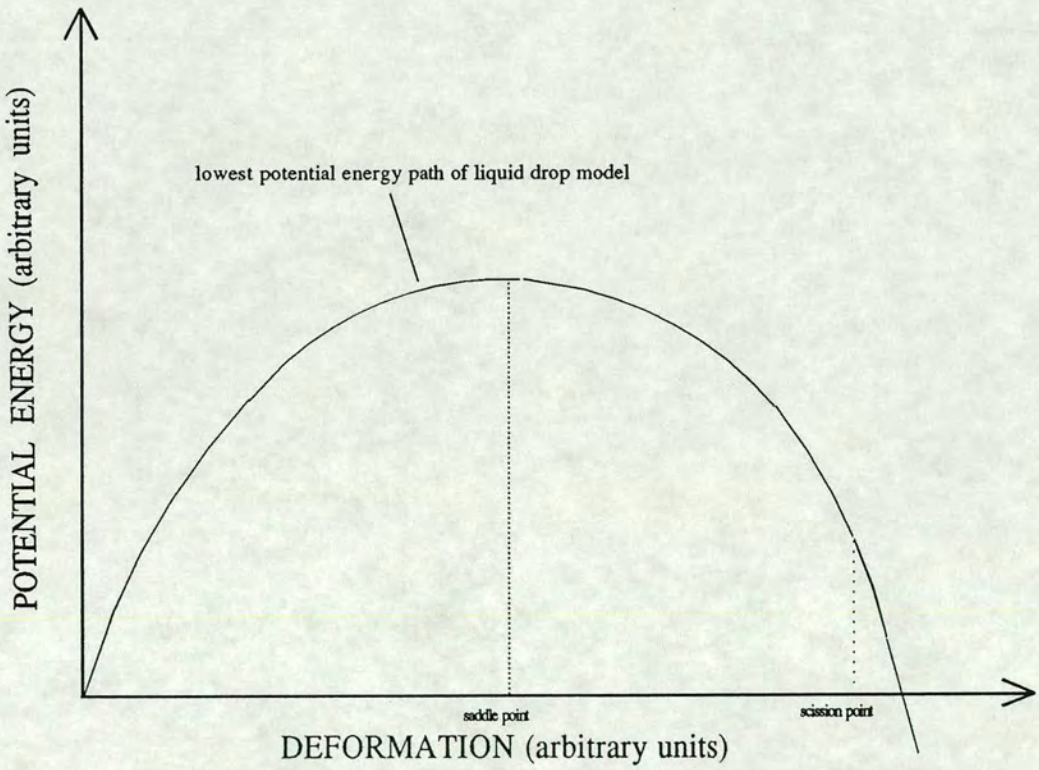

Figure 1.2: Potential energy of the nucleus as a function of deformation.

The next great advance to help explain these so-called anomalies came from Strutinsky [Stru 67] with the shell correction method. Just as atomic orbital shells are present in atoms due to the quantum mechanical effect of electrons under the influence of a central force so, he proposed, nucleons are bound in shells in the nucleus though the central force approximation here is much less accurate. Strutinsky suggested that the shell non-uniformities do not "wash out" in deformed nuclei, but play a major part in determining the path to fission. He proposed a correction of the form,

$$\delta U(N, \beta) = U(\beta) - \tilde{U}(\beta) \tag{3}$$

for N nucleons where U is the sum over ν of the single particle energies E_ν for a given deformation, β, of the average potential,

$$U \overset{E_\nu<\tilde{\lambda}}{=} \sum_\nu 2E_\nu(\beta). \tag{4}$$

and the term subtracted off to correct for the difficulty of ensuring self-consistency of bulk nucleon distribution over a large range of deformations, is $\tilde{U}$ of the form,

$$\tilde{U} = 2\int_{-\infty}^{\tilde{\lambda}} E\tilde{g}(E, \beta)dE \tag{5}$$

where $\tilde{g}(E, \beta)$ is the corrected, smoothed shell-density function and $\tilde{\lambda}$ is the Fermi energy. This shell correction potential has an undulating form as in Fig. 1.3, which when superimposed on the LDM potential gives a barrier of the form shown in Fig. 1.4. As a minimum occurs for the shell correction at approximately the saddle point of the LDM potential, the saddle is split into two and a second well is created giving rise to the so-called *double-humped* fission barrier.

This immediately gave an answer to the question of fissioning isomers in the form of excited states lodged in the second well. These are relatively stable to decay to the inner well due to the existence of the first hump but can tunnel through the second hump as a form of delayed fission. Furthermore, the position of the inner well in deformation space for heavy elements suggests that the nuclide is in a ground state with a permanently

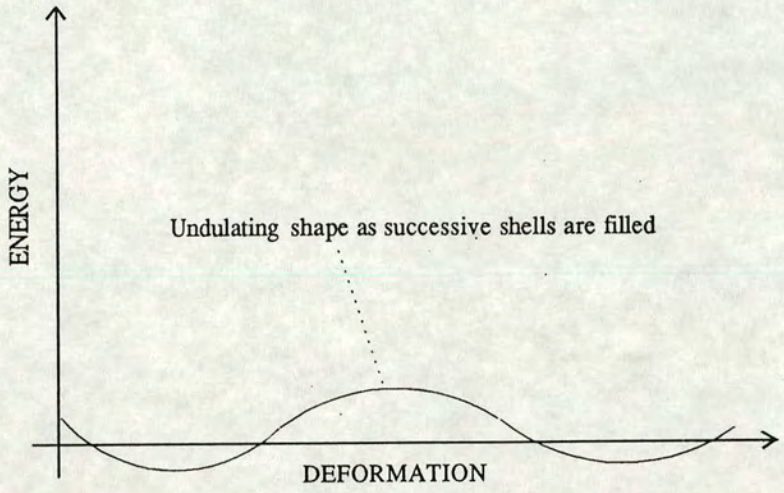

Figure 1.3: Shell correction potential.

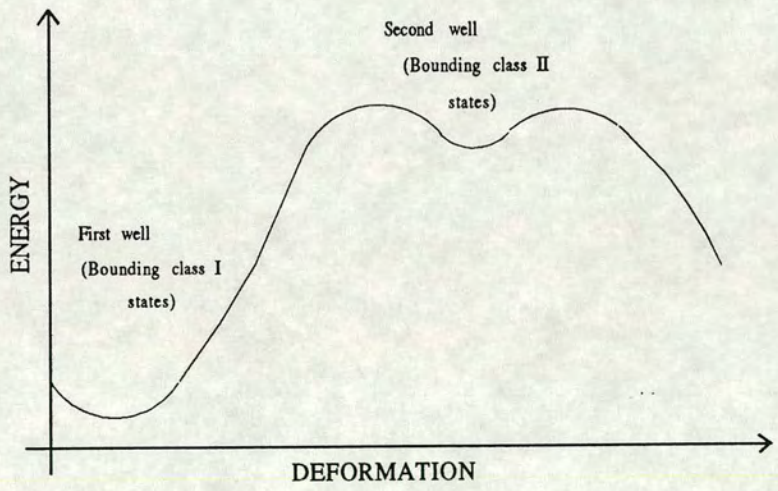

Figure 1.4: Sum of LDM potential and shell correction potential.

deformed shape which explains both the rotational energy levels seen in the even-even nuclei and the splitting of the *Giant Dipole Resonance*, or GDR, into two humps (see Fig. 1.5). Goldhaber and Teller [Gold 48] proposed that the GDR arises from the collective motion of neutron and proton "fluids" with respect to one another, under the influence of a restoring force, giving rise to an electric dipole moment. However, for a deformed nucleus, this collective oscillation can occur along the major or minor axis with different characteristic frequencies, hence the split shown in Fig. 1.5. The double hump also explains the existence of intermediate structure seen in fission cross-sections by suggesting coupling between states in the first and second wells.

1.1.3 Symmetric and Asymmetric Deformations

However, calculations allowing only symmetric deformations consistently over-estimate the heights of the fission barriers. But in 1969, Pashkevich [Pash 69] investigated axially asymmetric deformations. Work done by him and Larsson *et al.* [Lars 72], Schultheiss and Schultheiss [Schu 71] and Larsson and Leander [Lars 74] suggested that the inner barrier was γ deformed and allowing axial asymmetry at the inner barrier lowered the barrier height and gave a value more consistent with experiment.

Work done by Möller and Nilsson [Moll 70] and by Möller [Moll 72] suggested that the outer barrier is unstable with respect to reflection or mass asymmetry, which went some way towards explaining the asymmetric fission seen in many nuclei.

Furthermore, the inclusion of asymmetric deformations suggested a third shallow well in certain actinides, notably thorium, explaining the weakly damped sub-barrier resonances in the fission probability (observed by Back *et al.* [Back 72]) which could not be explained by just two deep wells. This was studied by such groups as Bellia *et al.* [Bell 79, Bell 82], Blons *et al.* [Blon 86], Caruana *et al.* [Caru 77], Lancman [Lanc 84] and Zhang [Zhan 84, Zhan 86].

The fission of nuclides with an even number of protons Z and neutrons N has been studied in much detail, particularly ^{232}Th and ^{238}U. Recent experiments at Harwell have been conducted studying these nuclides by Findlay *et al.* [Find 86, Find 87] however, there is much less information on the behaviour of Z-odd, N-even actinide nuclides such as ^{237}Np and ^{241}Am.

1.2 Rationale Behind Photon-Induced Fission

1.2.1 A Comparison of Various Fission Inducing Reactions

Fission can be induced by basically two methods: particle induced fission *e.g.* (p, f), (n, f) or photon induced fission in the form of virtual photons (electrofission) or, as used in the present experiment, real photons (photofission). Particle induced fission allows one to measure parameters at a specific incident particle energy for a wide energy range with high resolution. However, results are more difficult to interpret due to the varied spins of the particles involved. Fig. 1.6 shows the relative intensities of the fission channel multipoles excited by different probes showing quite clearly the selectivity of the photon. Furthermore, if one wanted to study fission of ^{241}Am by neutron induced fission one would have to start with a target of ^{240}Am which has a half-life of 50.8 hours. Clearly, this is not feasible. Also, neutron induced fission only allows one to study the fission barrier above the neutron emission threshold. Using charged particle induced fission on a long lived nuclide (such as employed by Back *et al.* [Back 74b]) which results in ^{241}Am fission has inherent problems with competing reactions and charged particle break-up. Photofission avoids these problems.

Photofission can give results which are easier to interpret because, dipole (E1) fission predominates (as the wavelength of the incoming radiation is large compared with the radius of the nucleus [2]). (In some circumstances

[2] *e.g.* a 7 MeV photon has a wavelength of 177 fm whereas the radius of ^{241}Am is 7.8 fm.

quadrupole (E2) fission has to be considered). However, a high intensity monoenergetic γ-ray source is difficult to find.

1.2.2 Producing γ-rays for Use in Photonuclear Studies

Photonuclear experiments are done using γ-rays from various sources including:

Neutron capture γ-rays This method is used in fine resolution work due to the narrow width of the γ-rays produced in the (n, γ) reaction. A number of targets need to be used to produce a range of γ-rays as each target produces a discrete range of photons, the relative intensities of which need to be known in order to unfold the results. Although this method is useful for identifying tightly bunched levels in the first well of the fission barrier, care must be exercised when comparing results with broader resolution results as the (n, γ) photons may be on or off resonance whereas broader resolution γ-rays average over a number of resonances.

Proton capture γ-rays A variation of the above using the (p, γ) reaction producing a different range of γ-rays.

e^+e^- γ-rays This is an intermediate resolution technique using annihilation γ-rays and has the advantage of being infinitely adjustable. Positrons are produced by bombarding a converter target with electrons. These can then be accelerated before being analysed using a magnet spectrometer and collimated onto a low-Z target such as Be producing quasi-chromatic annihilation photons. The technique is limited by the resolution of the positrons, the thickness of the annihilation target and the presence of bremsstrahlung produced when the positrons are slowed down in the annihilation target.

Bremsstrahlung γ-rays The method most often used and the one used in this experiment to perform photonuclear experiments, due to its

high intensity and infinite energy adjustability is bremsstrahlung production. This method is achieved by bombarding a high Z target (the intensity of γ-rays is proportional to Z^2/A) with energy analysed and collimated electrons from an accelerator. The electrons are slowed down or stopped in the radiator target producing a spectrum of γ-rays with energies up to the energy of the incident electron beam. This technique is used for broad resolution work as the spectrum of γ-rays averages over many levels and it allows the study of broad resonances caused by levels in the second well of the fission barrier. The main drawback of this method is the need to unfold the continuum of γ-rays from the resultant yields in order to obtain the cross section as a function of monochromatic energy. One way of getting round this at the expense of the beam intensity, is to "tag" the photons. That is to say, the electrons which have passed through the radiator are energy analysed using a spectrometer and detected in coincidence with the photonuclear events. The energy k of the photon for an event is then simply given by:

$$k = E_e - E_e' \tag{6}$$

where E_e is the energy of the electrons incident on the radiator and E_e' is the energy of the electron detected in coincidence with the photonuclear event.

Laser backscattered photons This involves the Compton scattering of a laser beam of relatively low energy photons by high energy electrons to give quite high energy photons. The advantage of this method is that it produces, with suitable collimation, a very high resolution photon beam uncontaminated with bremsstrahlung, although of a much lower energy than the electrons.

1.2.3 The Channel Theory of Fission

It is the selectivity in multipole components from photon induced reactions which is so useful in understanding fission. Bohr [Bohr 56] proposed, in 1956, his channel theory of fission. That is to say, fission takes place via a number of discrete states or *channels*. Furthermore, he stated that these states resembled those of a thermodynamically "cold" nucleus near its ground state as most of the excitation energy is tied up as deformation energy. Hence, if one can select just one or two of these low-lying states, one should be able to deduce information about the shape of the fission barrier for these channels. It is with this thought in mind that the current experiment and others like it have been undertaken.

1.3 The Layout of this Thesis

Chapter 2 details the experimental set-up used to collect the data. The analysis of the data to produce the final cross sections *etc.* is detailed in Chapter 3. The cross sections are presented and analysed in the next chapter and Chapter 5 presents the theory of fission cross sections along with fits to the present data plus two other actinides. Finally, Chapter 6 details the conclusions and discussions for further work. The actual numbers used to produce the graphs in the Results chapter are given in Appendix A.

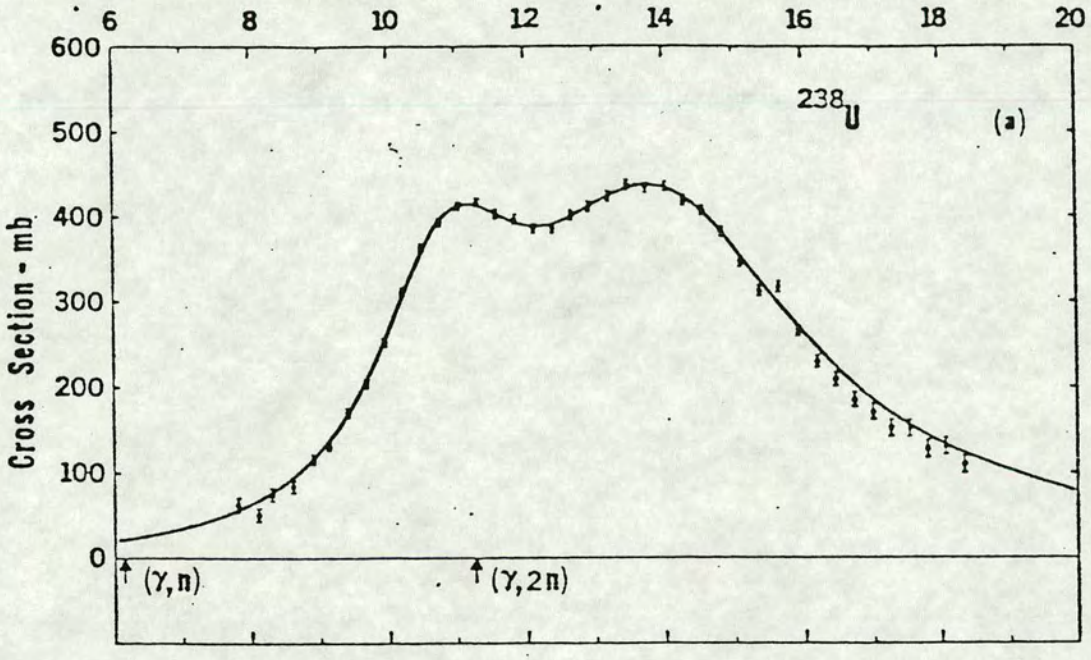

Figure 1.5: Split in the GDR for the deformed nucleus ^{238}U [Berm 75].

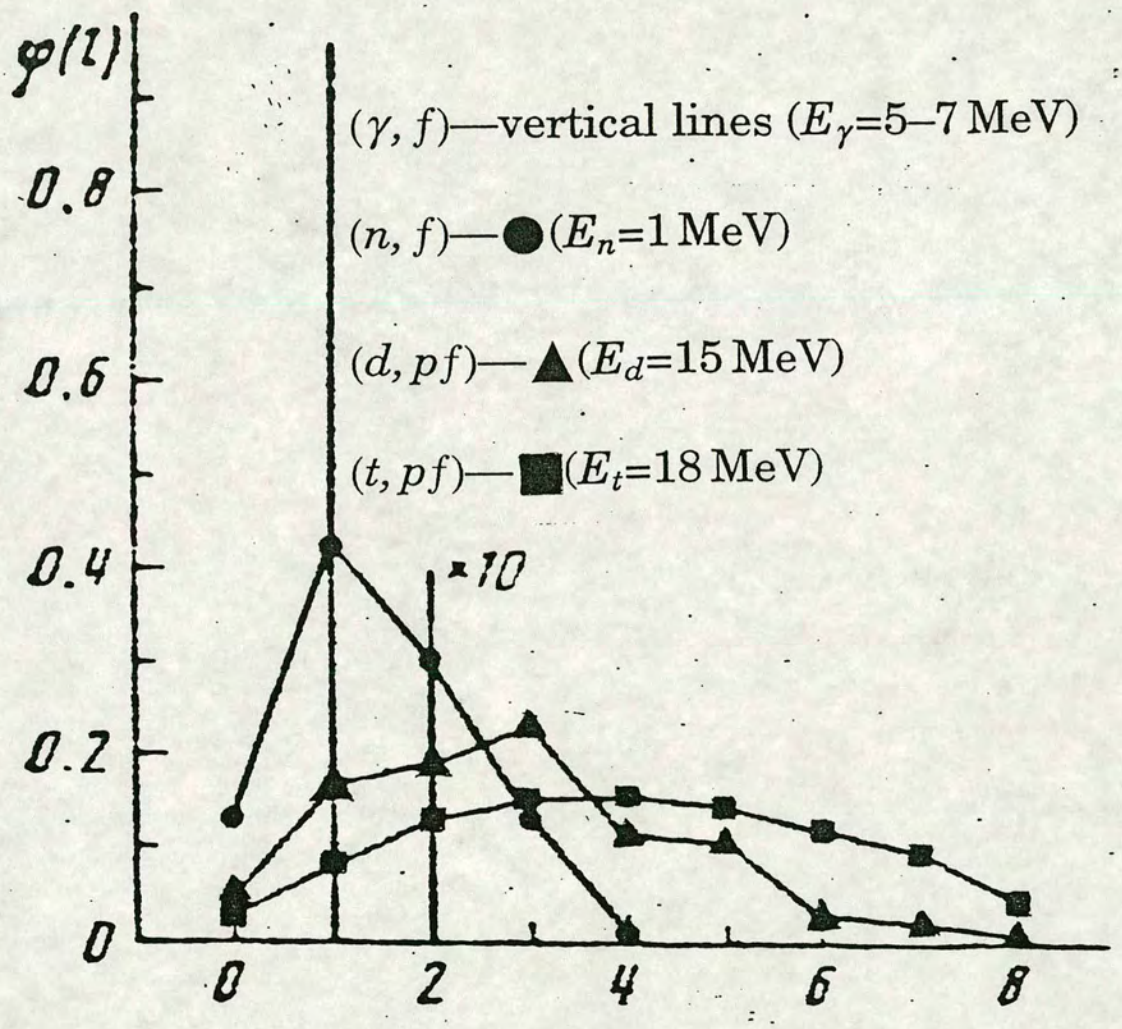

Figure 1.6: The relative intensities of compound nuclear angular momenta excited by various reactions [Zhuc 78].

Chapter 2

Experimental Method

2.1 The Purpose of the Experiment

The purpose of the experiment was to measure simultaneously the photofission cross section, $\sigma_{\gamma,f}$, the photoneutron cross section, $\sigma_{\gamma,n}$, and the mean number of neutrons per fission, $\overline{\nu}$.

2.2 A Résumé of the Experiment

The experiment was performed by accelerating electrons using a linac. The electrons have a known energy determined by bending magnets and are focussed onto a bremsstrahlung target which was in this case gold. The electrons are finally slowed down or stopped producing a continuum of γ-rays. These are then collimated onto the ^{241}Am target. The target is mounted inside an efficient neutron detector which detects the number of neutrons associated with each beam pulse from the linac. Above the (γ, n) threshold, both fission neutrons and photoneutrons will be produced. However, by fitting a theoretical fission neutron multiplicity distribution to events of two or more neutrons --- data was taken below the $(\gamma, 2n)$ threshold --- the number of one neutron fission events can be predicted and subtracted from the total number of one neutron events to separate out the (γ, f) cross section from the (γ, n) cross section. Below the (γ, n) threshold,

the theoretical distribution can be fitted to event multiplicities of one and above.

An ionisation chamber, type P2, was used to measure the γ-ray flux incident on the target allowing absolute cross section measurements to be made.

2.3 The Linac

The experiment was carried out on the Harwell 136 MeV pulsed electron linear accelerator, HELIOS (Fig. 2.1). This is an eight section machine, though for the present experiment only the first two sections were required.

Microwave radiation from the klystrons is fed into circular waveguides loaded with copper irises to give the electromagnetic wave the correct phase velocity to accelerate the electrons. These are injected in pulses into the wave guides and the electron bunches "ride" on the crest of the electromagnetic wave in a "surf-board" fashion (Fig. 2.2). Table 2.1 gives details of the accelerator's operating specifications. Table 2.2 gives the operating parameters used in the present experiment. The electrons are then deflected into the Low Energy (or LE) line (see Fig. 2.3).

2.3.1 The Low Energy Line

The LE line is used to define the energy and energy spread of the electrons and hence of the bremsstrahlung. The first set of bending magnets is used to define the energy of the beam, hence the current in the windings and the magnetic field need to be monitored and controlled quite tightly. The water-cooled slits after the bending magnets determine the spatial spread of the beam and hence the energy resolution. This was set, for the present experiment, at $\pm 1.0\,\%$ and $\pm 0.5\,\%$ depending on the energy steps made. The beam is focussed using pairs of quadrupole magnets onto the bremsstrahlung radiator --- in this case $0.1\,\mathrm{g\,cm^{-2}}$ gold foil. Scintillators can be moved in and out of the beam to indicate the position of the beam spot

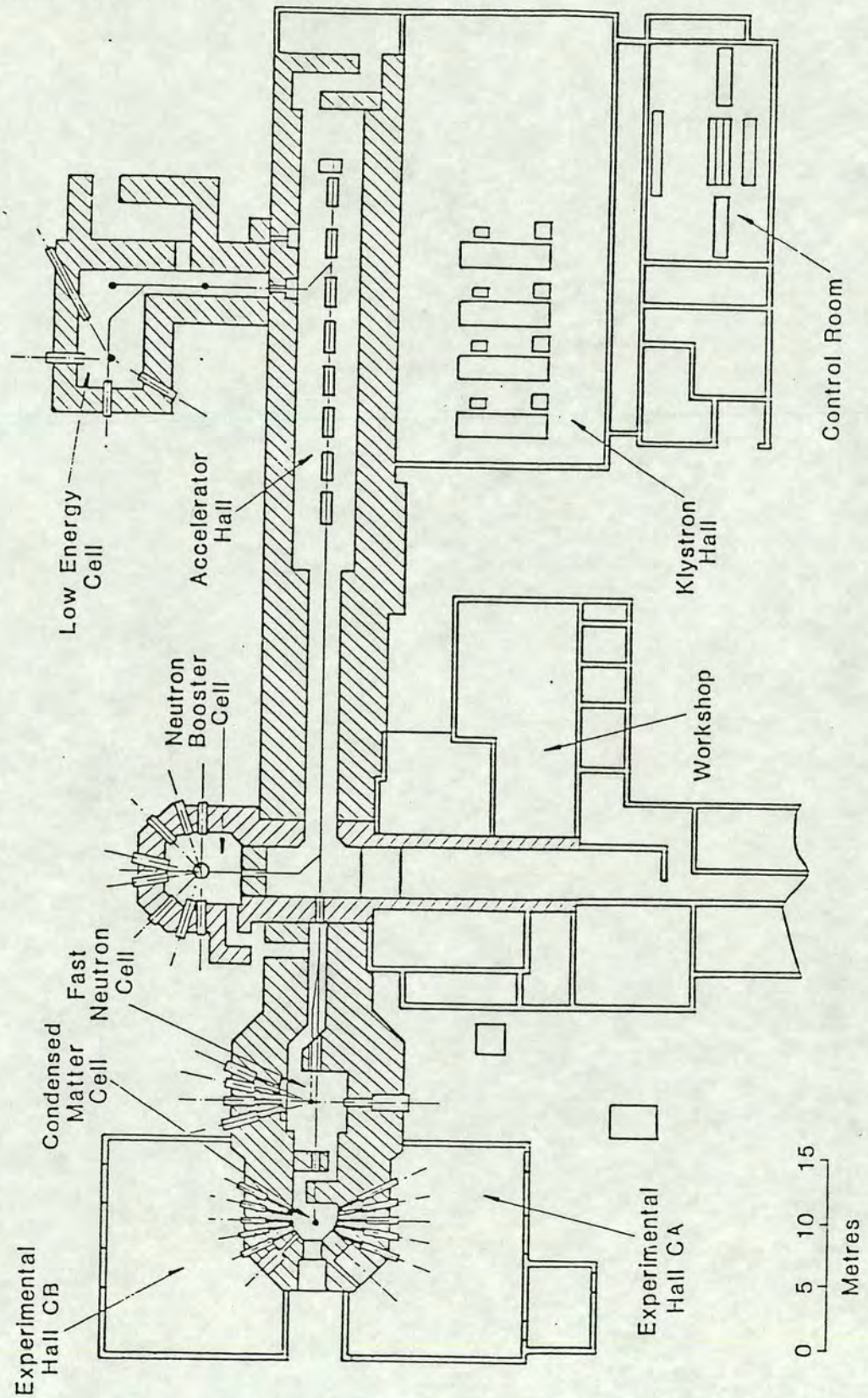

Figure 2.1: HELIOS:The Harwell Electron Linear accelerator for the Investigation Of neutron and radiation Science.

Maximum Energy:	136 MeV.
Operating Frequency:	1300 MHz (L band).
Klystrons:	Four Thompson-CSF type TV 2022 each giving 20 MW or 10 MW peak power and 40 kW mean power.
Acceleration length:	16 m (8×2 m).
Maximum pulse length:	5 μs at ≤300 pps.
Maximum repetition rate:	2000 pps for pulse width ≤0.4 μs.
Electron pulse duration:	Variable from 5 ns to 5 μs.
Maximum beam power:	30 kW (short pulses), 90 kW (long pulses).
Maximum pulse current:	6--11 A (short pulses), 0.6--1 A (long pulses).

Table 2.1: The accelerator specifications.

Electron energy:	Between 5.6 and 10 MeV.
Pulse repetition rate:	500 pps.
Width of energy-defining slits:	±1% or ±0.5%.
Max. pulse current at bremsstrahlung radiator:	400 mA.
Pulse width at bremsstrahlung radiator:	Between 0.1 and 1 μs.
Gamma dose on target per electron pulse:	~0.04 mRad.

Table 2.2: Operating conditions for the present experiment.

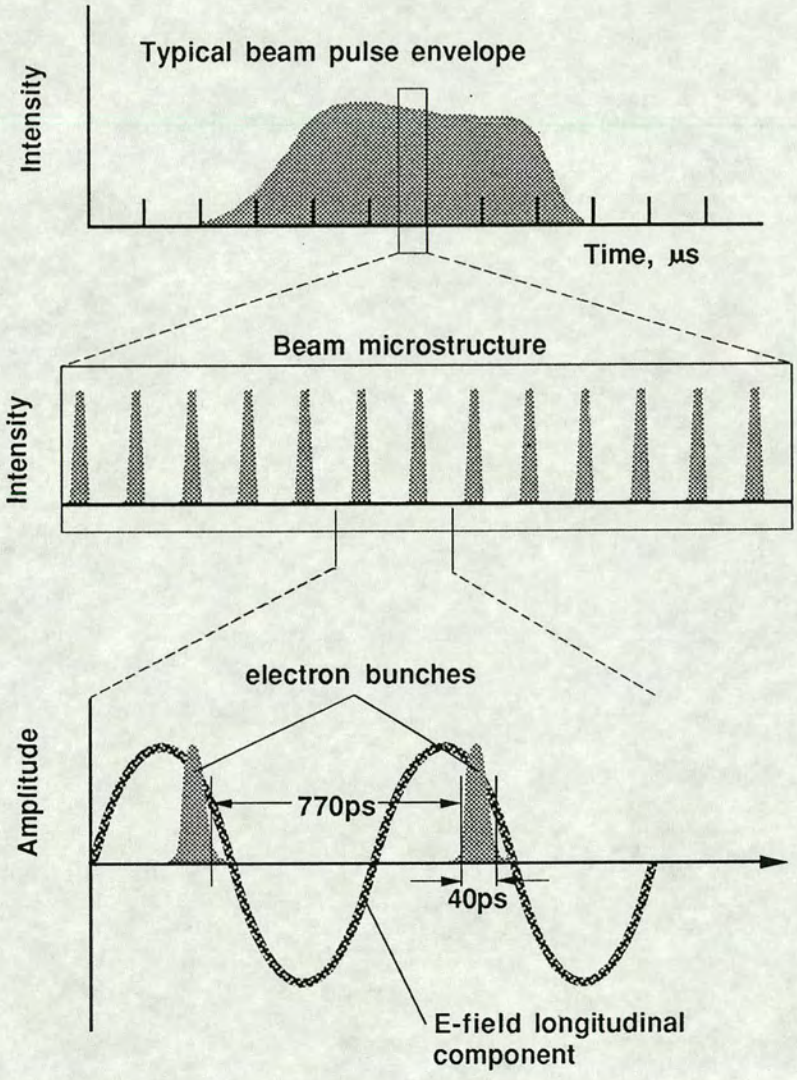

Figure 2.2: Electrons being accelerated by a travelling wave.

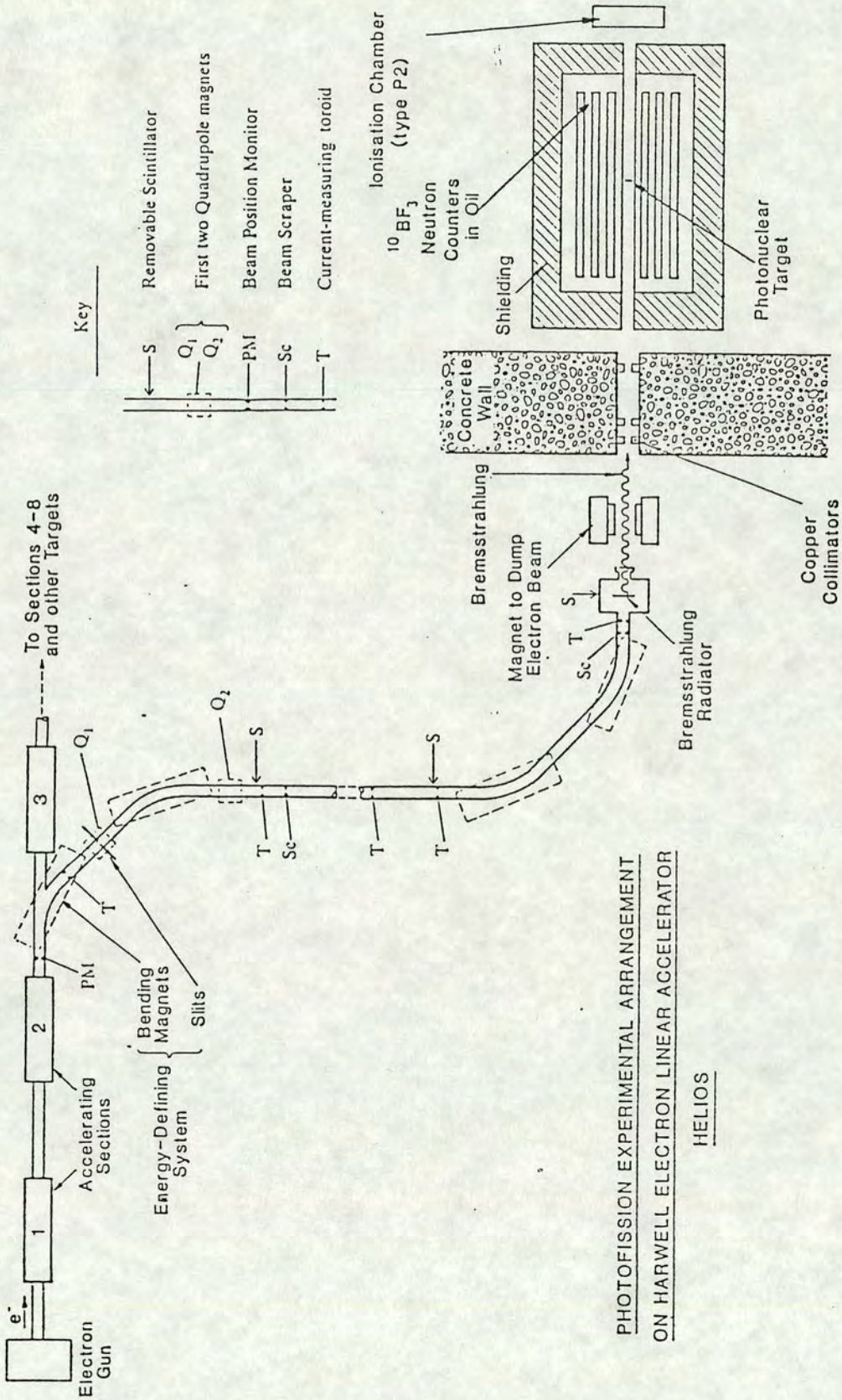

Figure 2.3: The Low Energy line.

for steering purposes. Also, the beam current is monitored by toroidal beam transformers to give an indication of the pulse width and current incident on the radiator.

2.4 The Target

2.4.1 General Description

For this experiment, one target of 1.533 g of ^{241}Am metal was used, prepared by and on loan from the Oak Ridge National Laboratory, U.S.A., . The metal was rolled into a sheet and cut into a 2 cm x 2 cm square with an areal density of 0.383 g cm^{-2}. The metal was obtained from its oxide by a reduction-distillation process carried out by the Isotope Research Materials Laboratory, U.S.A. [Vanp 84]. Table 2.3 shows the isotopic analysis of the oxide and Table 2.4 shows the isotopic analysis of the metal after reduction-distillation. In subsection 2.4.3 it is shown, with reasonable confidence, that there is a certain percentage of fluorine in the target even after reduction-distillation, with undesirable side-effects discussed therein.

2.4.2 The Target Mounting

^{241}Am is predominantly an α-particle emitter and thus 1.533 g of ^{241}Am presents something of a radiological hazard.[1] For this reason, as well as to prevent oxidation, the target was mounted, between two thin (0.01 mm) nickel foils which are virtually transparent to 5--10 MeV γ-rays, but absorb α-particles, inside an evacuated metal can (see Plate 1). The main structure of the can is made from aluminium with a thin aluminium window at either end of the can to allow the γ-ray flux to pass through the target unhindered. The outside of the can is surrounded by a 2 mm thick sheet of lead to shield the detector from the γ-rays accompanying α-decay of the target. A

[1] The target has an activity of ~5 Ci.

Element	*Quantity (wt. ppm)*	*Element*	*Quantity (wt. ppm)*
Al	0.3	V	1.0
B	1.0	Zn	0.5
Ba	0.3	Zr	5.0
Ca	2.0	Cl	3.0
Cr	0.2	F	0.7
Cu	0.2	S	7.0
Fe	3.0	Y	5.0
K	0.3	La	10.0
Mg	1.0	Ce	250.0
Na	1.0	Pr	3.0
Ni	0.5	Nd	10.0
P	0.1	Eu	10.0
Pb	7.0	Tb	0.5
Sb	<0.5	Dy	5.0
Si	3.0	Ho	0.5
Sn	<0.7	Er	≤2.0
Ta	≤1.0	Tm	70.0
Te	2.0	Yb	5.0
Ti	<0.1	Lu	0.5

Table 2.3: Spark source mass spectrographic analysis of high purity americium oxide used for americium metal preparation.

Element	*Quantity (wt. ppm)*
Al	10
B	10
Ca	200
Cr	10
Fe	≤50
K	10
Mg	≤10
Na	30
Ni	≤10
P	≤2
Si	≤100
Zn	≤50
^{239}Pu	≤30
S	50

Table 2.4: Spark source spectrographic analysis of americium metal prepared by reduction-distillation process.

dummy can was constructed, identical in every way to the target can, (but containing no ^{241}Am target) for mounting dummy targets or sources in the detector.

2.4.3 Analysis of the Target

For ^{241}Am, α-decay accounts for ~ 100 % of the decay strength and spontaneous fission for only 3.77×10^{-10} %. Assuming a pure metal target and ~ 3 neutrons per fission, this implies a neutron output for the target of ~ 2 neutrons per second. When the target can was placed in the detector, an emission rate of ~ 7500 s^{-1} was found. Clearly, some reaction other than spontaneous fission was going on in the target.

(α, n) Neutrons

If the target is not a pure metal, there is the opportunity for (α, n) reactions to take place. Neutron yields for light elements under α-bombardment are listed by *e.g.* Liskien and Paulsen [Lisk 77]. A first thought might be, therefore, that the target can had leaked allowing the target to oxidise, resulting in the reaction ^{16}O(α, n). However, allowing for even total oxidation of the target, this should only give a neutron output of ~ 80 s^{-1} using figures for the ^{16}O(α, n) thick target yield quoted by Bair and Gomez del Campo [Bair 79].

(α, n) sources have characteristic γ-rays accompanying the reaction as the excited residual nucleus decays to its ground state. Therefore, it was decided to examine the spectrum of γ-rays from the target to try and find out what impurity might be causing the high neutron flux. For this purpose, an intrinsic Ge detector was placed near to the source, keeping the dead-time down to an acceptable rate from the high flux of γ-rays. The output was fed into an amplifier and used to produce a pulse height spectrum with a multi-channel analyser (M.C.A.). The energy scale of the spectrum was calibrated using a ^{22}Na source plus two naturally occurring lines from ^{40}K and ThC″ (^{208}Tl).

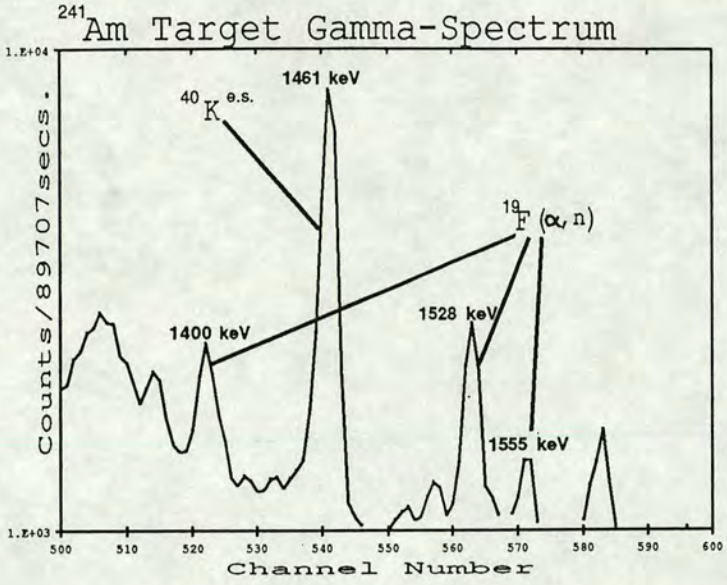

Figure 2.4: γ-spectrum of ^{241}Am Target.

Upon analysis, no lines consistent with the constituents of Table 2.4 were observed with sufficient intensity to give rise to the large neutron output. Reference was then made to work done by Lees and Lindley [Lees 78] concerning the neutron output from an $^{241}AmO_2$ source. In this case, neutron output was determined for all possible sources in the $^{241}AmO_2$, taking account of all known impurities *i.e.* those impurities that had been declared by the suppliers T.R.C. Amersham. Nevertheless, this still led to a shortfall in the neutron output. A γ-ray spectrum was taken and upon analysis, lines due to $^{19}F(\alpha, n)$ and $^{19}F(\alpha, p)$ were found. The authors were clearly surprised to find this undeclared fluorine impurity and indeed, upon close inspection, several of these $^{19}F(\alpha, \frac{n}{p})$ lines were found in the spectrum from the ^{241}Am target used in this experiment (see Fig. 2.4). Henceforth, a similar spectrum was made for the present experiment from an ^{241}Am/F source (of known neutron output) was taken to normalise the ^{241}Am target spectrum. By adding up the number of counts in the four most prominent $^{19}F(\alpha, n)$ lines in the two spectra and normalising for time and solid angle, the number of neutrons due to $^{19}F(\alpha, n)$ reaction was of the correct order to that observed, within about 30% accuracy. Obviously, the lead shielding of the target used in the present photonuclear experiment and the ^{241}Am/F

capsule were different, however, the evidence does point to the large flux of neutrons being due to an undeclared impurity of fluorine which is, in fact, used in the extraction of certain actinides.

Further evidence for this assumption comes from the *ring-ratio* of the neutron detector (described in section 2.5). The ratio implied a mean neutron energy of ~ 1.6 MeV, which corresponds to the neutron energy quoted for an ^{241}Am/F source by Owen *et al.* [Owen 82].

Why this fluorine impurity was not detected in the spectrographic analysis is unknown. Lees and Lindley, who saw approximately the same flux of neutrons due to fluorine in their target, suggested that the fluorine was probably present in parts per thousand which ought to be detectable by spectrographic methods.

Fission Neutrons

In an (α, n) source, the time correlation between neutrons is random *i.e.* the distribution of times between neutrons follows a Poisson distribution. However, in a spontaneous fission source, neutrons will be emitted in bursts following each fission. Hence, by setting up a T.A.C. (time-to-analogue converter) as in Fig. 2.5, a histogram was built up on an M.C.A. of the time between successive neutrons emitted by the ^{241}Am target. Due to the low count rate, spectra need to be taken over about a week. The detector package used had a well-defined die-away time of $23 \pm 1\,\mu$s and consisted of a ^{3}He counter in a block of moderating polythene surrounded by cadmium to absorb neutrons which have thermalised after "bouncing" around the room and will be totally uncorrelated and so therefore undesirable.

Fig. 2.6 shows the T.A.C. spectrum for an ^{241}Am/B source with a full scale of 1 ms (1 μs/channel). The mean detected singles count rate was ~ 100 counts/second which is consistent with the time constant of 10 ms (time constant $\propto$ 1/(mean count rate)). There is no structure at small times to suggest fission neutrons, as one might expect from the very small amount of ^{241}Am in the ^{241}Am/B source (~ 100 mCi).

Fig. 2.7 shows the T.A.C. spectrum from the ^{241}Am target. Again the mean detected singles count rate was ~100 counts/second which is consistent with the ~10 ms time constant observed in the T.A.C. spectrum. Clearly, there is some structure at the beginning with a time constant of ~60 μs. With such a time constant of about three times that of the detector package die-away time of ~23 μs at first sight this seems unlikely to be due to prompt neutrons from fast neutron induced fission where one fission neutron provides a start and another a stop resulting from fission induced by neutrons from the (α,n) reaction on the fluorine contaminant in the target, in which case one would expect a time constant of the order of the detector package. However, the ratio of the small time constant area (60 μs) to that of the large time constant area (10 ms) is about 1/240. The proportion of (α, n) neutrons which could induce a fission reaction is given approximately by the expression $\rho_{dens} N_A \sigma_{n,f} t_{eff}/A$ where ρ_{dens} is the density of the ^{241}Am target, N_A is Avogadro's number, $\sigma_{n,f}$ is the total neutron induced fission cross section and A is the atomic number of ^{241}Am.The quantity t_{eff} is the effective target thickness which takes account of the fact that not all of the (α, n) neutrons will penetrate the entire thickness of the target and is a certain fraction of the actual target thickness t_{targ} such that $t_{eff} \approx 0.5 t_{targ}$. If the neutron induced fission cross section is assumed to be around 2 b for 1.6 MeV neutrons [ENDF **] (resulting from (α, n) on fluorine) then the fraction of (α, n) neutrons inducing fission reactions is about 1/1000. If each fission gives rise to around 3 neutrons then this calculation implies a ratio of about 1:300 fission neutrons to (α, n) neutrons. This number is not too dissimilar to the fraction of 1/240 deduced from Fig. 2.7.

In conclusion, therefore, although there is a 60 μs component in the T.A.C. spectrum of uncertain origin, no firm evidence is seen for a large number of prompt fission neutrons from the ^{241}Am target. Is seems that the most likely cause of the 60 μs component is from (α, n) neutron induced fission neutrons. The time constant is much larger than expected, though this might be due to uncertainties in the experimental set-up and the

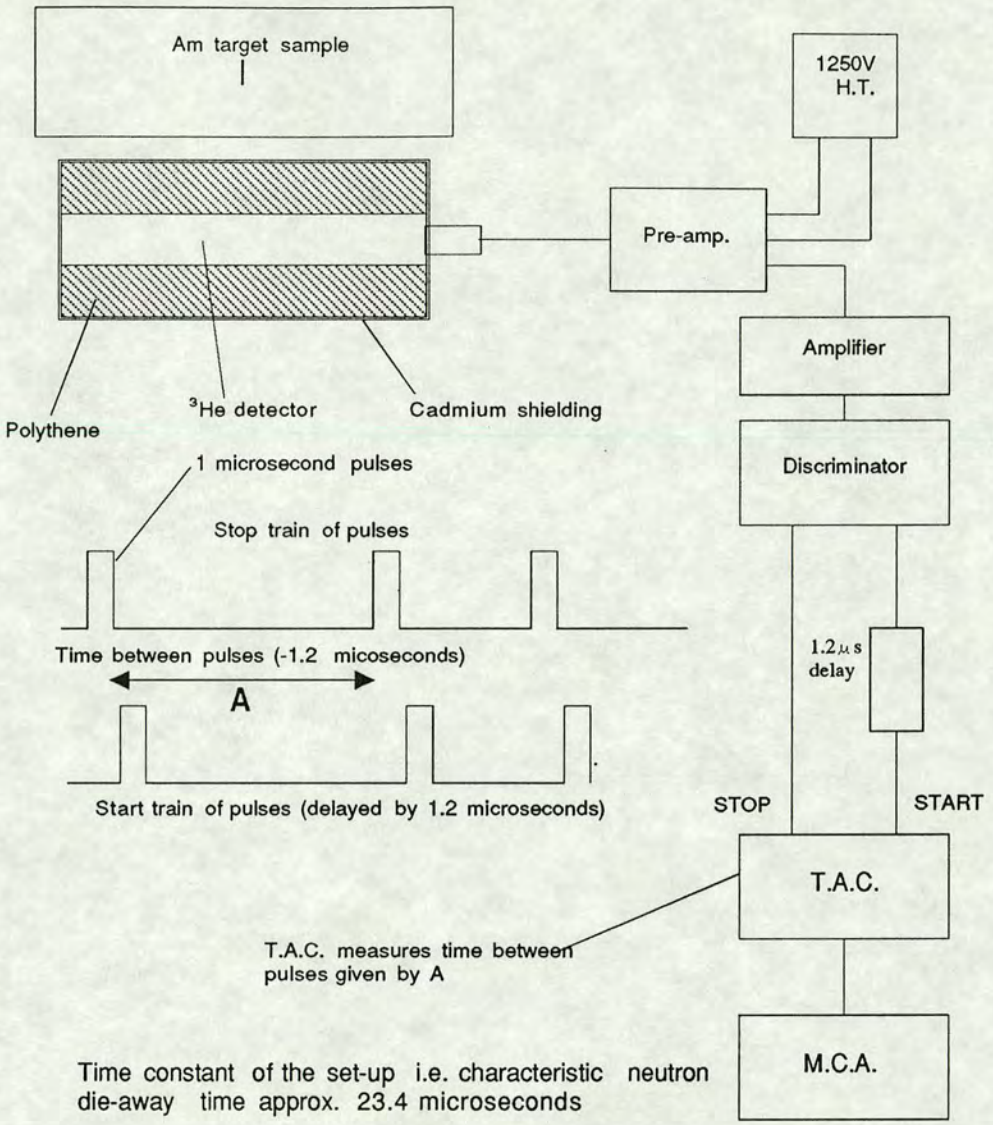

Figure 2.5: The set-up to produce a T.A.C. spectrum.

accuracy of the experiment. Indeed the fact that the detector package was situated on a concrete floor might mean that the die-away time was longer than originally measured due to neutrons being scattered back into the detector by the nearby concrete.

Auto-radiograph of the Target

It was decided, as a check, to see if the target was mounted in the position that it was supposed to be in its can. This was done by "taking a picture" of the target using its own radiation and a lead "pin-hole" camera set-up as in Fig. 2.8.

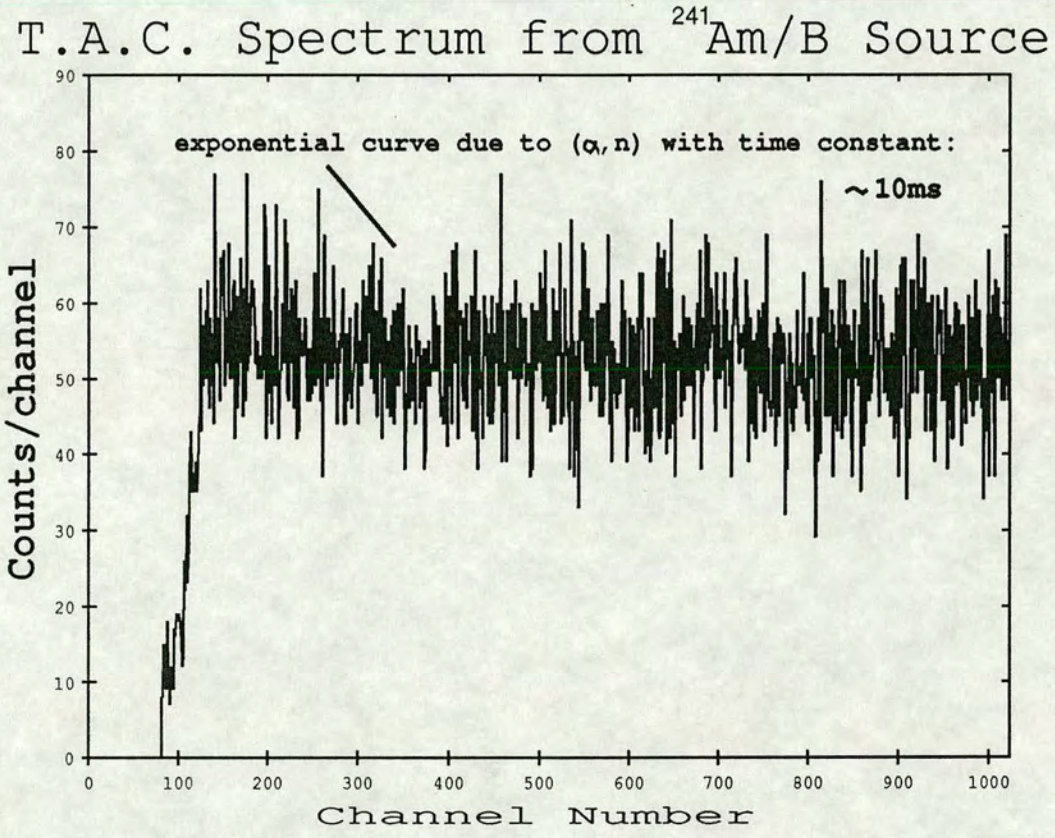

Figure 2.6: T.A.C. spectrum from ^{241}Am/B source.

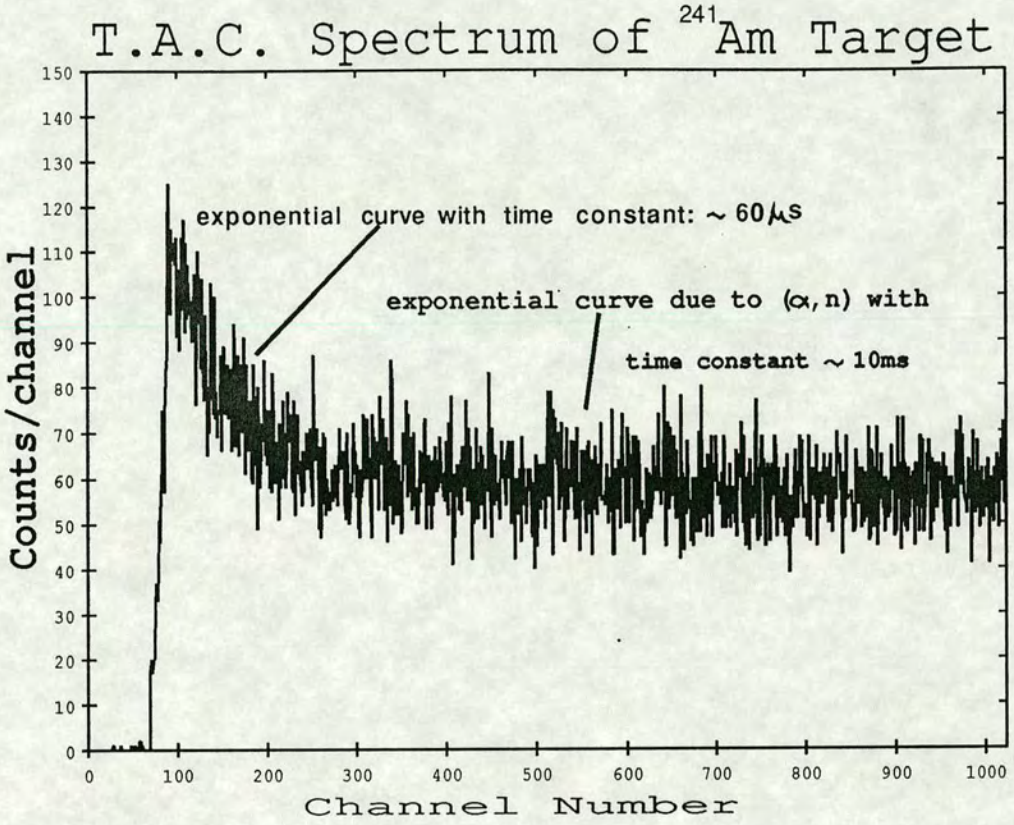

Figure 2.7: T.A.C. spectrum from ^{241}Am target.

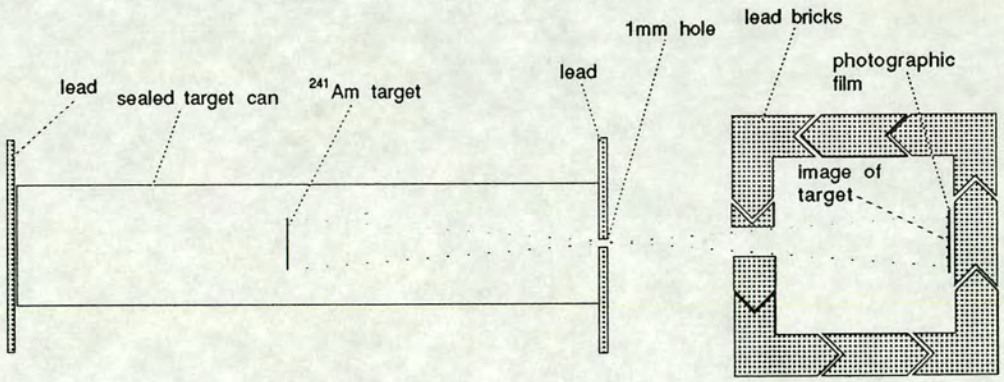

Figure 2.8: The "lead pin-hole camera."

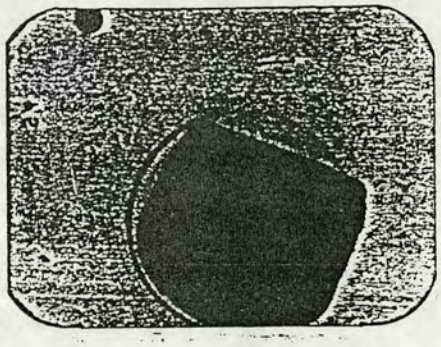

Figure 2.9: The film after exposure to the ^{241}Am target.

The arrangement was set up to allow the target to form an image of itself on a film badge to give ~ 1:1 ratio of target: image. The pin-hole was a 1 mm hole in a piece of lead placed in front of the target can thin aluminium window. The lead was thick enough to attenuate the γ- radiation sufficiently not to fog the film, except that which passed through the pin-hole. Lead was also placed at the other end of the can to prevent unnecessary radiation leaking out of the thin aluminium window at that end. The film was shielded all around, except for an aperture, to allow exposure to the target image, but not to unwanted radiation which may bounce around the room. This particular set-up required around 5 days to give sufficient exposure of the target (~ 10 mSv dose equivalent).

Fig. 2.9 shows the film after exposure. The faint circle is drawn to indicate the position of the pin-hole. In fact, taking into account where the film was mounted and where the target image appeared, the target seemed to be in the correct position, to within the accuracy of this set-up ($\pm$1 mm). This was quite adequate for the constraints placed upon the beam which would be incident on the ^{241}Am target during the experiment.

2.5 The Detector

The detector used in this experiment was designed to be both efficient and have an efficiency virtually independent of neutron energy. In fact, the

efficiency can be approximated by a linear function of energy, decreasing slightly as neutron energy increases. The design was based on the Halpern type as described by Gerstenburg and Fuller [Gers 67] The detector itself is described in full by Lees *et al.* [Lees 80] with modifications as described by Edwards *et al.* [Edwa 82].

The detector employs copper-walled $^{10}BF_3$ (boron trifluoride) gas proportional counters of *active* length 1070 mm, and 50 mm cross sectional diameter. $^{10}BF_3$ counters are preferred to the more efficient ^3He neutron counters, because the former are less sensitive to the γ-flash produced by the intense spray of bremsstrahlung used in this experiment. The counters used rely on the reactions:

$$^{10}_{5}B + {}^{1}_{0}n \xrightarrow{93\%} {}^{7}_{3}Li^{(1^{st}\,e.s.)} + \alpha + 2.30\ \text{MeV} \quad (7)$$

$$\xrightarrow{7\%} {}^{7}_{3}Li^{(g.s.)} + \alpha + 2.78\ \text{MeV} \quad (8)$$

The reaction is detected by the ionisation caused by the Li and α particles. The cross section for the reactions is very high at low neutron energies (~3800 barns at thermal energies) but falls off rapidly with neutron energy. Hence, the neutrons need to be moderated for efficient detection. For this reason 56 $^{10}BF_3$ counters are arranged in five concentric rings immersed in a tank of transformer oil.

The tank is 0.8 m wide x 1.3 m long x 1.0 m high. The oil has a large density of hydrogen atoms which are most efficient at moderating neutrons. This slowing down produces a random delay between neutrons produced in one event, allowing each neutron to be detected separately - essential for determining neutron *multiplicity*. Plate 2 shows the detector with its lid removed to reveal the counters partly submerged in the oil. Plate 3 shows the rings of counters hoisted out of the detector tank. Fig. 2.10 shows a schematic diagram of the detector viewed end-on. The rings consist of 8, 8, 8, 16 and 16 counters going outwards from the centre consecutively. The ratio of neutrons detected in the outermost-ring to the innermost-ring (the so-called *ring-ratio*) gives a measure of the mean neutron energy (higher energy neutrons will tend to diffuse further out from the centre before

detection than lower energy neutrons thus increasing the ratio). The ^{241}Am target, in its evacuated can, is placed in the central through-tube.

The detector is surrounded by cadmium to "mop up" any stray thermal neutrons and borated resin to absorb neutrons which might otherwise "rattle around" the block house and back into the detector creating an unwanted background. In addition, the detector is surrounded by lead bricks to shield from the γ-flash.

The blockhouse in which the detector is sited is air conditioned and kept at a constant temperature as $^{10}BF_3$ counters are susceptible to changes in both temperature and humidity. For this reason also, the oil is periodically streamlined (heated up under vacuum allowing any water in it to evaporate off) to keep the counters as free from moisture as possible.

2.5.1 The Detector Electronics

Fig. 2.11 shows a schematic diagram of the electronics used for the data collection in this experiment. Each counter runs at an E.H.T. of 3.8 kV and as such needs to be capacitatively decoupled from the pulse shaping preamplifiers. In addition, there is filtering of the bias supply to remove spurious mains signals. The components used for decoupling and filtering are located in an earth screened box which is hermetically sealed with replaceable desiccaters located inside the box ensuring that no moisture can induce breakdown or noise. The pulses from the preamplifier are fed into an amplifier and on into a discriminator. Fig. 2.12 shows a typical pulse height spectrum for a ring with the discriminator level indicated.

Neutrons from an event associated with each beam burst are recorded for the duration of two gates as in Fig. 2.13. The set-up is gated to maximise the signal-to-noise ratio with a *spectrum* gate of 200 μs duration 7 μs after the γ-flash to record (γ, f) and (γ, n) neutrons. A similar *background* gate follows 1 ms later to record background neutrons and each cycle is repeated every 2 ms. The pulses from each ring are digitised and recorded during each gate as a serial digital signal, 3 bits for each ring and an extra bit to

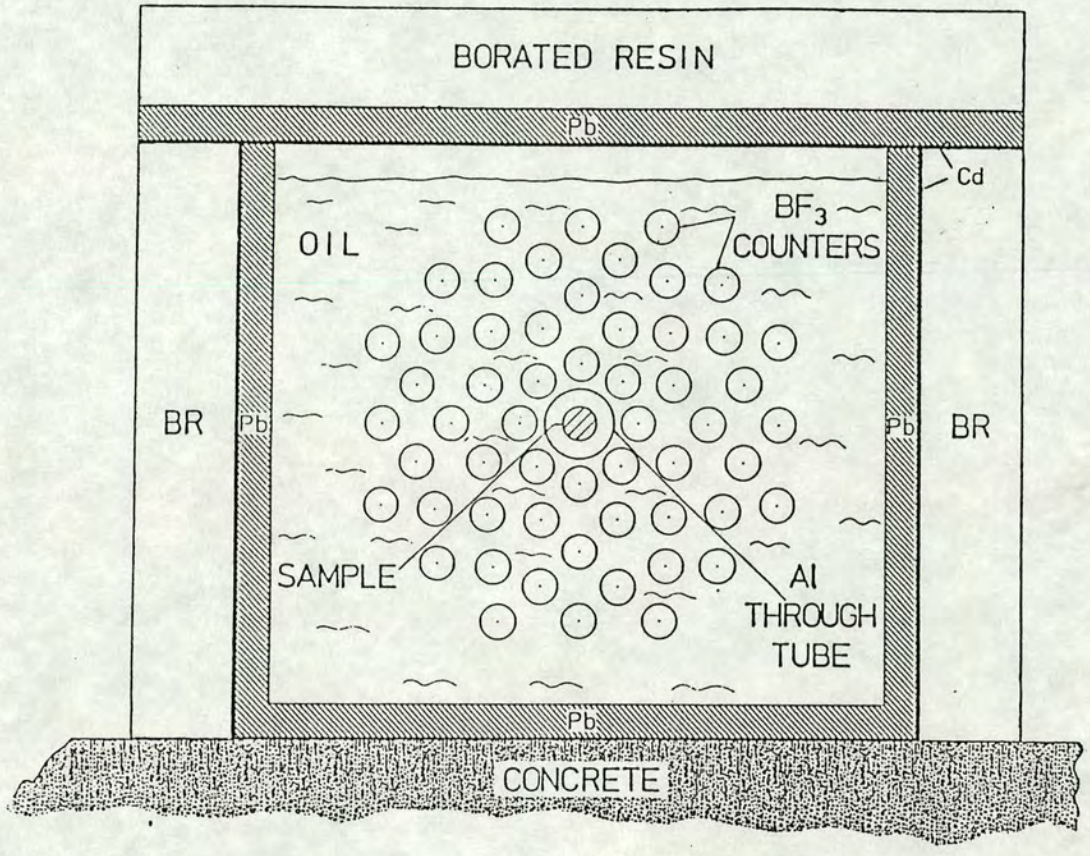

Figure 2.10: Schematic of the neutron detector.

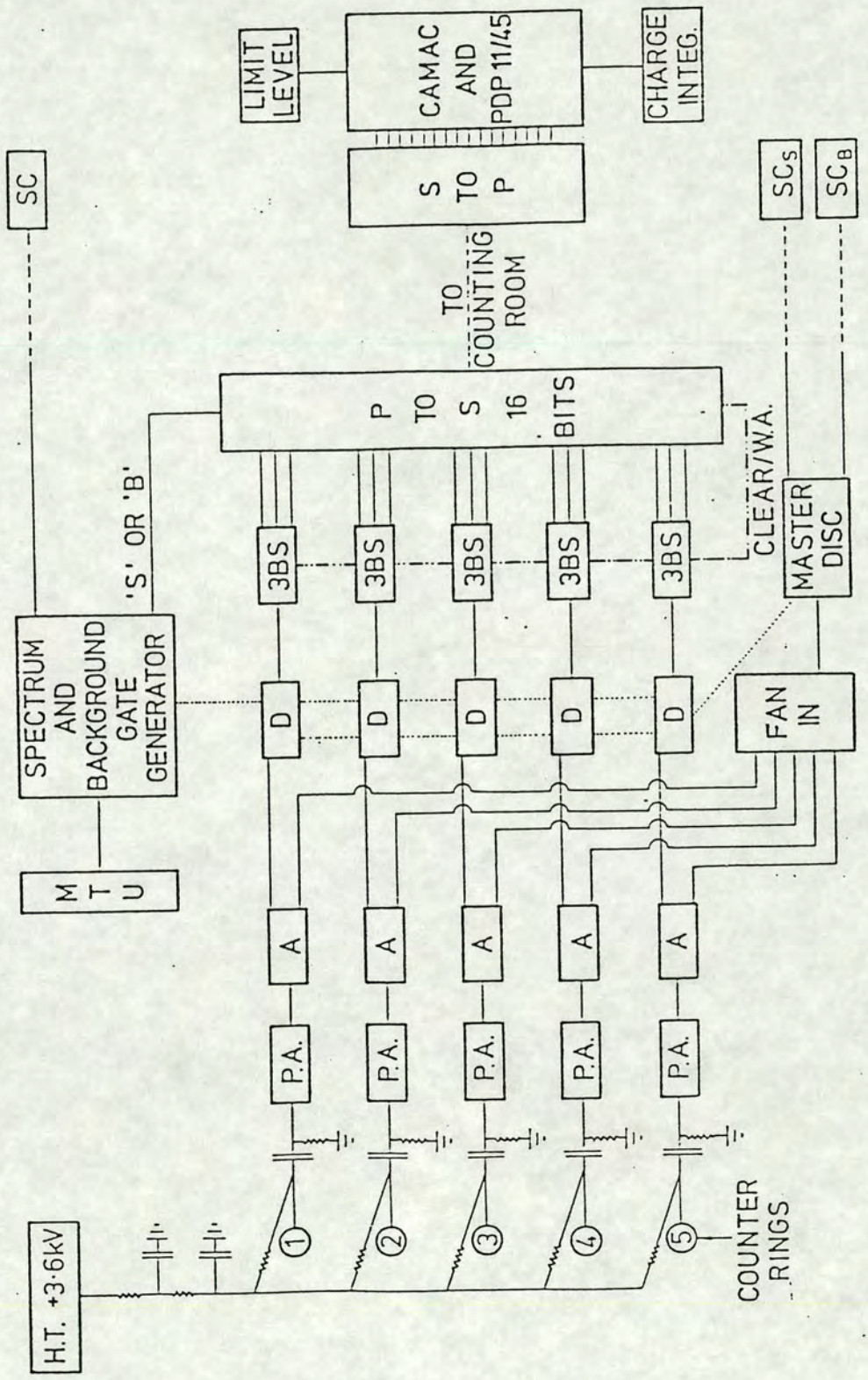

Figure 2.11: The detector electronics.

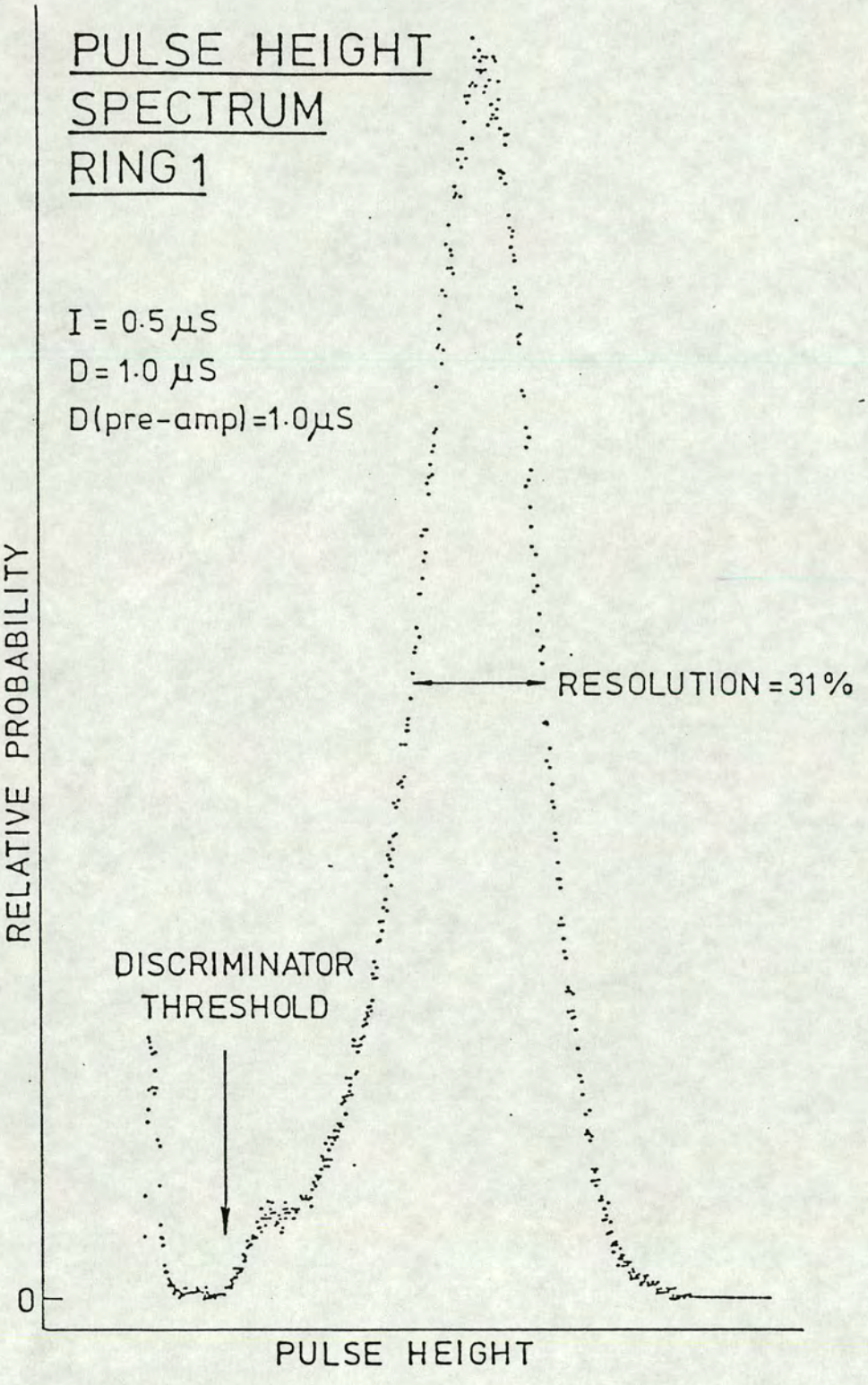

Figure 2.12: A typical pulse height spectrum for a ring of $^{10}BF_3$ counters.

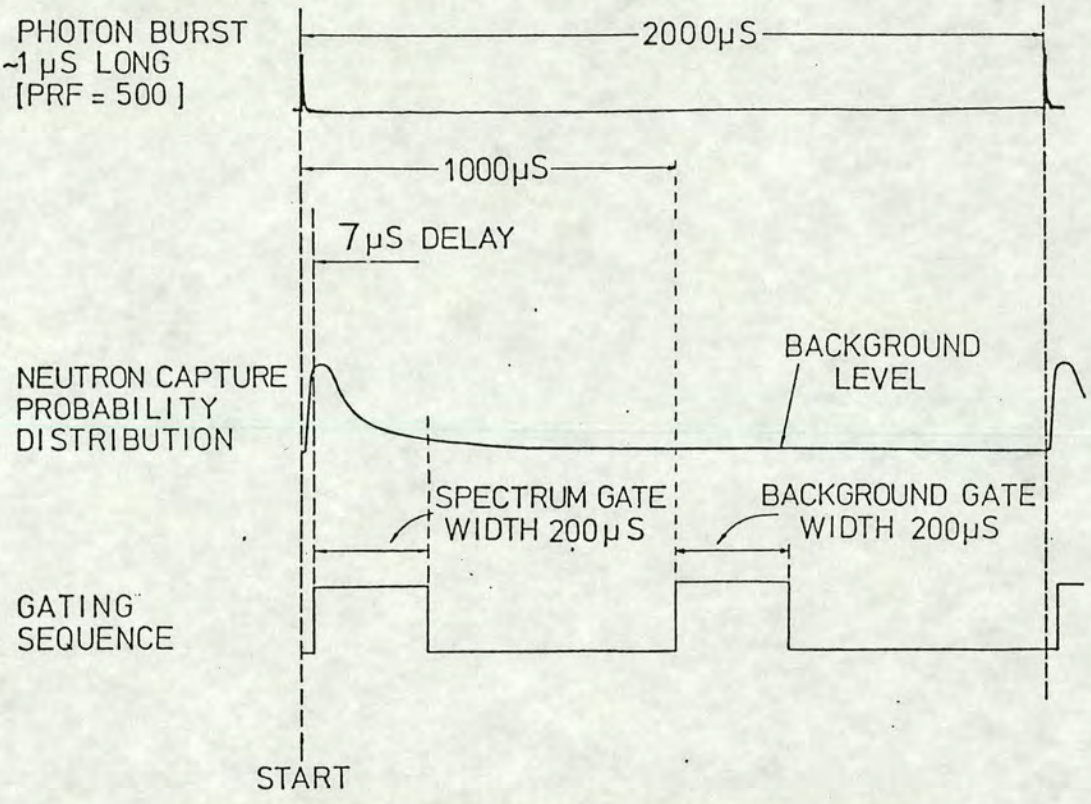

Figure 2.13: The gates used to detect neutron pulses.

indicate either spectrum or background is tacked onto the pulse train. The signal is sent to the counting lab via a CAMAC interface to a PDP 11/45 computer where the signal is decoded and the spectrum and background multiplicity for each beam pulse used to increment multiplicity histograms. As a cross check, analogue signals from the amplifiers are recorded by Harwell 2000 series scalers to give the total number of spectrum and background neutrons.

2.5.2 The Detector Response

Efficiency

As mentioned in a previous section, the detector was designed to have an efficiency virtually independent of neutron energy. The efficiency was determined by placing various calibrated neutron sources in the centre of the detector and counting the number of neutrons detected for a fixed length of time.

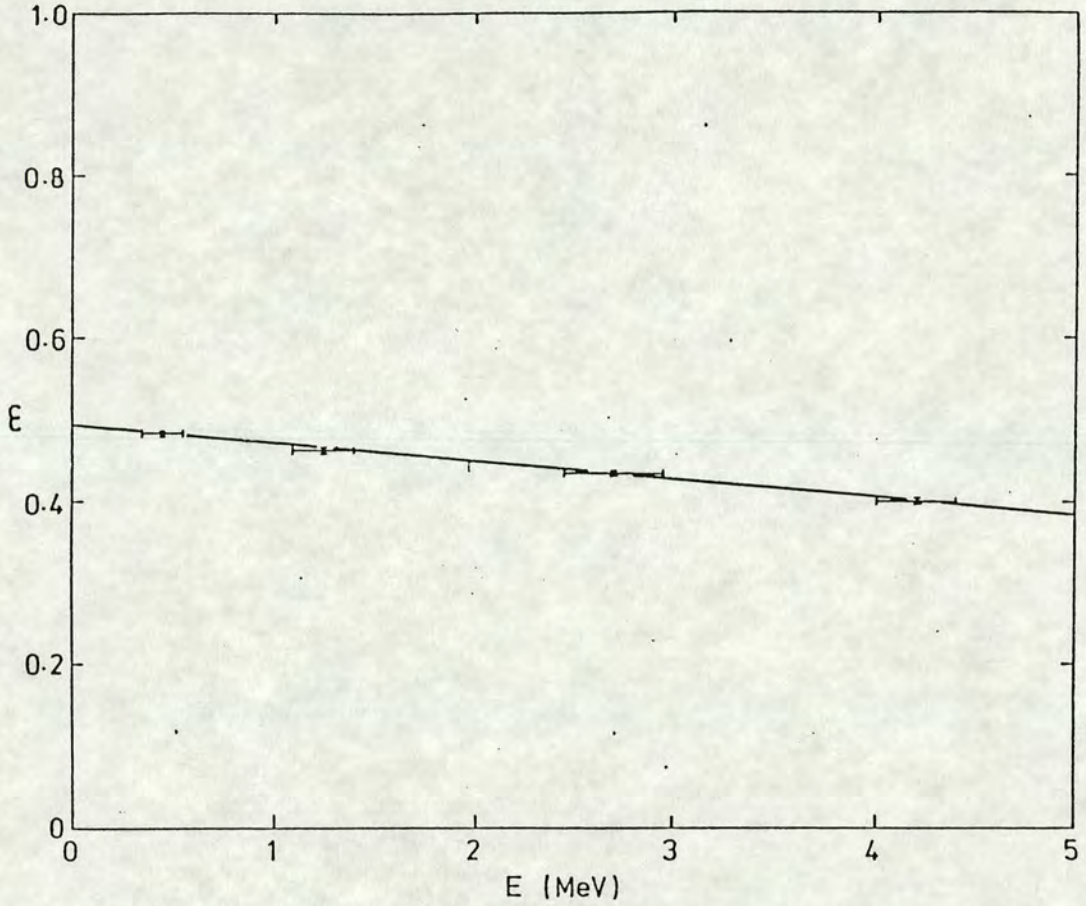

Figure 2.14: The efficiency of the detector.

The sources used were: ^{241}Am/B, /Be, /Li, /F (α, n) sources and ^{252}Cf(s.f.)[2]. All of these sources were calibrated using a manganese bath at the National Physical Laboratory at Teddington, Middlesex. After count loss corrections, (described in the Analysis Chapter) the efficiency for each source can be obtained. Though each source emits a spectrum of neutron energies, a mean energy can be assumed for each source to give a plot of detector efficiency against mean neutron energy such as in Fig. 2.14. A linear best line fit can be made to the data showing a slight decrease in efficiency with energy. This one might expect as higher energy neutrons will tend to diffuse further out from the centre of the detector before moderation and hence have a greater chance of escaping the detector before detection.

Knowledge of the energy dependence of the detector efficiency is impor-

[2]s.f. ≡ spontaneous fission

tant in calculating the number of (γ, f) and (γ, n) neutrons associated with multiplicity one events, the former type having a higher average energy than the latter (see Analysis Chapter).

Neutron Capture Time Distribution

In order to set the optimum gate widths and timing to maximise the signal-to-noise response, knowledge of the neutron capture time distribution is required. For this purpose a ^{252}Cf spontaneous fission sample is used.

The sample is incorporated into an ionisation chamber and the ionisation caused by the fission fragments gives rise to a pulse which can be used as a timing "start" to time how long after fission the fission neutrons are detected. Fig. 2.15 shows this distribution in time. The mean neutron lifetime of neutrons in the detector is $135\,\mu$s. The gate width for backgrounds and spectrums was set at $200\,\mu$s, and the distribution enables one to make a capture time correction to the overall efficiency of detection. For example, in the case of a $200\,\mu$s spectrum gate opening $7\,\mu$s after the γ-flash, statistically, $0.796 \times \varepsilon_{\gamma f}$ of the total number of fission neutrons will be detected in that gate.[3] The figure of 0.796 is called the *gating factor* and is given by

$$g = \int_{t_{open}}^{t_{close}} P(t)\,dt \tag{9}$$

were $P(t)$ is the capture time distribution, and t_{open} and t_{close} are the opening and closing times of the gate, respectively.

2.6 The P2 Chamber

As mentioned previously, the γ-ray flux needs to be measured to make absolute cross section measurements.

The device used in this experiment to do so is a type P2 ionisation chamber, the response of which is described in detail by Pruitt and Domen

[3] $\varepsilon_{\gamma f} \equiv$ ungated efficiency of detection for (γ, f) neutrons.

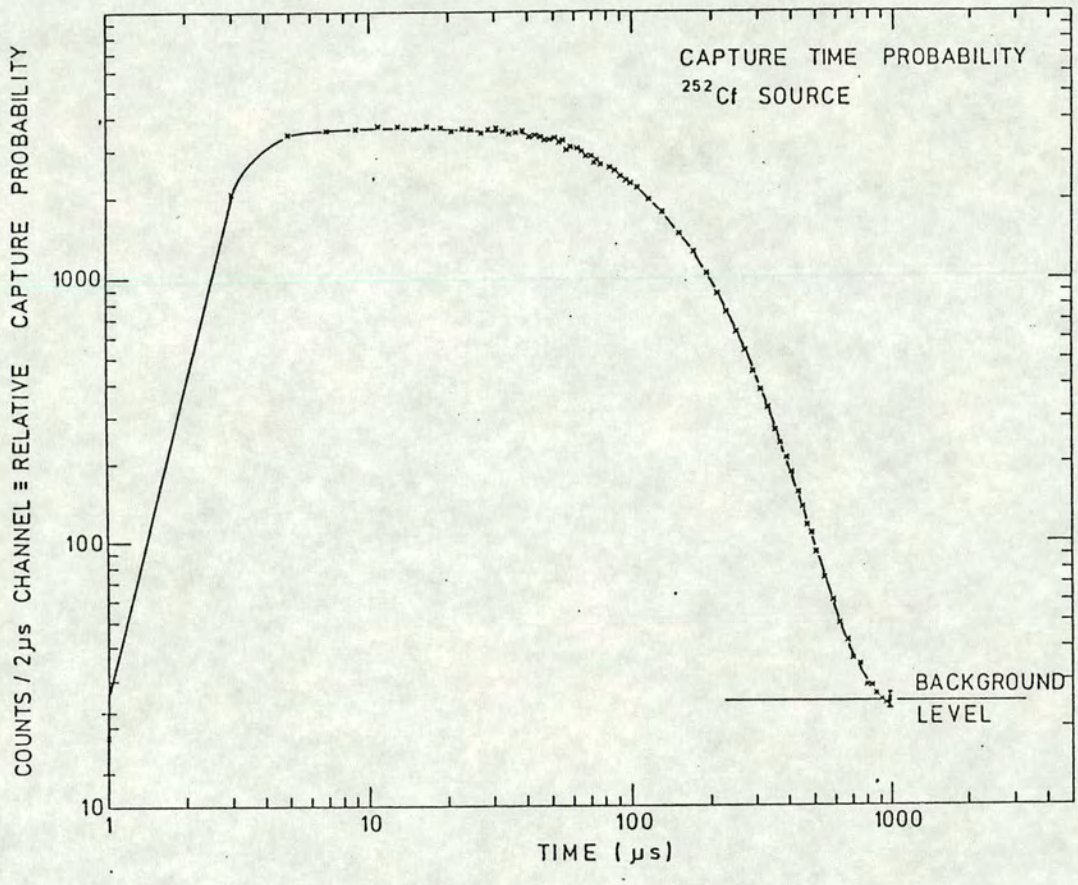

Figure 2.15: The capture time distribution.

[Prui 62]. Its response is affected by changes in pressure and temperature. As said before, the temperature in the blockhouse is kept constant to within $\pm 1^0$C. The pressure is recorded by a barograph connected to a chart recorder for the duration of the experiment and used to correct the measured flux at a later stage (see Analysis Chapter). The incident radiation energy is a function of the collected charge and the maximum photon energy, as also described in the Analysis Chapter.

In order to measure the flux incident on the target, the P2 chamber is mounted in line with the through-tube (as shown on Fig. 2.10) and downstream of the target. Most of the flux passes straight through the target without interaction and with a small correction for photon attenuation in the target, the flux can be measured fairly accurately although problems did arise which will be mentioned later. Plate 4 shows the detector with the P2 chamber in position.

The charge from the chamber is measured by a Brookhaven current integrator which gives out a pulse for a fixed amount of charge input. These pulses are recorded, via CAMAC, by the computer and by the 2000 series scalers for cross checking.

2.7 Experimental Running

2.7.1 Two-Energy Magnet Cycling

The simplest way in which one could collect data from the apparatus would be to run at energy E_1, reset the beam-line, run at energy E_2, etc., covering the entire energy range, one energy setting at a time. This would be fine in the ideal world, however, the linac settings are apt to drift slightly during a run, affecting the energy spread of the beam or the angle at which the beam enters the energy defining magnets (referred to henceforth as "LM1--4") causing a drift in bremsstrahlung end-point energy. Fig. 2.16 shows what happens to the difference in yields given a small random drift in E_1 and E_2. However, if the two energies E_1 and E_2 are kept a fixed amount apart, the

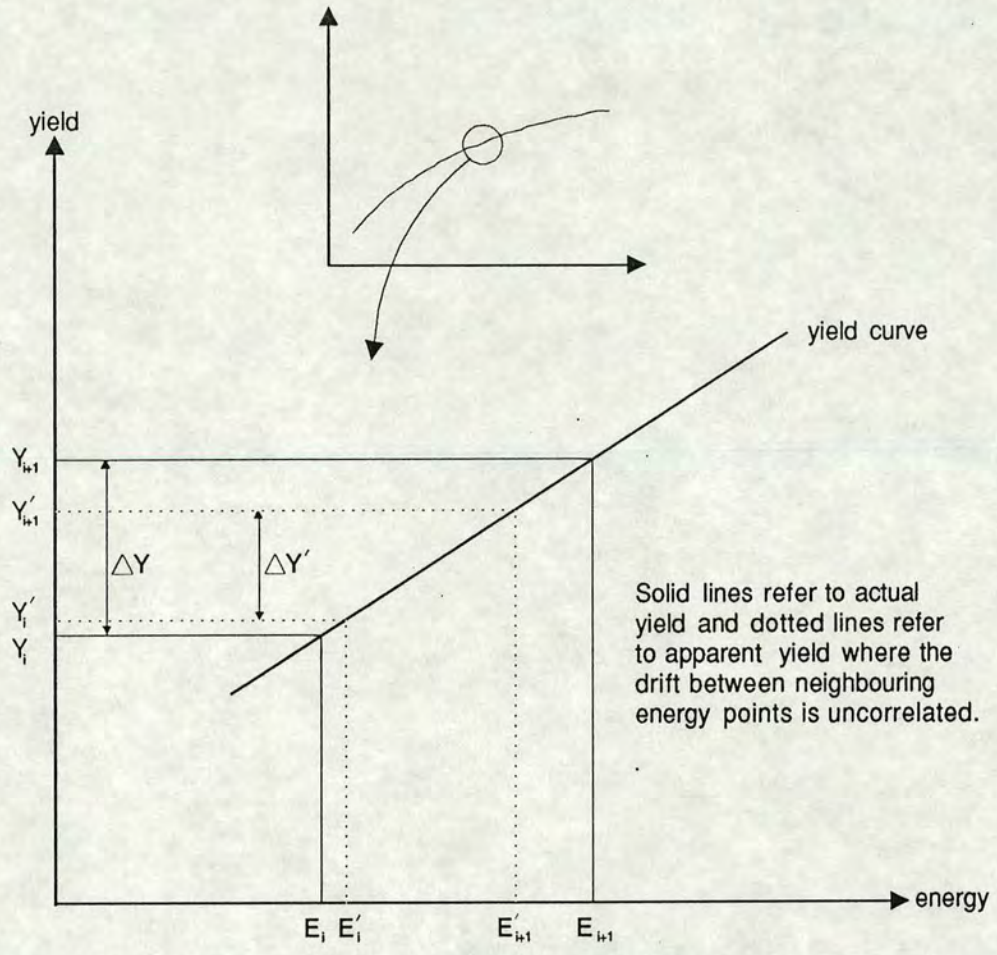

Figure 2.16: Drift in the yield for two different energies.

difference is much less, assuming an approximately linear change in yield over a small energy change (see Fig. 2.17). The answer, therefore, is to run simultaneously at the two energies, E_1 and E_2 and look at the difference. In reality, the closest way to achieve this is to run at E_1 for a short time (*e.g.*~1 minute, which is much shorter than the time-scale of the electron beam drifts), then at E_2 for the same length of time and repeating the cycle throughout the run. This method is referred to as *two-energy magnet cycling*.

This is achieved by placing the magnets LM1--4 under computer control, which allows the magnets to be switched between the two field settings during data acquisition. Two variable resistances are switched in and out, alternately every minute, by mercury-wetted relays (see Fig. 2.18) to increment or decrement by a small amount the mean field set by the

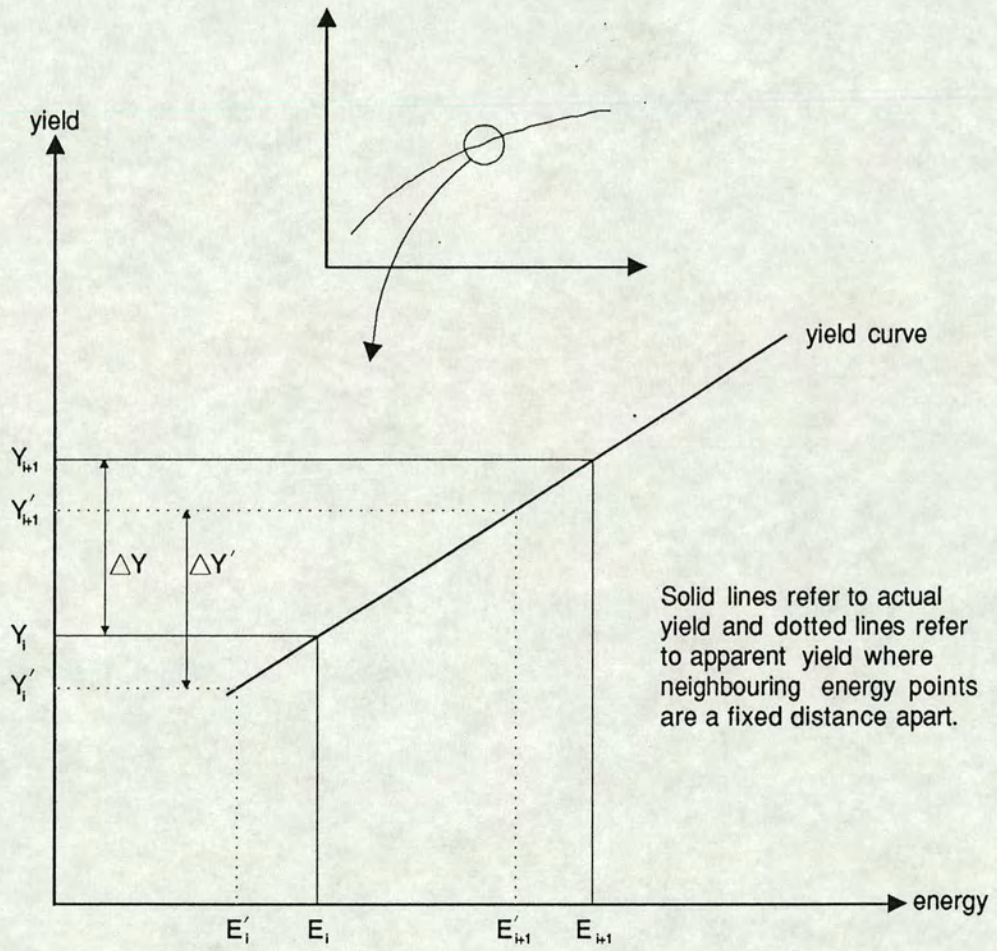

Figure 2.17: Drift in the yield for two different energies a fixed distance apart.

coarse and fine adjustments and measured by a Rawson-Lush rotating coil gaussmeter (see § 2.7.5). It is by this control of current to the magnets that the two energies, E_1 and E_2, can cycled between during a run. Clearly, to do this procedure properly would require the whole beam to be adjusted, not just the first bending magnets, however, the beam spot is set-up at the beginning of each run to move as little as possible upon cycling so small energy change cycles are acceptable using this procedure. It is for this reason that the largest practical energy change used is ~ 100 keV.

Data is thus taken at energies E_1 and E_2, then the coarse and fine adjustments altered to take data at E_2 and E_3, then E_3 and E_4, and so on until the entire energy range is covered. In theory, the higher energy data of one run should agree with the lower energy data of the next and so provide a good check of consistency throughout the experiment.

2.7.2 Data Acquisition

Data for this experiment were taken between 5.6 MeV and 10 MeV *i.e.* from fission threshold upwards. Below 5.6 MeV the cross section is too small to collect sufficient statistics using this set-up. The range up to 8 MeV was covered in 100 keV steps and above this in 200 keV steps. Where possible resonances were indicated, (5.8 -- 6.5 MeV), 50 keV steps were used.

The beam line is set up for each energy pair in order to optimise the beam spot on the target. The position of the beam can be inferred in several ways:

- Scintillators can be moved in and out of the beam at the positions marked "S" in Fig. 2.3. Each scintillator has a cross marked on it in order that the beam be steered centrally.

- Beam scrapers, marked "Sc" in Fig. 2.3 indicate whether the beam is grossly off-centre, implying that the beam should be steered to give the minimum signal on the scrapers.

- Beam position monitors, marked "PM" in Fig. 2.3 consist of two ferrite

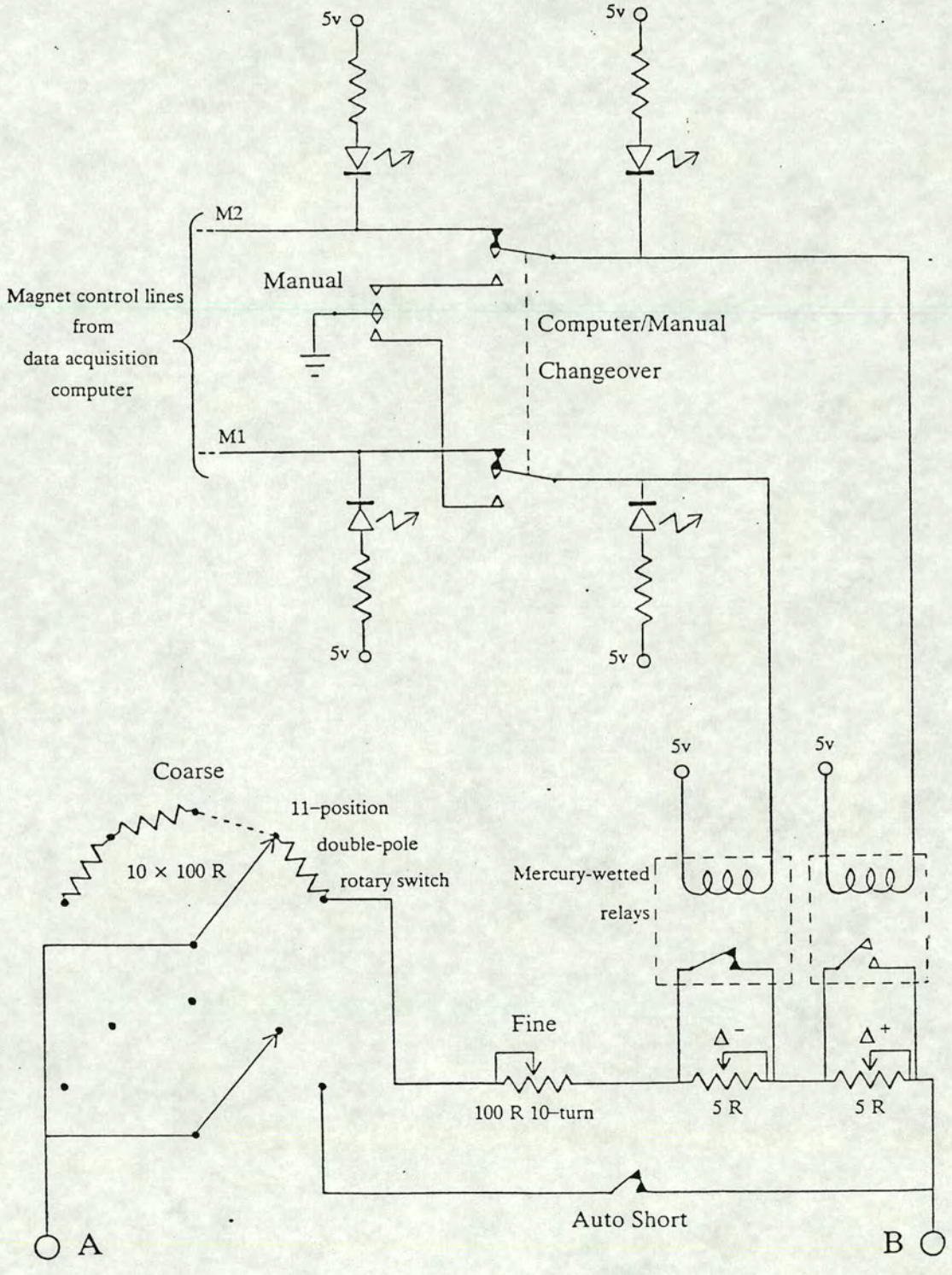

Figure 2.18: The magnet set-up.

rods with a coil wound around them. By inverting one coil signal and adding to the other, minimisation of the total signal gives a centralised beam.

- Beam toroids marked "T" in Fig. 2.3 measure the current in the beam and the beam spread and so indicate whether the beam is properly focussed and has been optimally steered through the machine.

- A dose monitoring film badge, mounted in a specially made frame which can be fixed in the dummy can where the target would be situated, indicates whether the beam spot is passing entirely through the target. After a short exposure to the beam, the badge is developed giving a black spot the same size as the beam. Obviously, the beam must pass entirely through the target otherwise the P2 chamber would be measuring a certain amount of flux which did not intercept the target and suggest a smaller cross section than was actually the case.

- The P2 chamber, to a lesser extent, can be used to infer an optimum beam in that a maximum P2 signal suggests a central beam.

The beam line is set up such that the spot on the scintillator at the gold radiator position moves as little as possible when switching between the two magnet positions.

Data is taken in the form explained in § 2.5.1 whereby a histogram of neutron multiplicities is incremented for both spectrum and background gates and recorded separately for the two energies of the run. The time for each run depends upon whether data is taken above or below the (γ, n) threshold and the magnitude of the cross section. For low energies, the cross section is very small and data needs to be taken for a large fraction of a day to give $\sim 10^5$ (γ, f) neutrons per energy setting. Moving up to the (γ, n) threshold the runs take about 5 -- 6 hours. Below the (γ, n) threshold, one needs only to infer the number of 0 neutron fission events from measured multiplicities > 1, however, above this threshold one needs

to infer both the number of 0 neutron and 1 neutron fission events from measured multiplicities > 2. For this reason, ~ 10^6 (γ, f) and (γ, n) neutrons are collected. But now the cross section is getting larger to offset this and runs take ~ 4 hours.

At the end of each run the data is dumped to both disk and line-printer for analysis.

2.7.3 The P2 Background

During the first set of runs taken with the ^{241}Am target, it was found that at high energies as the cross section increased, the beam width needed to be cut back quite severely in order that the event rate stayed within acceptable limits (see § 2.7.4). This was because only one target was available. Had several targets of varying thickness been available, this problem would not have arisen; one would simply switch to a thinner target to reduce the event rate. This resulted in such a low γ-flux that the Brookhaven current integrator was at the limit of its sensitivity. In fact, the slight drift in the Brookhaven zero-point was significant compared with the P2 signal. This led to unreliable P2 current measurements for the very high energy runs. Hence, it was decided for the second set of runs to record this drift in order to give correct P2 readings.

This was done by giving the Brookhaven a positive signal offset (it is not possible to record a negative signal) and recording its current output between magnet changes with the beam off. During magnet changes, the data acquisition computer inhibits the beam and enables the Brookhaven "background" signal. This is recorded along with the time for which this signal is enabled to allow a background rate subtraction from the total P2 current and hence give a correct P2 total charge at the end of the run.

The success of this method was confirmed when good agreement was achieved between the high energy yield of one run and the low energy yield of the next during the second set of runs.

2.7.4 Data Collection Inhibits

During data acquisition, certain criteria need to be met for the data to be acceptable. For this reason the computer receives inhibit signals if these are not met.

For the overlap correction to be valid (where two events may occur within one beam burst) the count rate needs to be kept within a certain range. In fact, usually it is not allowed to vary by more than a factor of 2 from its mean value. As the P2 current is proportional to the count rate, for convenience constraints are placed upon the P2 meter connected to the Brookhaven which has adjustable upper and lower limits. If the needle indicating the current strays outside these limits, a signal is sent out to inhibit data collection.

Similarly, the gaussmeters indicating the two magnet settings have trip limits which are far tighter than that for the P2 current as a drift in the magnet field creates an unacceptable drift in the energy.

Neutron count data is inhibited between magnet settings and also if the number of spectrum and background gates differs from the number of beam starts by more than 4. The user then has the option of continuing data collection or aborting.

2.7.5 Energy Calibration

The electron energy defining system of the 90^0 bend uses the water-cooled slits (see § 2.3.1). The magnetic field at this point is measured by a Rawson-Lush rotating-coil gaussmeter which is both radiation resistant and capable of measuring change of 0.05 gauss in about 300 gauss which is approximately the field strength used in this experiment.

In order to calibrate this system so that a particular field strength corresponds to a particular known electron energy, a nucleus with a well defined (γ, n) threshold is used to provide a reference energy. ^{183}W has a (γ, n) threshold at 6.191 MeV. By placing a target of this material in

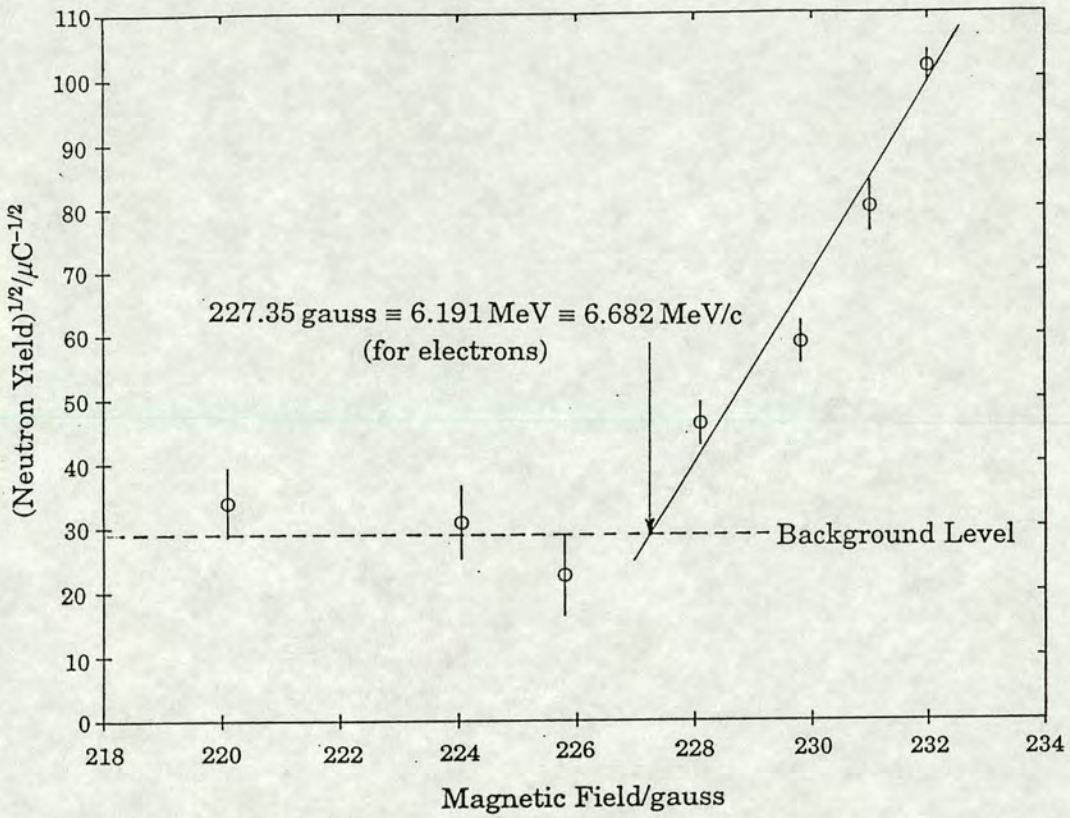

Figure 2.19: A beam energy calibration graph.

the neutron detector and measuring the yield at various field strengths, gradually increasing the defined electron energy so as to straddle the neutron emission threshold, one can establish the reference point. This is done by plotting the square root of the yield against field strength which results in a straight line. Where this straight line crosses the background level gives the threshold field strength. Fig. 2.19 shows such a calibration graph.

The relativistic relation between field strength B_T and electron kinetic energy in MeV T is given by

$$B_T = \frac{B_{cal}}{6.682}\sqrt{T^2 + 2mT} \tag{10}$$

where B_{cal} is the reference field strength measured in the calibration, 6.682 MeV/c is the momentum of the electron corresponding to 6.191 MeV kinetic energy and the mass of the electron m is measured in MeV.

2.7.6 Magnet Field Stabilisation

For the very fine resolution energy steps, assistance is required to keep the magnet fields within the necessarily very tight upper and lower limits on the gaussmeter inhibits. This is done by computer feedback.

A specially made up computer unit was employed to monitor the LM1--4 field for each magnet setting. Small resistances (0.05 Ω) can be inserted or removed by the computer using relays, in series with those between AB (see Fig. 2.18) to vary slightly the current to LM1--4 in order to keep the field within limits.

2.7.7 The Effect of the γ-Flash

As mentioned before, each beam pulse gives rise to a large γ-flash which produces a large signal in the detector. Even 8 μs after the γ-flash the effect could still be there, reducing the efficiency of the detector. For this reason, 4 scalers are gated on during the spectrum gate at periods 0--2 μs, 2--4 μs, 4--6 μs and 100--200 μs after the opening of the gate. The last 100 μs gate is sufficiently far away from the γ-flash not to be affected but the first three gates record a reduced number of neutron pulses than that expected from the capture time probability distribution and thus can be used to calculate this effect.

In fact, it was found that this effect was negligible in comparison with previous photonuclear experiments carried out with the present set-up due to the much smaller beam cross section and relatively thin target areal cross section. For this reason no correction was made for this effect.

2.7.8 The Background

The background gate does not measure the entire background which occurs during the spectrum gate. The γ-flash, Compton-scattered by the target, gives rise to a certain number of neutrons from photodisintegration of naturally occurring deuterium in the oil. To measure this "γ-flash background"

a *passive* target is used *i.e.* one which scatters γ-rays in the same way as the ^{241}Am target but produces no photoneutrons. To this end, a gold target with an equivalent Compton scattering areal cross section was used. The resulting yield can be used to subtract off the γ-flash background for each multiplicity.

In fact, the effect is quite small in this experiment as, once again, the tighter collimation of the beam than from previous photonuclear experiments using this set-up much reduces the γ-flash.

2.7.9 Typical Signal-to-Noise Rates

Because of the large (α, n) background, the signal-to-noise ratio was not as good as it might have been. The background gate rate was very close to $0.54\,\text{gate}^{-1}$ for all of the runs whereas the spectrum gate rate varied from $\sim 0.01\,\text{gate}^{-1}$ above this background value for the low-rate runs up to $\sim 1.5\,\text{gate}^{-1}$ above the background value for the high rate runs. Most of the runs were made at the low-rate. High-rate and low-rate runs are described in § 3.4.8.

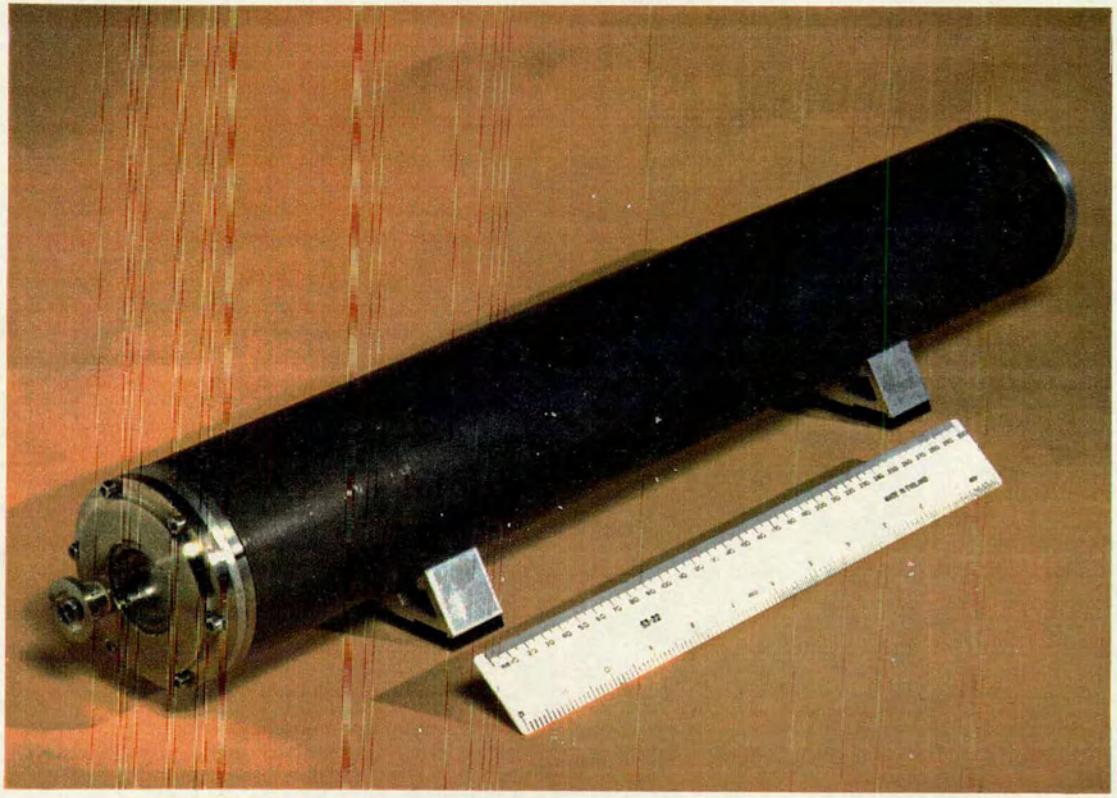

Plate 1 The target can

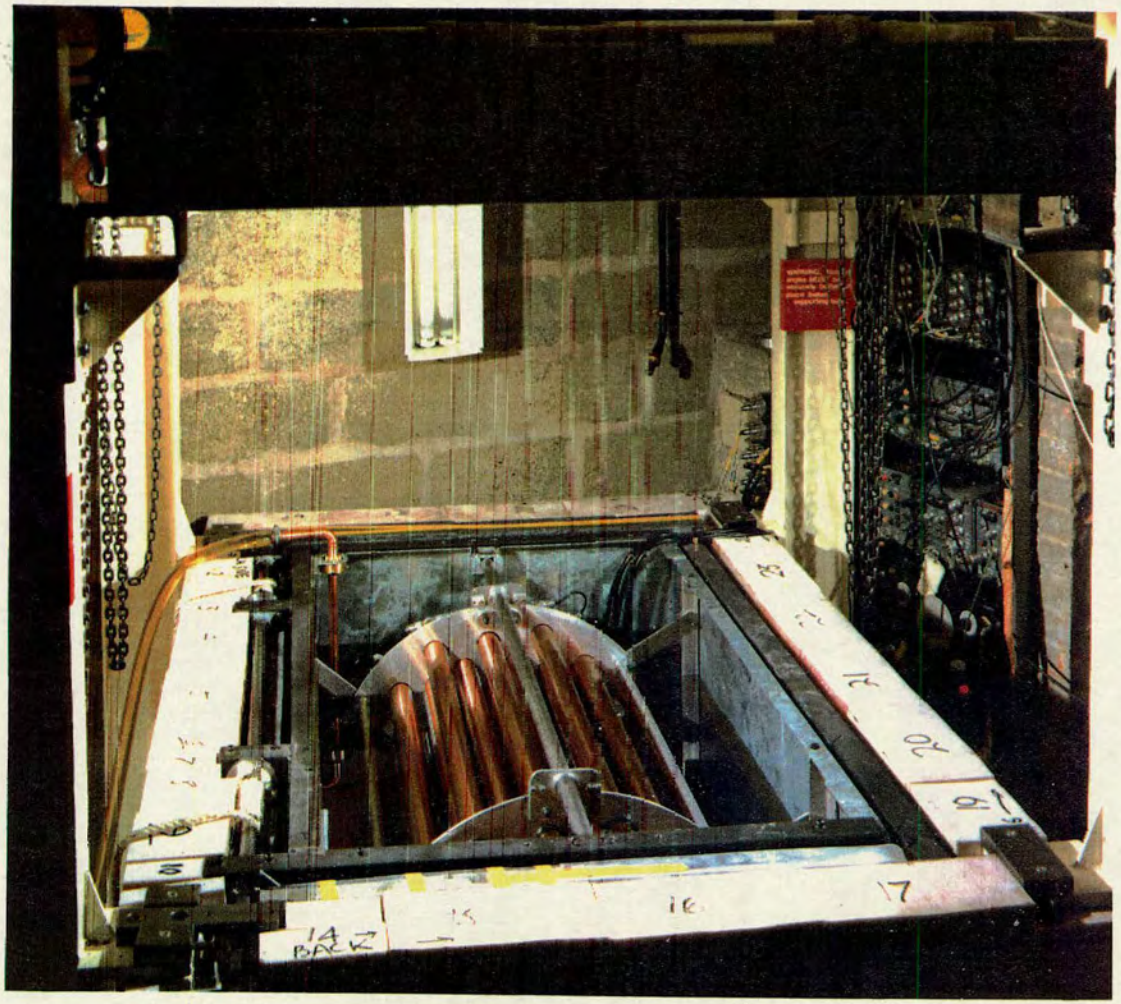

Plate 2 An inside view of the detector

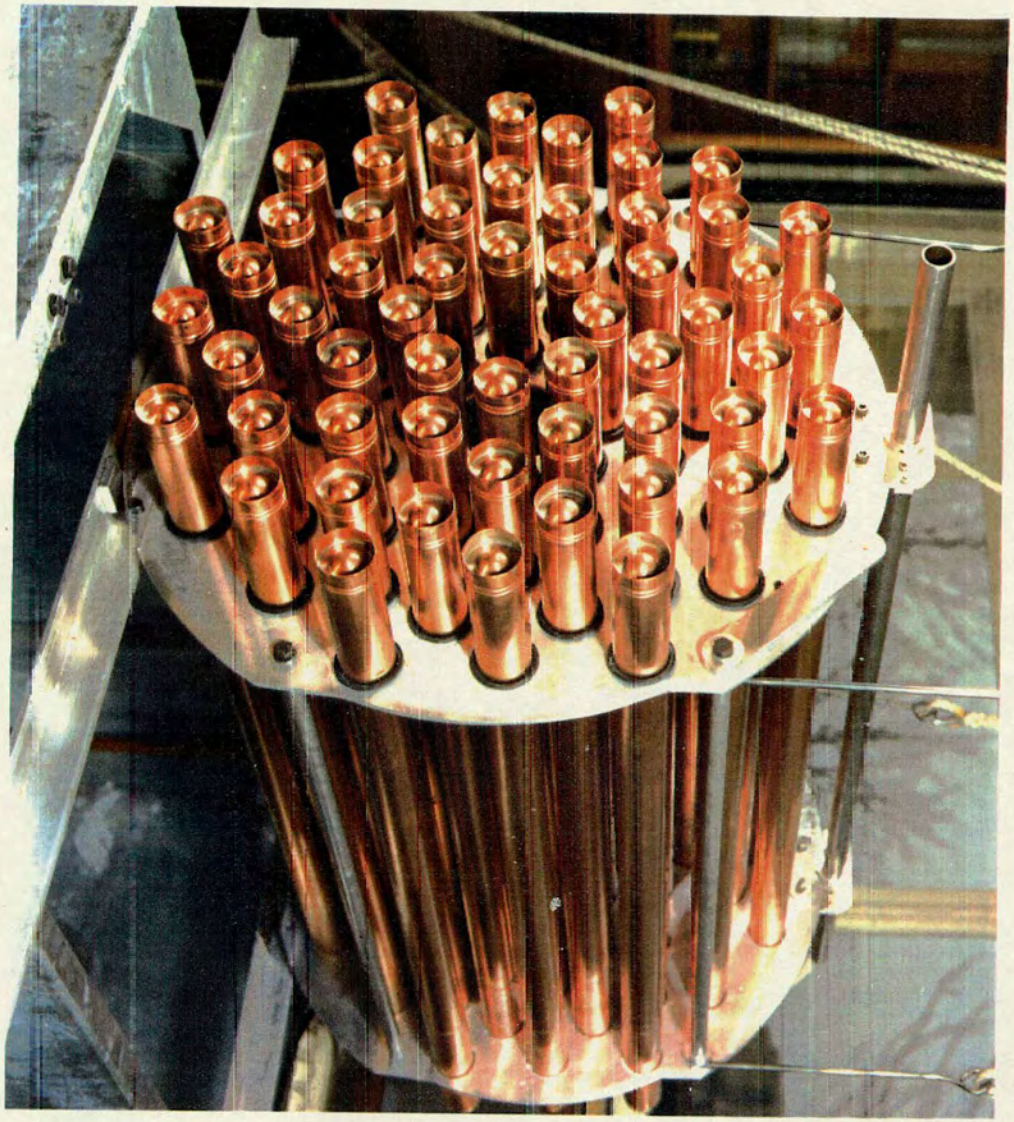

Plate 3 The 56 $^{10}BF_3$ counters

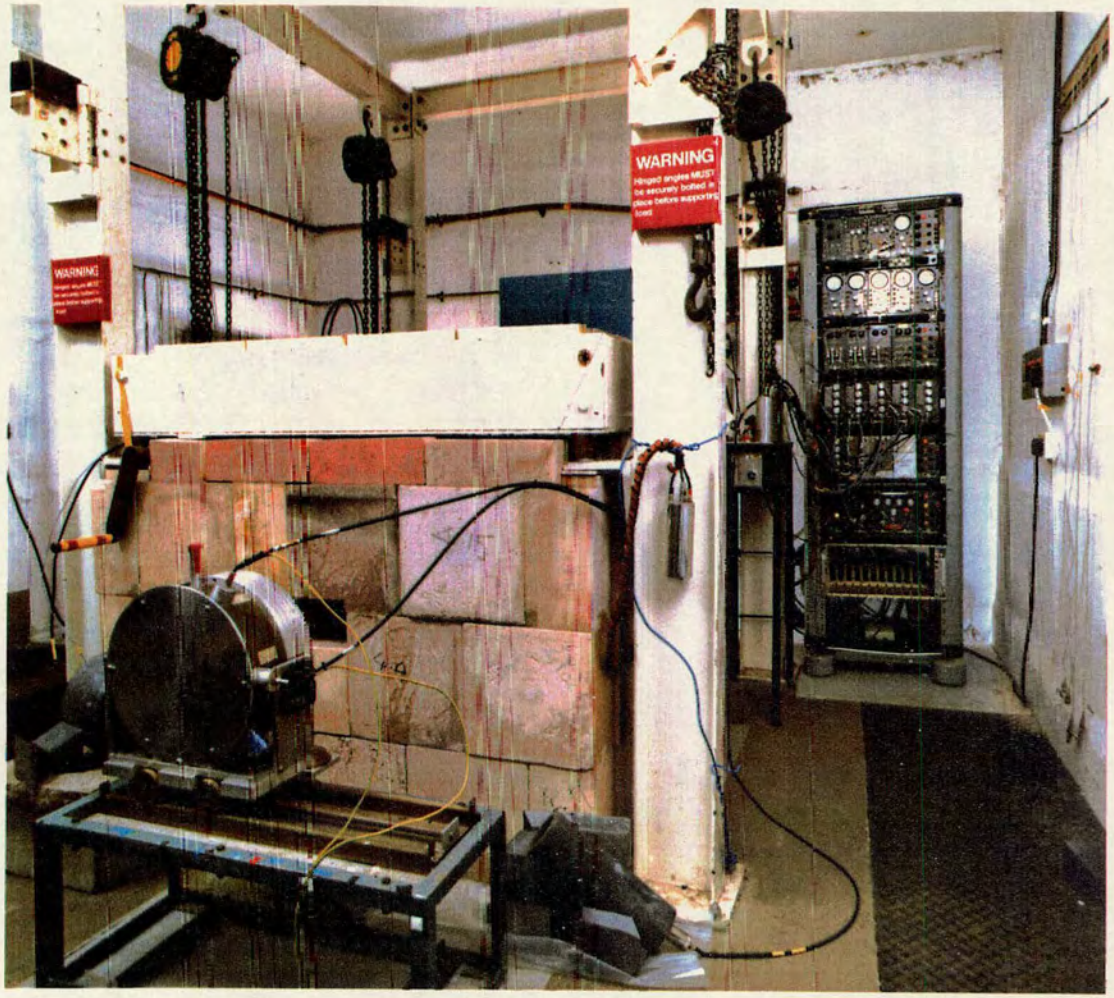

Plate 4 The detector with the P2 chamber in position

Chapter 3

Analysis

3.1 An Outline of the Analysis

Once the raw data have been taken, several stages of corrections and fitting need to be carried out to obtain the cross sections ($\sigma_{\gamma f}$, $\sigma_{\gamma n}$) and the mean number of prompt neutrons per fission, $\overline{\nu}$. The three main stages of the analysis are:

1. Correction of the data --- see below.
2. Fitting the data to find $\overline{\nu}$ and extract the photoneutron and photofission event yields.
3. Unfolding the yields to give the final cross sections.

The data taken consist of a series of energy pair runs at end-point energies between 5.6 and 10.0 MeV, encompassing both the fission and (γ, n) thresholds. For each run the pair data are corrected for:

- Background (which is predominantly from the (α, n) contaminant in the target).
- Dead-time.
- Overlap of events.
- Effect on detector efficiency from gating (covered in § 2.5.2).

- Effect of atmospheric pressure on the P2 chamber response.
- Absorption of the flux incident on the P2 chamber by the target.
- Reduction in the effective thickness of the target due to attenuation of γ flux in the target.

These corrected data can then be passed to the fitting stage. As one does not know the number of multiplicity zero fission events, it is necessary to fit an efficiency corrected theoretical distribution to the multiplicities one and above in order to determine the true number of fission events. Above the (γ, n) threshold, this distribution can only be fitted to multiplicities of two and above, and theoretical fission events of multiplicity one can then be subtracted from the total number of experimental events of multiplicity one to determine the number of (γ, n) events for that run. This theoretical distribution is known as the *Truncated Renormalised Double Gaussian* (TRDG) distribution [Edwa 81] for reasons that will become apparent in the following sections. It is a function of two parameters which are closely related to $\overline{\nu}$ and σ^2 (the variance of the fission neutron multiplicity distribution).

Because the quality of the data was degraded by such a large background and also because $\overline{\nu}$ is believed to vary only slowly with energy, the distribution was fitted to the *sum* of the energy pair data $c_s(i)$ where:

$$c_s(i) = c_u(i) + c_l(i) \qquad i = 1, 7 \tag{11}$$

where $c_u(i)$ and $c_l(i)$ are the number of events of multiplicity i in the upper energy and lower energy of the energy-cycled run pair respectively. The sum distribution is well defined with good statistics but is un-normalised. However, the *difference* distribution $c_d(i)$ given by:

$$c_d(i) = c_u(i) - c_l(i) \qquad i = 1, 7 \tag{12}$$

reflects accurately the change in events going from the lower to the upper distribution but has a less well define shaped due to poorer statistics. It is

for this reason that the shape of the theoretical distribution is fitted to the sum distribution and normalised by the difference distribution.

One then has a series of difference yields of (γ, f) and (γ, n) events which are convoluted with the shape of the bremsstrahlung cross section. These difference yields are then unfolded to give the final cross sections.

3.2 Details of the Corrections

3.2.1 Philosophy of the Corrections

The corrections to the data are done sequentially, correcting for a different effect at each stage. The stages of the corrections are:

$$Q' \rightarrow Q \rightarrow F \rightarrow X \tag{13}$$

where

1. Q' are the uncorrected raw multiplicity data
2. Q are the multiplicity data corrected for background
3. F are the multiplicity data corrected for background and dead-time
4. X are the multiplicity data corrected for background, dead-time and overlap

3.2.2 Background Correction

This corrects for the effect of a background count and a beam-induced count registering as a multiplicity 2 event in the spectrum gate, a background count and two beam-induced counts appearing as a multiplicity 3 event *etc.* As mentioned above, the background rate in this experiment was quite large, often much larger, in fact, than the foreground event rate and involves by far the greatest correction factor. This background rate degraded the quality of the data and gave rise to errors much larger than was desirable. This can be seen by taking the case where there are x total background

events and $x + \delta$ total foreground *detected* events (*i.e.* true + background) where δ is much smaller than x. This gives rise to a background subtracted total of events given by (to a first approximation) $\delta \pm (2x)^{1/2}$. Clearly, the error on δ is quite large.

If one now considers multiplicity data, one can express the probability of seeing a multiplicity n event in terms of probabilities of background multiplicities and true event multiplicities *i.e.*

$$Q'_0 = Q_0 B_0 \tag{14}$$

$$Q'_1 = Q_0 B_1 + Q_1 B_0 \tag{15}$$

$$Q'_2 = Q_0 B_2 + Q_1 B_1 + Q_2 B_0 \tag{16}$$

$$\vdots$$

$$Q'_n = \sum_{j=0}^{n} Q_j B_{n-j} \tag{17}$$

where Q'_i, Q_i and B_i are the probabilities of observed multiplicity i events, true multiplicity i events and background multiplicity i events respectively. These expressions assume that the dead-time is negligible. If one takes account of the fact that background events and true events detected within a time τ (the overall deadtime of the detector - see Eq. 20) will not be registered as individual events, Eq. 17 is modified and becomes [Baro 66]:

$$Q'_n = \sum_{j=0}^{n} Q_j \sum_{p=n-j}^{p_{max}} B_p P_{j,p}^{p+j-n} \tag{18}$$

$$P^k_{n,p} = k! C^k_n C^k_p r^k P^0_{n-k,p-k} \tag{19}$$

where $r = 2\tau/T$ (T is the gate width) and C^k_m is the binomial coefficient $k!/m!(k-m)!$. $P^k_{n,p}$ is the probability of k coincidences[1] when there are n true counts and p background counts within a gate and is found by the recurrence relation in Eq. 19 noting that $P^0_{0,1}$ is equal to 1.

[1]A coincidence in this case refers to a 2-fold coincidence, that is when two counts occur very close together in time within the dead-time τ and so register as one count so if $n = 1$ and $p = 1$ then k could be 1 or 0 corresponding to one coincidence or no such coincidences. This correction is not valid for 3-fold coincidences which are considered to be rare enough so as to be of no consequence.

The overall dead-time for the detector τ is a function of the dead-times of the individual rings (τ_i) and is smaller than for any individual ring. This is because each ring is processed separately. The overall dead-time is given by:

$$\tau = \sum_{i=1}^{5} \tau_i f_i^2 \tag{20}$$

where f_i is the fraction of counts detected in ring i. Typically, τ_i is ~2.05 μs and τ is ~0.59 μs.

Q_j in Eq. 18 is solved firstly with $n = 0$ for Q_0 then $n = 1$ *etc.* to give the background corrected probabilities of observing j counts in the spectrum gate.

As the background due to the γ-flash was very small (<0.5 % of the foreground) due to tight beam collimation and relatively small target areal cross section, it was assumed that the background was, to a very good approximation, due entirely to the (α, n) fluorine contaminant in the target. Hence, by taking all the runs of a particular efficiency and averaging the background rate, one could obtain the mean background rate for all runs, thus reducing the error on the background. By assuming a Poisson distribution of multiplicities for each run then

$$B_k = N_{st} \frac{e^{-r} r^k}{k!} \tag{21}$$

with associated errors

$$(\delta B_k)^2 = N_{st}^2 \left[\left(\frac{k}{r} - 1 \right) \frac{e^{-r} r^k}{k!} \right]^2 (\delta r)^2 \tag{22}$$

where B_k is the number of background events of multiplicity k, N_{st} is the number of starts for the run in question and r is the mean background rate. In this way, the error on the background can be reduced by a factor of ~ 10 from the that which one would obtain using the background measured for each individual run distribution.

3.2.3 Dead-Time Correction

This corrects for the effects of the dead-time of the counting system on individual beam-induced counts whereby such counts occurring within a

time τ will be counted as one unless this correction is made. Note that although one has already included the effect of dead-time in subtracting background counts as described in the previous section, one must also correct for the effects on beam-induced counts. This correction is of a similar form to the background correction. Taking the background corrected (but not dead-time corrected) probabilities from the previous section (Q_n), one can obtain the background and dead-time corrected probabilities (F_n) from the relation [Baro 66]

$$Q_n = \sum_{p=0}^{n} F_{n+p} P^p_{n+p} \tag{23}$$

where P^k_n is the probability of k coincidences when n neutrons are captured and is given by:

$$P^k_n = \frac{n!\, s^k}{k!\, 2^k (n-2k)!} P^0_{n-2k} \tag{24}$$

where

$$s = 2\tau \int_0^T P'^2(t) dt \tag{25}$$

given that $P'(t)$ is the probability that a neutron is detected between t and $t + dt$ after the opening of the gate, and is a function of the capture time probability $P(t)$ (see § 2.5.2) such that

$$P'(t) = \frac{P(t + t_{open})}{\int_{t_{open}}^{t_{close}} P(t) dt} \tag{26}$$

where t_{open} and t_{close} are the opening and closing times of the gate respectively. Assuming that $F_n = 0$ for $n \geq 8$[2], then all other F_n's can be found in Eq. 23 working down from F_8.

3.2.4 Overlap Correction

This correction is to compensate for the effect of two or more events occurring within the same beam burst being registering as one event. For example, two events each of multiplicity 1 will be registered as one event of multiplicity 2, one event of multiplicity 1 and another of multiplicity 2 will

[2]This assumes that one can neglect events of multiplicities 8 and above, which is a reasonable assumption from the statistics.

be registered as one event of multiplicity 3, *etc.* Although the event rate is kept quite low, such overlaps still occur with finite probability. One must therefore take the background and dead-time corrected probabilities from the last section (F_n) and correct them to give the true average number of multiplicity i events per gate (X_i). Following the correction made by Fréhaut [Freh 76], if the quantities X_i are small (which has been ensured for this experiment) and the distribution $R_{i,j}$ follows a Poisson distribution then for a mean rate of multiplicity i events, X_i, then $R_{i,j}$ which is the probability of j events of multiplicity i occurring per beam burst is given by

$$R_{i,j} = \frac{(X_i)^j}{j!} e^{-X_i} \tag{27}$$

Hence the quantities F_n are functions of $R_{i,j}$ such that

$$F_0 = R_{1,0} R_{2,0} R_{3,0} \ldots = \prod_{i=1}^{\infty} e^{-X_i} \tag{28}$$

$$F_1 = R_{1,1} R_{2,0} R_{3,0} \ldots = X_1 F_0 \tag{29}$$

$$\begin{aligned} F_2 &= [R_{1,0} R_{2,1} + R_{1,2} R_{2,0}] R_{3,0} R_{4,0} \ldots \\ &= (X_2 + \tfrac{1}{2} X_1^2) F_0 \end{aligned} \tag{30}$$

$$\vdots$$

$$F_n = \sum_{\lambda} [\prod_{k=1}^{\infty} R_{k,j}] \tag{31}$$

where the sum is taken over all sets of k,j pairs (each labelled by the index λ) $\sum k_\lambda j_\lambda = n$. To put it another way, the sum contains as many terms as there are different possibilities of fulfilling the condition $\sum_{k=1}^{\infty} kj = n$. The expressions above (Eqs. 28--31) can be reduced to the recurrence relation

$$F_n = \frac{1}{n} \sum_{i=1}^{n} i F_{n-i} X_i \tag{32}$$

and starting from $F_1 = X_1 F_0$, all X_i's can be evaluated giving the background, dead-time and overlap corrected probability of multiplicity i events.

3.2.5 Atmospheric Correction to P2 Chamber Response

As stated previously, the response of the P2 ionisation chamber is dependent on the temperature and pressure. The temperature is controlled by the

air-conditioning in the experimental block-house to within $\pm 1^0$C. This represents an error on the measured P2 charge of less than 0.5 % due to temperature fluctuations. However, a correction needs to be made for changes in atmospheric pressure. For each run a barograph records the current pressure and the correction to the P2 recorded charge is in direct proportion to the pressure, *i.e.*

$$P2_{\text{corr.}} = \frac{P_{\text{atm}}}{760\,\text{mm Hg}} P2_{\text{uncorr.}} \tag{33}$$

where $P2_{\text{corr.}}$ and $P2_{\text{uncorr.}}$ are the corrected and uncorrected P2 charges respectively, and P_{atm} is the average atmospheric pressure during the run. This correction results from the fact that the response of the chamber is quoted at 760 mm Hg [Prui 62]. A pressure change as large as 40 mm Hg can occur during a series of runs which results in up to ~ 5 % correction to the P2 recorded charge.

3.2.6 Target Attenuation of Beam

Because of the finite thickness of the target, a certain amount of the γ flux will be absorbed by the target and hence the measured P2 current will be reduced due to the presence of the target.

The charge produced in the P2 chamber per incident electron on the gold bremsstrahlung radiator is given by the expression

$$q' = \int_0^{E_e} e^{-\mu_f(k)t_f} N(E_e, k) e^{-\mu_t(k)t_t} S(k) k dk \tag{34}$$

where $N(E_e, k)dk$ is the number of γ rays, per incident electron, for bremsstrahlung end-point energy E_e, $S(k)$ is the response of the P2 chamber (in units of charge per unit energy) [Prui 62], and the exponential factors are absorption due to the air and beam line windows, and the target with:

- μ_f : the coefficient of γ absorption by the air and beam line windows.
- t_f : the thickness of air and beam line windows.
- μ_t : the coefficient of γ absorption by the target.

- t_t : the target thickness.

In the absence of any absorption by the target, Eq. 34 would become:

$$q = \int_0^{E_e} e^{-\mu_f(k)t_f} N(E_e, k) S(k) k dk \tag{35}$$

Hence the corrected P2 charge (that which would be observed without target absorption) would be:

$$Q_{\text{corr.}} = Q_{\text{uncorr.}} \frac{\int_0^{E_e} e^{-\mu_f(k)t_f} N(E_e, k) S(k) k dk}{\int_0^{E_e} e^{-\mu_f(k)t_f} N(E_e, k) e^{-\mu_t(k)t_t} S(k) k dk} \tag{36}$$

where $Q_{\text{corr.}}$ and $Q_{\text{uncorr.}}$ are the corrected and uncorrected charges respectively. This expression can be evaluated numerically.

3.2.7 Effective Target Thickness

An additional effect of the target thickness is that upstream side of the target sees more γ flux than the downstream side, due to the attenuation, seemingly reducing the effective target thickness. The total number of photonuclear events for a target with D nuclei per unit volume and cross section $\sigma(k)$ is given by:

$$\int_{k=0}^{E_e} \int_{x=0}^{x=t_t} N(E_e, k) e^{-\mu_f(k)t_f} e^{-\mu_t(k)x} D\sigma(k)\, dx\, dk \tag{37}$$

which, when integrated over the target thickness, x, becomes:

$$\int_{k=0}^{E_e} N(E_e, k) e^{-\mu_f(k)t_f} R(k) D\sigma(k) t_t\, dk \tag{38}$$

where $R(k)$ is the ratio of the effective to the actual target thickness for γ energy, k and is given by:

$$R(k) = \frac{1 - e^{-\mu_t(k)t_t}}{\mu_t(k)t_t} \tag{39}$$

Therefore, if one carries out the analysis forgetting about $R(k)$ initially, one finishes with the value $R(k)\sigma(k)$ and it only remains to correct this value using Eq. 39 to obtain the final cross section, $\sigma(k)$. For the target in this experiment, the ratio is virtually independent of k over the energy range studied and results in a ratio, $R(k)$ of ~ 0.99.

3.3 Calculating the Errors

To use the standard propagation of errors formulae for all the corrections described above would be quite complicated and involved, especially if the correlations between errors are included. The method adopted instead [Hawk 86] is to correct the data as normal initially, then add a random but Gaussian weighted amount to the data and recorrect where the Gaussian has mean 0 and standard deviation of the error on the initial data (*i.e.* square root of the events, except for when the generated background is used in which case the error in Eq. 22 is used). This procedure is repeated a number of times where 24 was considered sufficient and the standard deviation of these 25 loops gives the error on the initially corrected data.

In addition the 24 "perturbed" results show how the errors are correlated and can be used to generate a variance-covariance matrix:

$$V_{ij} = \frac{\sum_{k=1}^{k=25}(c_{ik} - \overline{c_i})(c_{ij} - \overline{c_j})}{24} \tag{40}$$

where c_{ik} is the i^{th} result in loop k and $\overline{c_i}$ is the mean value of the i^{th} result over the 25 loops. The off-diagonal elements carry the correlation information *i.e.* if all the off-diagonal elements were zero then the errors would be uncorrelated. This matrix is used in the TRDG fitting procedure for finding the generalised value of χ^2 when errors are correlated.

3.4 Fitting the Data

Once the data have been corrected, they then need to be fitted in order to find the true number of fission events in each run for the reasons outlined in § 3.1.

The TRDG distribution will be described and the fitting procedure outlined in the following sections. Firstly, the predecessor of the TRDG distribution, the Terrell distribution, will be described.

3.4.1 The Terrell Distribution

Terrell [Terr 57] considered the fission process as a series of random fluctuations whereby small amounts of energy are lost or gained by fission fragments. From the central limit theorem the fragments will have excitation energy distributed as a Gaussian, thus:

$$p(E)dE = \frac{1}{\sqrt{2\pi}(\Delta E)} e^{-\left[\frac{(E-\overline{E})^2}{2(\Delta E)^2}\right]} dE \tag{41}$$

which can allow the possibility of negative excitation energies and causes problems with this formalism which will be mentioned later in this section. By assuming that all the fission neutrons come from one *effective* fission fragment whose energy can be described by Eq. 41 and if δE is the average reduction in energy accompanying the release of a neutron, then the probability of emission of ν neutrons is given by

$$\sum_{n=0}^{\nu} p(n) = \frac{1}{\sqrt{2\pi}} \int_{-\infty}^{(1+\nu)\delta E} \frac{1}{(\Delta E)} e^{-\left[\frac{(E-\overline{E})^2}{2(\Delta E)^2}\right]} dE \tag{42}$$

If the final excitation energy of the fragment after emission of all fission neutrons is on average ~ $\delta E/2$ and ν_p is the number of neutrons emitted from a fragment with initial excitation energy of $\overline{E}$, then

$$\frac{\overline{E}}{\delta E} = \nu_p + \tfrac{1}{2} - b \tag{43}$$

where b is a small correction discussed below. If

$$f(x) = \frac{1}{\sqrt{2\pi}} \int_{-x}^{x} e^{-\left[\frac{t^2}{2}\right]} dt \tag{44}$$

and one defines

$$W = \frac{\Delta E}{\delta E} \tag{45}$$

then

$$\sum_{n=0}^{\nu} p(n) = \tfrac{1}{2} + \tfrac{1}{2} f[(\nu - \nu_p + \tfrac{1}{2} + b)/W] \tag{46}$$

and ν_p can be closely identified with the mean value $\overline{\nu}$ of the distribution by writing

$$b \approx \tfrac{1}{2} - \tfrac{1}{2} f[(\nu_p + \tfrac{1}{2})/W] \tag{47}$$

Eq. 46 is a function of just two parameters: ν_p (which is associated with $\bar{\nu}$) and W, the root mean square width of the total excitation energy distribution in units of δE. The variance of the multiplicity distribution is related to this quantity W by Sheppard's correction:

$$\sigma^2 = W^2 + \frac{1}{12} \tag{48}$$

Unfortunately, there are problems with the Terrell formalism, as pointed out by Edwards *et al.*[Edwa 81].

1. The theoretical value of ν_p of the Terrell distribution deduced from fitting experimentally measured multiplicity distributions can differ from the experimental $\bar{\nu}$ value for spontaneously fissioning isotopes by up to 3.5 %.

2. Similarly estimates of the variance obtained by fitting the distribution to measured multiplicity distributions can differ from the experimental values by up to 10 %.

3. The Terrell distribution consistently over-estimates multiplicity 0 events, sometimes by more than 100 %.

4. Poor fits to the data were obtained in several cases with consistently positive individual χ's of fit for multiplicities of 1 and above rather than a random distribution about 0.

It was deduced that having negative excitation energies with a non-zero probability was having a detrimental effect on the distribution. In order to improve the fit, it was decided to truncate the distribution to disallow non-zero probabilities of negative energies, and to renormalise the distribution.

3.4.2 The Truncated Renormalised Gaussian Distribution

If $p(E) = 0$ for $E < 0$ in Eq. 41, normalisation gives

$$p(E)dE = \frac{R}{\sqrt{2\pi}(\Delta E)} e^{-\left[\frac{(E-\overline{E})^2}{2(\Delta E)^2}\right]} dE \tag{49}$$

where

$$R = \left[\int_0^\infty p(E)dE\right]^{-1}, \quad E > 0 \tag{50}$$

$$R = 0, \quad E < 0 \tag{51}$$

This eliminates the need for Terrell's *ad hoc* correction, b and Eq. 43 becomes

$$\frac{\overline{E}}{\delta E} = \nu_p + \tfrac{1}{2} \tag{52}$$

and now Eq. 46 becomes

$$\sum_{n=0}^{\nu} p(n) = \frac{R}{2}\left\{f\left[\frac{\nu - \nu_p + \frac{1}{2}}{W}\right] + f\left[\frac{\nu_p + \frac{1}{2}}{W}\right]\right\} \tag{53}$$

This formula still assumes evaporation from one effective fission fragment. If one assumes neutron evaporation from 2 separate fragments, which is a more correct physical assumption, then the TRDG is obtained.

3.4.3 The Truncated Renormalised Double Gaussian Distribution

Assuming neutron evaporation from two fragments, the probability of getting a total of ν neutrons is now:

$$p'(\nu) = \sum_{i=0}^{\nu} p(i)p(\nu - i) \tag{54}$$

This, therefore, gives the TRDG distribution:

$$\begin{aligned} p'(\nu) = & \sum_{i=0}^{\nu}\left(\frac{R^2}{4}\right) \\ & \times\left\{f\left[\frac{i - (\nu_p/2) + \frac{1}{2}}{W/\sqrt{2}}\right] - f\left[\frac{i - (\nu_p/2) - \frac{1}{2}}{W/\sqrt{2}}\right]\right\} \\ & \times\left\{f\left[\frac{\nu - i - (\nu_p/2) + \frac{1}{2}}{W/\sqrt{2}}\right] - f\left[\frac{\nu - i - (\nu_p/2) - \frac{1}{2}}{W/\sqrt{2}}\right]\right\} \end{aligned} \tag{55}$$

where

$$R = \left(\tfrac{1}{2} + \tfrac{1}{2} f\left[\frac{\nu_p/2 + \frac{1}{2}}{W/\sqrt{2}}\right]\right)^{-1} \tag{56}$$

However, now there is no direct association between $\overline{\nu}$ and ν_p and between σ^2 and W. ν_p and W are now simply adjustable parameters of the distribution. $\overline{\nu}$ and σ^2 are calculated from

$$\overline{\nu} = \sum_{\nu=0}^{\infty} \nu p'(\nu) \tag{57}$$

$$\sigma^2 = \sum_{\nu=0}^{\infty} (\nu - \overline{\nu})^2 p'(\nu) \tag{58}$$

In fact, it does turn out that ν_p is quite close to $\overline{\nu}$ and W to the variance.

The TRDG distribution fits the spontaneous fission multiplicity distributions very well, much better than the Terrell distribution. For this reason, and the fact that there are still only 2 adjustable parameters, this is the distribution used to analyse the present data.

3.4.4 Efficiency Correcting the TRDG

The data taken above the (γ, n) threshold will include neutrons of two different mean energies (fission neutrons and photoneutrons), which will in turn have slightly different efficiencies of detection as it will be remembered from § 2.5 that the efficiency of the detector is a slowly decreasing linear function of mean neutron energy. For this reason, the experimental multiplicity distribution cannot be just corrected to the form it would have for a 100 % efficient detector. Instead, the TRDG multiplicity probabilities are weighted for a *gated* fission neutron detection efficiency of $\varepsilon_{\gamma f}$ following the formula of Baron *et al.* [Baro 66]:

$$q(i) = \varepsilon_{\gamma f} \sum_{j=1}^{j_{max}} C_i^j (1 - \varepsilon_{\gamma f})^{j-i} p'(j) \tag{59}$$

where $p'(j)$ is the TRDG probability distribution of Eq. 55, $q(i)$ is the efficiency weighted TRDG distribution, C_i^j is the normal binomial coefficient and j_{max} is the highest probability considered (in this case, 7).

3.4.5 Data Fitting

If the theoretical distribution is in the form of probabilities, $q(i)$, and the corrected data multiplicities, $c(i)$, are in the form of actual counts, then the theoretical distribution needs to be converted into counts if the data are to be fitted.

Unfortunately, one does not know the number of 0 neutron fissions (and also 1 neutron fissions above the (γ, n) threshold). So the theoretical probabilities, $q(i)$ are multiplied by a normalisation factor N:

$$N = \frac{\sum_{i=i_{min}}^{i_{max}} c(i)}{\sum_{i=i_{min}}^{i_{max}} q(i)} \tag{60}$$

where $i_{min} = 2$ above the (γ, n) threshold and $i_{min} = 1$ otherwise, and therefore the theoretical fission *count* distribution, $t(i)$ is of the form:

$$t(i) = Nq(i) \tag{61}$$

for $i = 1$ to 7.

Now, one can fit the values, $t(i)$, to the data, $c(i)$ varying the 2 parameters of the TRDG until the minimum χ^2 of fit is achieved. Minimisation is achieved using the Harwell subroutine, VA04A [Powe 64] which can minimise a function of n variables.

If the errors in the corrected data were uncorrelated, χ^2 would have the familiar form:

$$\chi^2 = \sum_{i=i_{min}}^{i_{max}} \left(\frac{t(i) - c(i)}{\delta c(i)} \right)^2 \tag{62}$$

where $\delta c(i)$ is the error on $c(i)$. However, in the present case the generalised form of χ^2 needs to be used, taking account of correlations between errors. This is where the variance matrix, V_{ij} of § 3.3 comes in:

$$\chi^2 = \sum_{ij} r_i V^{ij} r_j \tag{63}$$

where r_i are the residuals such that:

$$r_i = t(i) - c(i) \tag{64}$$

and V^{ij} is the inverse matrix of V_{ij}.

3.4.6 Errors on the Fits

The errors on the values of ν_p and W are calculated in a similar manner to that described in § 3.3 for the corrected data. The fits are repeated with the distributions perturbed by a random amount appropriate to the errors calculated during the correction stage. The standard deviation of the 25 fits then gives the error on the parameters much as before.

3.4.7 Fixing Parameters During Fits

Initially, fits to the experimental multiplicity distributions are carried out allowing both ν_p and W to vary until the lowest χ^2 is achieved. It is found, however, that W has almost a linear dependence with energy. What is more, there is an anti-correlation between ν_p and W so that when ν_p goes up, W goes down and *vice versa*. Therefore, any scatter in W is almost certainly due to random errors and by fixing W to a linear fit and refitting allowing only ν_p to vary, one can eliminate scatter in ν_p whilst also reducing the errors.

In the final fit, as the quality of the data had been degraded in the experiment by such a large background, both ν_p and W were fixed to a linear fit to obtain the cross section with the smallest errors. This can be partly justified as $\overline{\nu}$ (and so ν_p) should in theory have just a linear dependence on energy. For many actinides, (and in this experiment also) there are slight deviations from this hypothesis, however this makes only a small difference to the actual values of the calculated cross sections. Indeed, errors in the cross section are dominated by errors in the corrected yield rather than errors in ν_p and W.

3.4.8 Calculating $\overline{\nu}$, the Number of Fissions and the Number of Photoneutron Events

Once the multiplicity distribution data have been fitted, the appropriate number of photofissions, photoneutron events and $\overline{\nu}$ can be calculated.

As stated in § 3.1, the TRDG is fitted to the *sum* distribution as this has the best statistics and $\overline{\nu}$ is believed to change slowly with energy. Therefore, $\overline{\nu}$ is given by:

$$\overline{\nu} = \sum_{i=1}^{7} ip'(i) \tag{65}$$

where $p'(i)$ (see Eq. 55) is calculated using the best fit values of ν_p and W. However, to find the number of fissions and photoneutron events, one needs to look to the *difference* distribution which accurately reflects the yield difference in going from the lower to the upper energy. As the sum and difference distributions should have almost the same shape then values of ν_p and W should apply equally well to both. For this reason and by analogy with Eq. 60 the number of fissions is given by:

$$N_{\gamma f} = \frac{\sum_{i=i_{min}}^{i_{max}} c_d(i)}{\sum_{i=i_{min}}^{i_{max}} q(i)}. \tag{66}$$

where $q(i)$ (see Eq. 59) has been fitted (with the best values of ν_p and W) to the sum distribution. The number of photoneutron events as then given by

$$N_{\gamma n} = \frac{c_d(1) - t_d(1)}{\varepsilon_{\gamma n}} \tag{67}$$

where $t_d(1)$ is the theoretical number of multiplicity 1 fissions in the difference distribution given by:

$$N_{\gamma f} q(1) \tag{68}$$

and $\varepsilon_{\gamma n}$ is the average efficiency of detecting (γ, n) neutrons.

High- and Low-Rate Runs

It was mentioned in § 2.7.3 that in the first set of runs there were problems with the drift in measuring the P2 current at the very small beam currents used in order to keep the event rate down at higher energies where the yields are higher. This was solved in the second set of runs by measuring the P2 "background" throughout each run. However, for the first set of runs a procedure was followed whereby low-rate (low beam current) and

high-rate (high beam current) runs were carried out at energies greater than 8.0 MeV.

The low-rate runs (at 0.5 MeV intervals) had low enough event rates to be accurately corrected for overlap but had inaccurate values of the P2 current due to drifting. The high-rate runs (at 0.2 MeV intervals) had event rates too large to be corrected for overlap, but were carried out at P2 currents sufficiently high to make drifting negligible and so reflected accurately the absolute yield of neutrons for that run.

Firstly, the low-rate run P2 chamber readings were corrected to give the same overall yield per unit charge using the high-rate runs. Then the low-rate runs were corrected and fitted following the procedures of the previous sections. The final high-rate yields of difference fission and photoneutron events were then normalised to the total corrected low-rate yield of difference neutrons by multiplying the total high-rate yields by the factors:

$$X_{\gamma f} = \frac{N_{\gamma f}}{n_d} \tag{69}$$

$$X_{\gamma n} = \frac{N_{\gamma n}}{n_d} \tag{70}$$

where n_d is the total corrected low-rate yield of neutrons in the difference distribution. These ratios were assumed to have a smooth linear dependence on energy and so a linear interpolation was then made for all energies between these points. In fact, the ratios vary very little over the 8.0 to 10.0 MeV range. For each of the high-rate runs, the total yield of difference neutrons was determined (corrected for all but event overlap). This value when multiplied by $X_{\gamma f}$ and $X_{\gamma n}$ gives the yield of fission and photoneutron events respectively, for the high-rate runs.

3.5 Unfolding the Cross Sections

The yields obtained are essentially the cross sections of interest convoluted with the shape of the bremsstrahlung spectrum. This section describes how

the yields are unfolded to produce the final cross sections as a function of monochromatic photon energy (with finite resolution).

3.5.1 The Shape of the Bremsstrahlung Spectrum

To unfold the cross section one needs to know the shape of the bremsstrahlung spectrum. Figure 3.1 shows the spectrum calculated by Tseng and Pratt [Tsen 79] (dotted line) which assumes an infinitesimally thin radiator and a monochromatic electron beam. This has a cut-off at the electron energy, E_e. In reality, the radiator has thickness and the electron beam has an energy spread so that this cut-off is smeared by various perturbing effects such as energy losses due to ionisation and radiation in the bremsstrahlung radiator as well as the angular distribution of electrons in the incident beam. Findlay [Find 83a] calculated the bremsstrahlung spectrum taking into account these effects and obtained the curve as shown in Figure 3.1 (solid line). This smearing effect has certain consequences in the unfolding process which will be discussed in the following section.

3.5.2 The Mathematics of Unfolding

An accepted method of bremsstrahlung unfolding uses the *Penfold-Leiss Method* [Penf 59].

Setting aside for the moment the two energy magnet cycling technique used in this experiment, if one has measured the yield Y at a bremsstrahlung end-point energy E then

$$Y(E) = \int_{k_{thr}}^{E} N(E,k)\sigma(k)dk \tag{71}$$

where k is the photon energy, k_{thr} the threshold energy for cross section $\sigma(k)$, and $N(E,k)$ is the bremsstrahlung spectrum for end-point energy E and photon energy k. (N.B. This equation neglects various scaling factors which do not affect the argument).

The yield $Y(E)$ is actually measured at a series of discrete energies E_i where $E_i - E_{i-1} = \Delta$ and Δ is the energy bin width. The Penfold-Leiss method

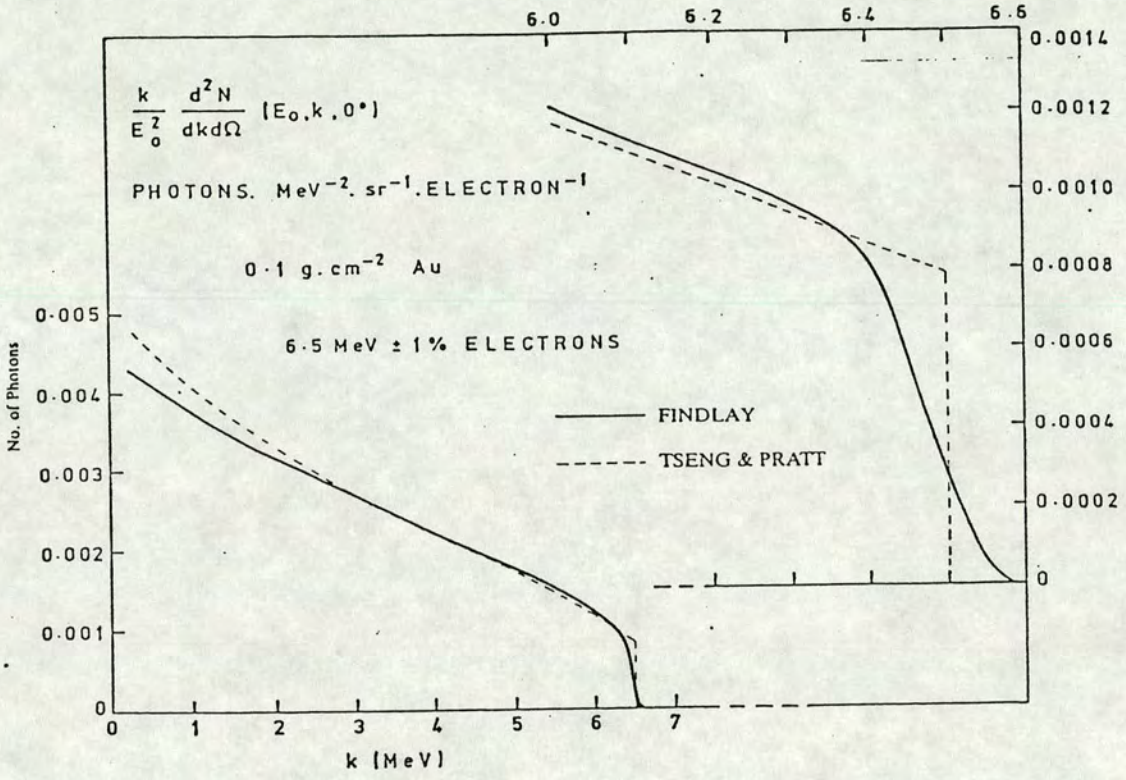

Figure 3.1: The bremsstrahlung spectrum calculated by Tseng and Pratt (dotted line) and Findlay (solid line).

takes appropriate linear combinations of these yields:

$$\sigma_i = \sum_{j=1}^{i} B_{ij} Y(E_j) \tag{72}$$

such that

$$\sigma_i \equiv \sigma[E_i - O(\Delta)] \tag{73}$$

where $O(\Delta)$ is a quantity of the order of Δ. This linear combination assumes that the cross section is very small for $E = E_1$ (the first and lowest energy point) and negligible for any energy less than the first point. B_{ij} is chosen so that

$$\Delta \sum_{j=1}^{i} B_{ij} N(E_j, E_{i'} - \frac{\Delta}{2}) = \delta_{ii'} \tag{74}$$

B_{ij} forms the inverse bremsstrahlung matrix and $\delta_{ii'}$ is the Kronecker delta function. Substituting Eq. 71 into Eq. 72 and noting that $N(E_j, k) = 0$ for $k > E_j$ the cross section, σ_i becomes

$$\begin{aligned} \sigma_i &= \int_{k_{thr}}^{E_i} \left[\sum_{j=1}^{i} B_{ij} N(E_j, k) \right] \sigma(k) dk \\ &= \int_{k_{thr}}^{E_i} T_i(k) \sigma(k) dk \end{aligned} \tag{75}$$

where

$$T_i(k) = \sum_{j=1}^{i} B_{ij} N(E_j, k) \tag{76}$$

is the *weighting function*. This function is basically a linear combination of bremsstrahlung spectra with endpoint energies differing by Δ and should have the following properties:

- It should be zero for $k > E_j$.
- It should have a peak of width ~ Δ at $k = E_i - O(\Delta)$.
- It should converge quickly *i.e.* only the first few terms should be important (so that statistical fluctuations in certain cross section points effect other points as little as possible).
- It should have area unity.

Energy Range (MeV)	Interlaced Energy Step (keV)	Electron Energy Spread (Slit Width) (%)	λ	Photon Energy Resolution (keV)
5.7--6.4	100 (50 keV 2-fold)	$\pm\frac{1}{2}$	1.75	130
5.6--8.0	200 (100 keV 2-fold)	± 1	1.50	220
8.0--10.0	500	± 1	0.75	500

Table 3.1: The resolutions appropriate to each value of λ used to unfold in the present experiment where interlacing is explained in § 3.5.5.

However, because of the smearing at the end of the bremsstrahlung spectrum as shown in Fig. 3.1 for the Findlay calculation, if the interval Δ is about the same size as this spread, the weighting function may give rise to wild oscillations and become unusable as in Fig 3.2 where the resultant weighting function is shown as a solid line. To get around this Findlay [Find 83b] introduced a damping factor, λ which suppresses these oscillations at the expense of the resolution. With this modification Eq. 74 becomes

$$\Delta \sum_{j=1}^{i} B_{ij} N(E_j, E_{i'} - \lambda\Delta) = \delta_{ii'} \tag{77}$$

Fig. 3.3 shows an example of this function made up of added and subtracted bremsstrahlung spectra where, again, the resultant weighting function is shown as a solid line. The greater the value of λ, the greater the "damping width" and the less the resolution. The λ factor becomes more significant for the finer resolution work as shown in Table 3.1. The best values of λ for which the oscillations are suppressed but the resolution preserved are found approximately from the relation

$$\lambda\Delta = \delta E_{\text{spread}} \tag{78}$$

where δE_{spread} is the energy spread of the electron beam incident on the radiator.

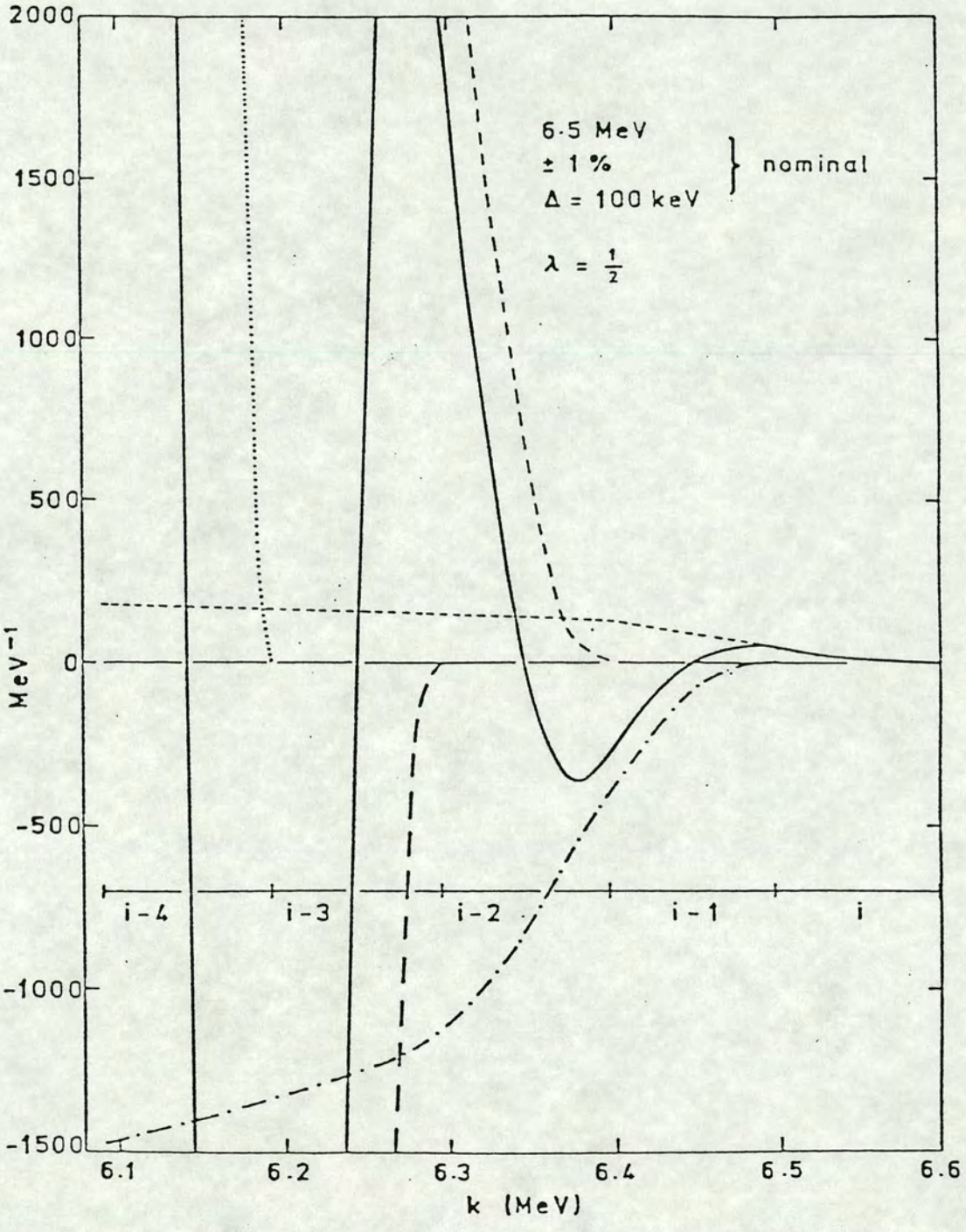

Figure 3.2: Oscillations in the Penfold-Leiss weighting function as the function is forced to go through the midpoint of each bin between i and $i+1$.

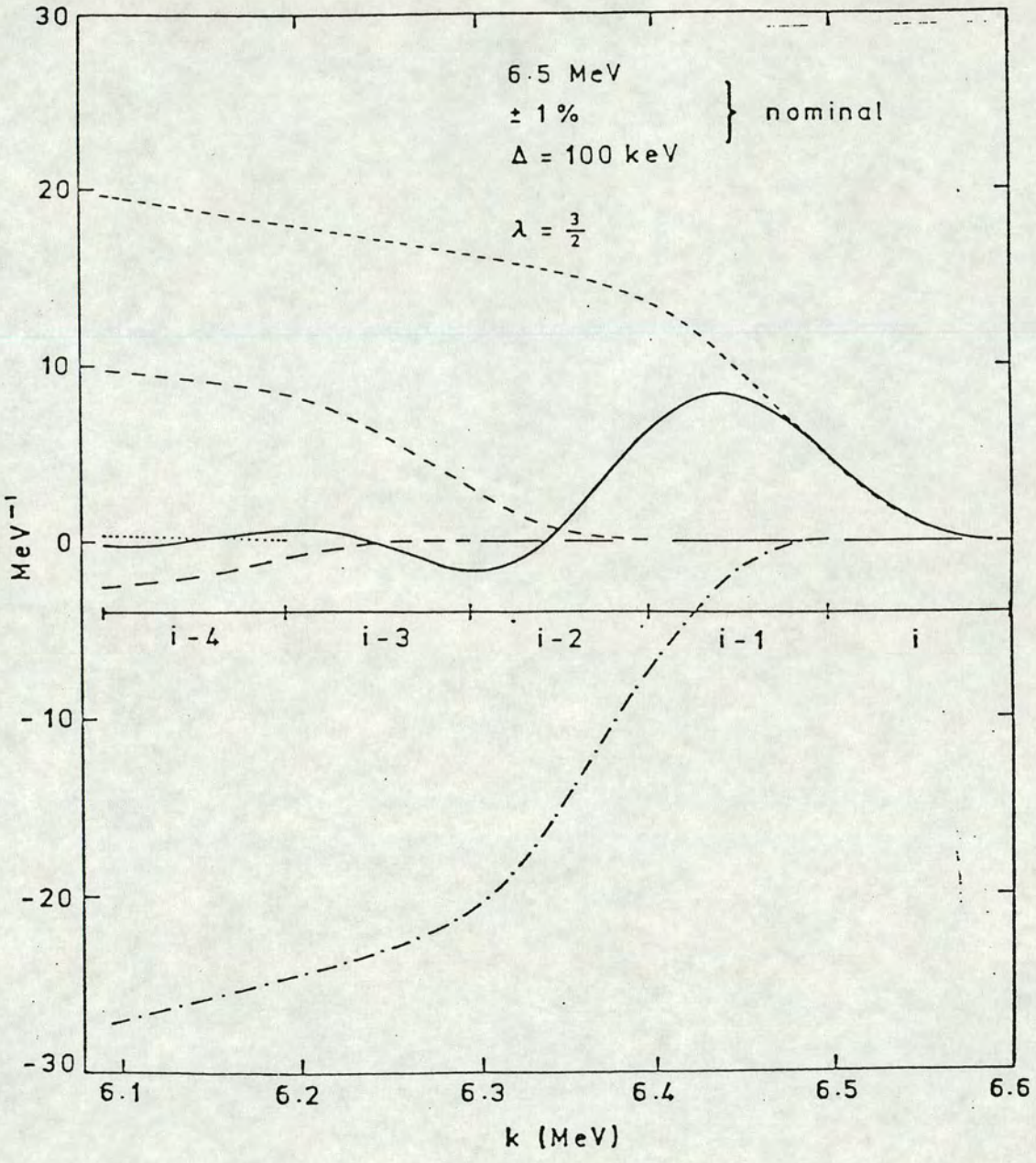

Figure 3.3: The bremsstrahlung weighting function with λ factor changed from 1/2 to 3/2.

3.5.3 Unfolding the Energy Pair Data

Taking Eq. 72 and writing out a few of the terms gives:

$$\sigma_1 = B_{11}Y_1 \tag{79}$$

$$\sigma_2 = B_{21}Y_1 + B_{22}Y_2 \tag{80}$$

$$\sigma_3 = B_{31}Y_1 + B_{32}Y_2 + B_{33}Y_3 \tag{81}$$

$$\vdots$$

$$\sigma_i = B_{i1}Y_1 + B_{i2}Y_2 + B_{i3}Y_3 + \cdots + B_{ii}Y_i \tag{82}$$

so that

$$\begin{aligned}\sigma_i = {} & B_{ii}(Y_i - Y_{i-1}) \\ & +(B_{i,i-1} + B_{ii})(Y_{i-1} - Y_{i-2}) \\ & +(B_{i,i-2} + B_{i,i-1} + B_{i,i})(Y_{i-2} - Y_{i-3})\end{aligned} \tag{83}$$

which implies that

$$\sigma_i = \sum_{j=1}^{i}(\sum_{m=j}^{i} B_{im})\Delta Y_j \tag{84}$$

where ΔY_j are the yield differences $Y_j - Y_{j-1}$. If one defines

$$A_{ij} = \sum_{m=j}^{i} B_{im} \tag{85}$$

then the leading term is $A_{ii}Y_i$ and the A_{ij} series converges rapidly as j is decreased.

3.5.4 Anomalies in Unfolding when Starting from Different Yield Points

In § 3.5.2 it was mentioned that the unfolding method assumed that the cross section was negligible for energies lower than the lowest energy point to be unfolded. If one unfolds yield data starting at the reaction threshold this assumption is reasonable. If however, one unfolds from say 3 MeV above threshold (at a change of energy bin widths, for instance) then this assumption is no longer so true. In fact, unfolding from this point results in

a slight overestimate of the first couple of cross section points. Therefore, a small correction needs to be made to these two points.

Assuming that the expression for a cross section point σ_i converges rapidly *i.e.* one need only consider the last three terms of the series (remembering that A_{ij} rapidly becomes 0 for decreasing j), then

$$\sigma_i = A_{ij}\Delta Y_j + A_{i(j-1)}\Delta Y_{j-1} + A_{i(j-2)}\Delta Y_{j-2} \tag{86}$$

But for the first unfolded point, the last two terms in Eq. 86 are normally assumed to be 0. Similarly, for the second unfolded point the last term is assumed to be 0. So, when unfolding starts at an energy below which the yields are *not* negligible, the first and second points must be multiplied by:

$$k_{corr1} = \frac{A_{ij}\Delta Y_j + A_{i(j-1)}\Delta Y_{j-1} + A_{i(j-2)}\Delta Y_{j-2}}{A_{ij}\Delta Y_j} \quad \text{for the first point} \tag{87}$$

$$k_{corr2} = \frac{A_{ij}\Delta Y_j + A_{i(j-1)}\Delta Y_{j-1} + A_{i(j-2)}\Delta Y_{j-2}}{A_{ij}\Delta Y_j + A_{i(j-1)}Y_{j-1}} \quad \text{for the second point} \tag{88}$$

To estimate the values of these corrections, one should calculate what these corrections would be for the third and fourth cross section points, using the values of the yield difference bremsstrahlung matrix A_{ij} and then use a linear extrapolation back to the first and second points.

In this calculation, the yield was assumed to be roughly constant over this small range so that $Y_i \simeq Y_{i-1}$. This correction is therefore an upper limit as the yield is actually rising with energy, but to do the calculation to any higher order simply complicates the argument for little gain in accuracy.

3.5.5 Interlacing Data Runs

To improve the statistics and hence reduce errors, it was found necessary to *interlace* the data.

Interlacing means adding the corrected yield differences from neighbouring energy runs, fitting as before, but then unfolding the yield differences which are now spaced by $2\Delta E$ as opposed to ΔE where ΔE is the energy step for the series of runs. The summations are then "offset" by one and the calculations repeated *i.e.* by first adding together corrected yield differences

from runs 1 and 2, 3 and 4, 5 and 6, *etc.* fitting and unfolding, then adding together corrected yield differences from runs 2 and 3, 4 and 5, 6 and 7, *etc.* fitting and unfolding to give two interlaced sets of results where the errors are reduced but the resolution halved. This particular procedure is known as *2-fold interlacing*. 3- or 4-fold interlacing can be performed by adding 3 or 4 neighbouring yield differences and offsetting the summations 2 or 3 times respectively for each fit and unfolding. Obviously, this will improve the errors still further but reduce the resolution. In this analysis it was thought necessary to do only 2-fold interlacing to bring down the errors whilst still preserving sufficient resolution to see any apparent structure in the cross sections.

3.5.6 Normalisation of Yields

The final yields need to be normalised to the same number of electrons incident on the bremsstrahlung radiator in order to obtain the final cross section as the bremsstrahlung spectra $N(E_j, k)$ used in the unfolding are for photons *per* MeV of photon energy *per* electron.

The number of incident electrons for a run is obtained from the P2 corrected charge from the equation

$$N_e = \frac{Q_{\text{corr.}}}{\int_0^E N(E,k)e^{-\mu_f(k)t_f}S(k)kdk} \tag{89}$$

where all the quantities are defined as before.

3.6 The Delayed Neutron Yield

3.6.1 A Description of Delayed Neutrons and their Importance

After fission, the fission fragments are unstable *i.e.* off the Z-N stability line and neutron rich as shown in Fig. 3.4. The fragments then β-decay towards the stability line. However, if the fragments are still unstable

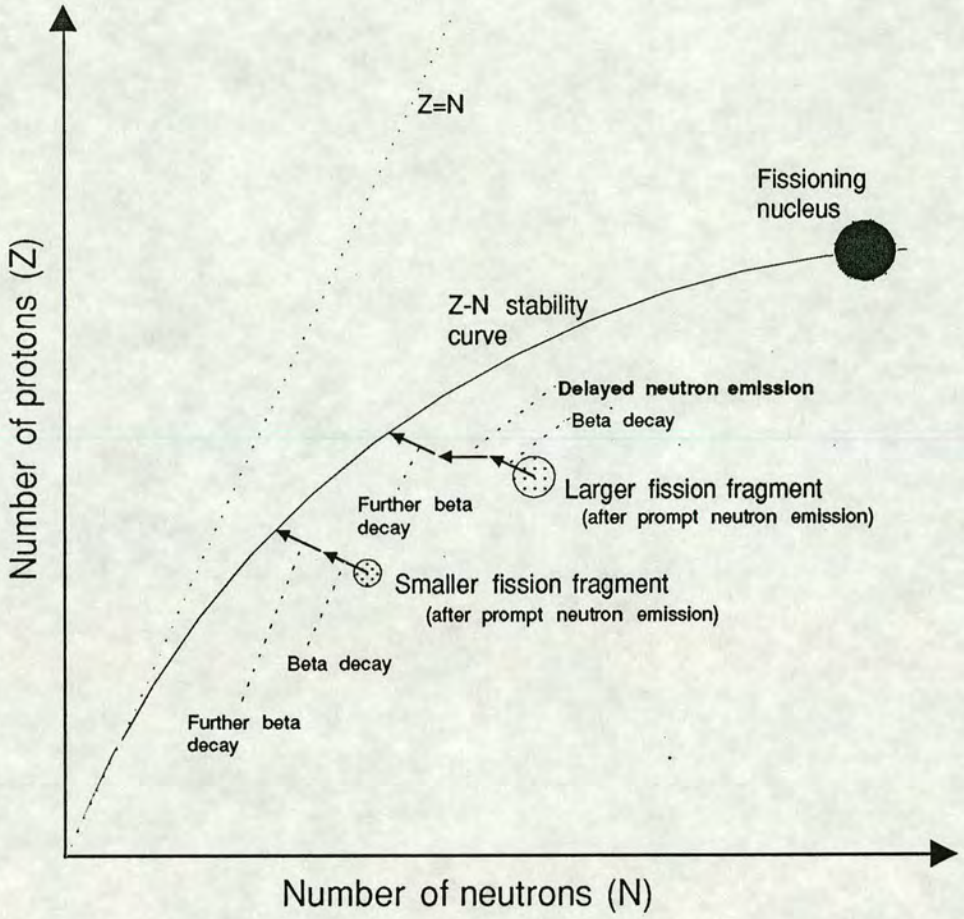

Figure 3.4: Fission fragment decay towards the *Z-N* stability curve (schematic representation).

and have sufficient excitation energy, they will occasionally emit neutrons known as *delayed neutrons*. These neutrons are important in the control of a chain reaction. In a normal reactor, the neutron flux is controlled so that the reactor core is marginally sub-critical for prompt fission neutrons. Delayed neutrons occur on a much longer timescale than prompt neutrons (*i.e.* $> 10^{-3}\,s$ as opposed to $< 10^{-14}\,s$ for prompt neutrons[3]), and if used to make the core critical, will offer a much better way of controlling the chain reaction within safe limits than using prompt neutrons alone. Hence a knowledge of the delayed neutron yield for actinides and how it agrees with theory is important, especially in helping to determine this parameter for

[3] *e.g.* the delayed neutrons from the fission fragment nuclide ^{87}Br have a half life of 54.5 s

fissile materials which might be used in future reactors.

3.6.2 Detection of the Delayed Neutrons

The delayed neutron yield was detected in much the same way as Dowdy *et al.* [Dowd 74]. The background gate is normally considered to record events unconnected with fission or photoneutron events. However, as delayed neutrons occur on a timescale much longer than fission neutrons, delayed neutrons will be detected in the background gate. Unfortunately, the delayed neutron yields for actinides are quite small (at most a few percent) and will constitute only a small perturbation to the (α, n) background neutrons recorded. Nonetheless, the high-rate runs (§ 3.4.8) show a noticeable effect.

Fig. 3.5 shows a plot of how the background event rate varies with increasing spectrum count rate. Note that the net spectrum rate has not been dead time corrected as this would be negligible. There is a large cluster of points near zero net spectrum count rate. These are the normal low-rate counts kept within limits so that the overlap correction is valid. These points are used to find the limiting background level in the absence (or near absence) of delayed neutrons. As the net spectrum count rate is increased, the background rate is seen to go up noticeably as the delayed neutron yield makes itself conspicuous above the (α, n) background. The slope of this line is used to find the delayed neutron yield.

3.6.3 Calculation of the Delayed Neutron Yield

All the high-rate runs were carried out well above the (γ, n) threshold. The low-rate runs suggested a fairly constant ratio of photoneutrons to fission neutrons and also a fairly constant value of $\overline{\nu}$ over this range. If the delayed neutron lifetimes are much greater than the time between beam bursts and there are on average N_f fissions/second and N_n photoneutrons/second at the beginning of each spectrum gate, giving $y_d N_f$ delayed neutrons/second (where y_d is the number of delayed neutrons/fission) over all time, then the

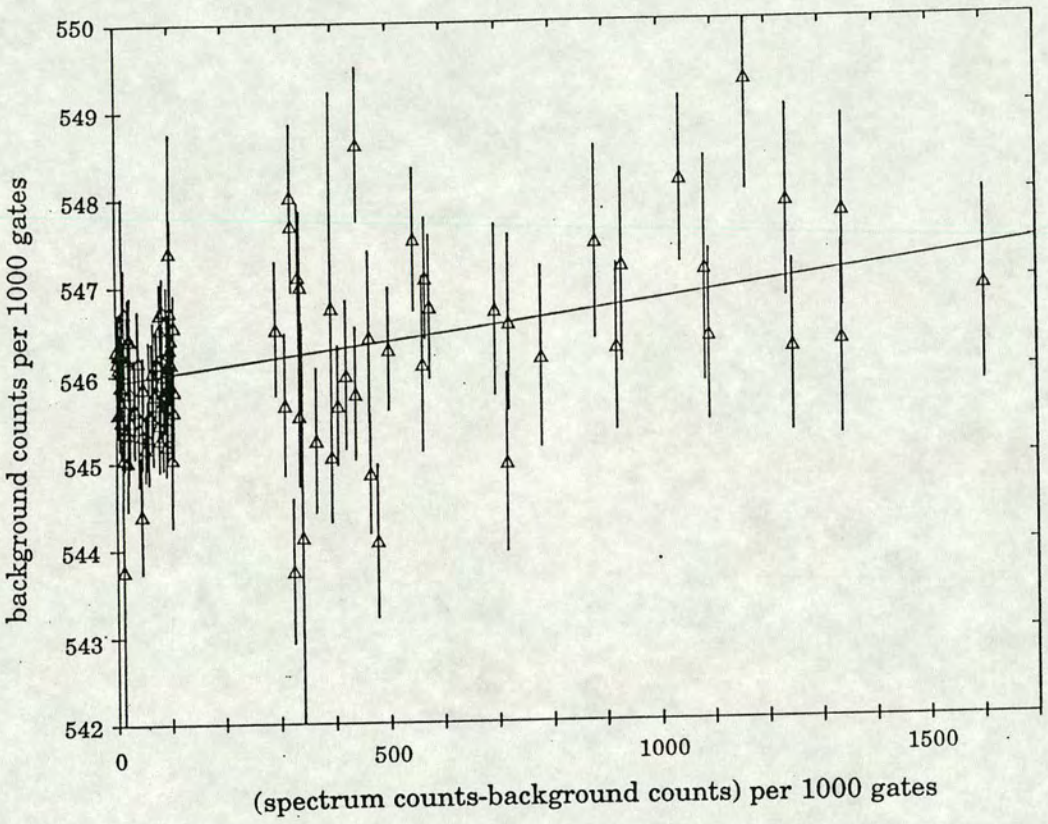

Figure 3.5: The change in the background count rate with increasing net spectrum count rate.

number of *detected* neutrons/gate in each spectrum gate S is given by

$$\begin{aligned} S &= g_s \varepsilon_{\gamma f} \overline{\nu} N_f T + \\ & g_s \varepsilon_{\gamma n} \frac{N_n}{N_f} N_f T + \\ & \varepsilon_d t y_d N_f + \\ & c \end{aligned} \tag{90}$$

where the first term is due to prompt fission neutrons, the second term is due to photoneutrons, the third term is due to delayed neutrons and the fourth term is due to the (α, n) and ambient background, T is the time between beam bursts and is 2000 μs in this case (see Fig. 2.13), t is the gate width, $\varepsilon_{\gamma f}$ is the ungated efficiency of detection of photofission neutrons, $\varepsilon_{\gamma n}$ is the ungated efficiency of detection of photoneutrons, ε_d is the efficiency of detection of delayed neutrons, $\overline{\nu}$ is the mean number of prompt neutrons per fission and g_s is the gating factor for the spectrum gate. A similar expression exists for the number of neutrons/gate detected in the background gate B

$$\begin{aligned} B &= g_b \varepsilon_{\gamma f} \overline{\nu} N_f T + \\ & g_b \varepsilon_{\gamma n} \frac{N_n}{N_f} N_f T + \\ & \varepsilon_d t y_d N_f + \\ & c \end{aligned} \tag{91}$$

where the four terms result in the same way as Eq. 90 and g_b is the gating factor for the background gate. Subtracting Eq. 91 from Eq. 90 gives the background subtracted spectrum gate rate

$$(S-B) = (g_s - g_b)\left(\varepsilon_{\gamma,f} \overline{\nu} N_f T + \varepsilon_{\gamma,n} \frac{N_n}{N_f} N_f T\right) \tag{92}$$

Combining Eq. 92 and Eq. 91 gives

$$B = \frac{1}{g_s - g_b}\left(g_b + \frac{\varepsilon_d t y_d}{(\varepsilon_{\gamma f}\overline{\nu} + \varepsilon_{\gamma n}\frac{N_n}{N_f})T}\right)(S-B) + c \tag{93}$$

If one makes a substitution such that

$$B = kS + c \tag{94}$$

then the quantity k is the slope of the line in Fig. 3.5 so that

$$k = \frac{1}{g_s - g_b}\left(g_b + \frac{t}{T}\frac{\varepsilon_d}{\varepsilon_{\gamma f}\overline{\nu} + \varepsilon_{\gamma n}\frac{N_n}{N_f}}y_d\right) \tag{95}$$

and the delayed neutron fraction is then

$$y_d = \frac{(g_s - g_b)k - g_b}{\frac{t}{T}\frac{N_f}{\overline{\nu}N_f + N_n}} \tag{96}$$

where it is assumed that

$$\varepsilon_{\gamma f} \approx \varepsilon_{\gamma n} \approx \varepsilon_d \tag{97}$$

as the efficiency response of the detector is a fairly flat function of energy over the region of interest and the dominant error is in the slope of k. Fig. 3.5 shows how the background subtracted spectrum rate (which is essentially $(S-B)$) varies with the background rate (which is essentially B). The numbers plotted are in terms of 1000's of gates.

Chapter 4

Results

4.1 A Summary

This chapter will present the best fit cross sections for the $\sigma_{\gamma f}$, $\sigma_{\gamma n}$ and $\overline{\nu}$ as well as a tentative figure for the delayed neutron yield from ^{241}Am. The cross sections are compared with few previous measurements in the literature noting any clear structure which might be seen. The cross section values and the values of $\overline{\nu}$ have, for convenience, been tabulated in Appendix A.

It has been mentioned before but will be reiterated that the quality of the data was not as good as might be desired, however in light of the fact that very little data has been taken for this isotope with the resolution of this experiment, these cross sections still represent at least a significant contribution to the available data for photonuclear reactions of ^{241}Am.

4.2 The Results for $\sigma_{\gamma f}$, $\sigma_{\gamma n}$, $\overline{\nu}$ and the Delayed Neutron Yield

4.2.1 $\sigma_{\gamma f}$

Fig. 4.1 shows a semi-log. plot of the photofission cross section of ^{241}Am over the energy range studied in this experiment for the first set of runs referred to henceforth as the '88 data. The data were taken at 100 keV steps and the

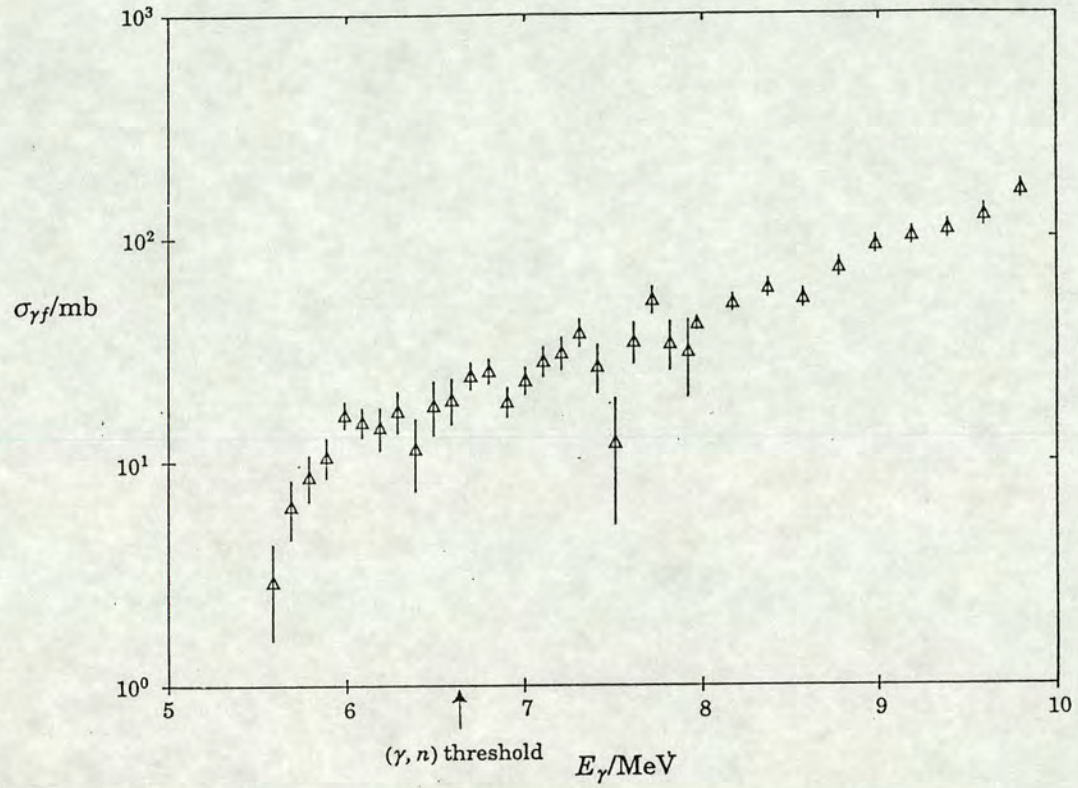

Figure 4.1: The photofission cross section from the '88 data.

interlaced, unfolded resolution is 220 keV throughout. The fit was carried out with both ν_p and W fixed as explained in § 3.4.7 to reduce the errors as much as possible. Note that systematic errors are not included such as the uncertainties in the energy calibration, the calibration of the P2 chamber and the value of $\overline{\nu}$ (see § 4.2.3), and these could amount to up to 5 %.

Fig. 4.2 shows the '88 data taken between 5.6 and 8.0 MeV at 100 keV steps with 220 keV interlaced and unfolded resolution. Fig. 4.3 shows the second set of runs (the '90 data) taken within the same range. Note that the cross sections were calculated using 2-fold interlacing.

The two sets of runs were analysed separately due to the different running efficiencies of each set. Furthermore, having two independent sets of data acts as a consistency check whereby if the same detail is seen in both sets of results one can have more confidence in this detail.

It will be noted that there are larger errors on the points after the opening of the (γ, n) threshold and up to about 8 MeV. This reflects the decrease in

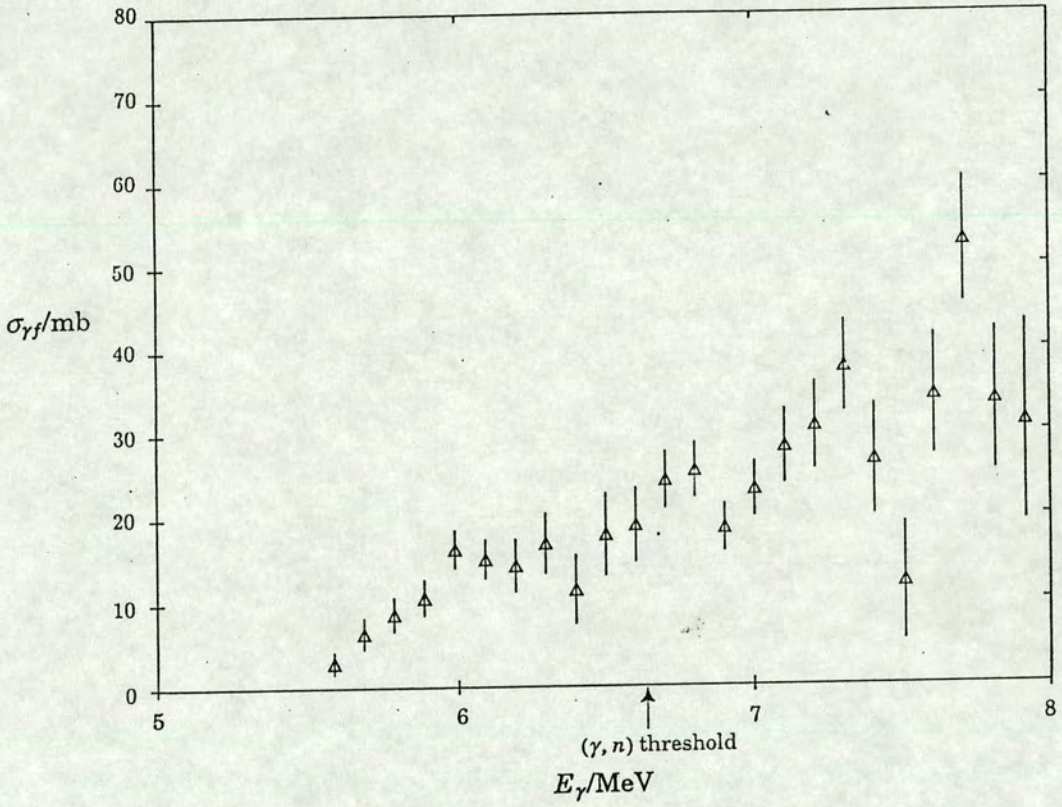

Figure 4.2: The photofission cross section between 5.6 and 8.0 MeV from the '88 data.

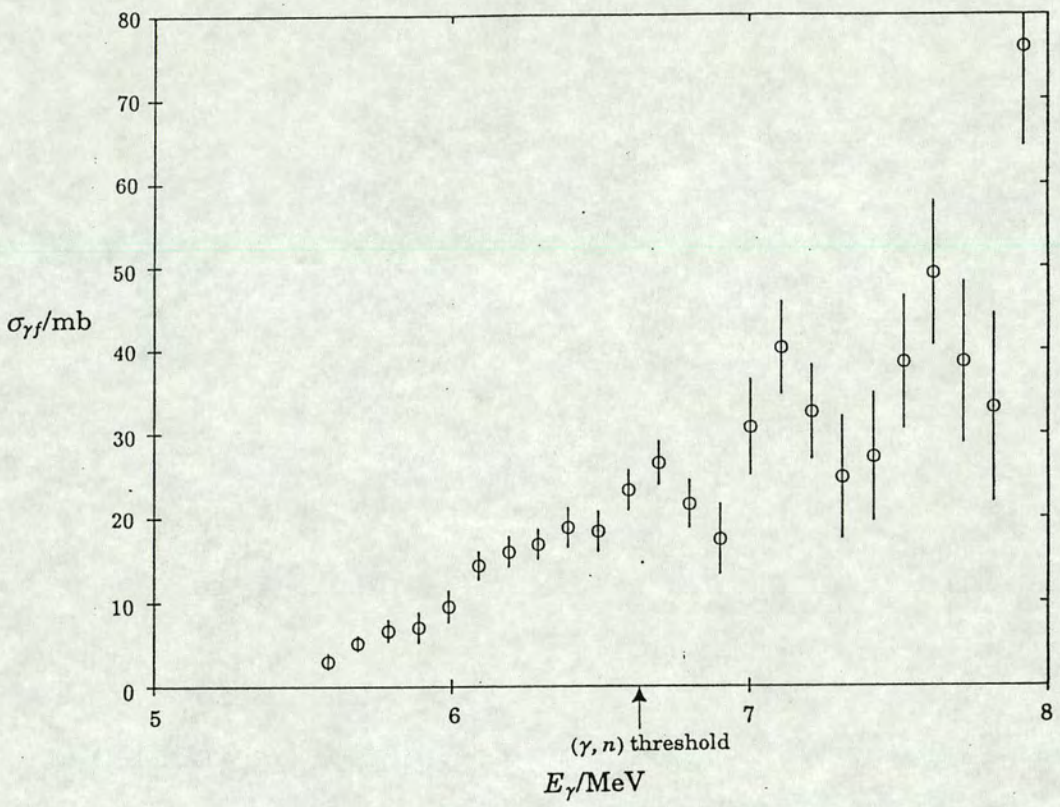

Figure 4.3: The photofission cross section between 5.6 and 8.0 MeV from the '90 data.

statistics from fitting only multiplicities 2 and above for the 100 keV steps data. The '88 data were taken at 200 keV intervals between 8.0 MeV and 10.0 MeV in order to find the yields in this range and at 500 keV intervals to carry out the fits. The data are quite smooth in this region which is partly reflected in the fact that the ratio of the (γ, f) to (γ, n) events were averaged from the fits to the 500 keV data. This average was used to find the cross sections resulting from the 200 keV data as explained in § 3.4.8. This is not an unreasonable approach because at these energies a large number of fission channels would be expected to be open thus smoothing out any irregularities in each individual channel. Furthermore, any barrier effects should be small as this energy range is well in excess of the barrier heights.

Though some form of a dip near the (γ, n) threshold at 6.63 MeV is seen in Fig. 4.2 and Fig. 4.3, the fact that the dips in the two data sets do not exactly coincide coupled with the fact that a further large unexplained dip occurs in both figures near 7.3 MeV suggests that this structure might be caused by the onset of instability in the unfolding procedure.

It has been shown from previous (γ, f) measurements (*e.g.* [Find 86, Find 87, Know 82]) that structure in the (γ, f) cross section is often observed near the fission threshold where the number of contributing fission channels is small. In order to help clarify this region, further data were taken at 50 keV steps between 5.7 and 6.5 MeV. Fig. 4.4 shows the 'raw' yield differences in counts/μC. The cross section obtained from the raw yield data shown in Fig. 4.4 produces a very wide spread of points from which it is difficult to conclude any shape to the cross section. The reason for this is that Fig. 4.4 uses no information about the shape of the multiplicity distribution but simply indicates the background subtracted neutron yield differences. Fitting the corrected data (even with both ν_p and W fixed) assumes a theoretical distribution which is not in fact a very good fit of the corrected yield difference multiplicity distribution due to the poor statistics and the effect of correcting for a large background in the difference distribution. Furthermore, fitting uses *event yield differences* as opposed to *neutron yield*

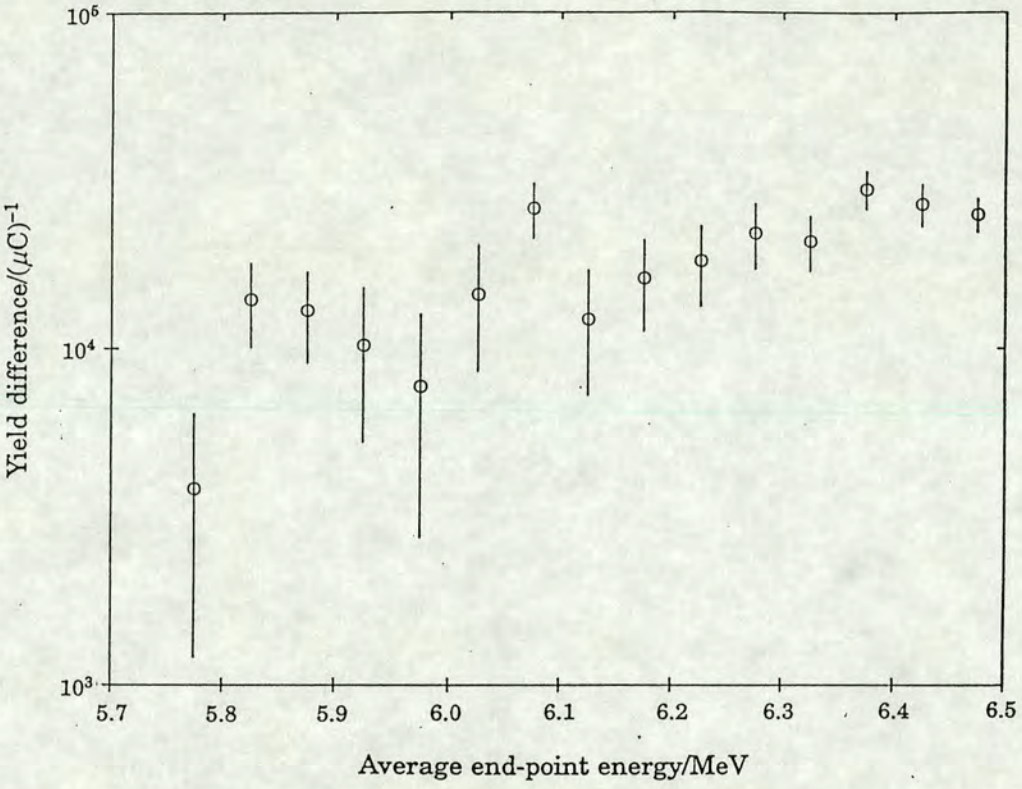

Figure 4.4: The raw yield differences from the 50 keV data.

differences the former having larger fractional errors. Unfolding the fitted event yields makes the problem worse as each point contains information about the previous points (see § 3.5.2) so any wild fluctuations in the fitted yields due to poor statistics is amplified in the unfolding procedure. Possible structure in the raw yield differences is seen in Fig. 4.4 between 6.0 and 6.1 MeV but the errors are too large to say there is definite evidence for a resonance at this point. By 2-fold interlacing the 50 keV data the wide spread of points is reduced at the expense of the resolution. The 2-fold interlaced 50 keV data (see Fig. 4.5) may show evidence for a peak at ~6.0 MeV but statistically this is not significant.

Fig. 4.6 shows the '88 data compared with measurements carried out by Zhuchko *et al.* [Zhuc 78]. Similarly, Fig. 4.7 shows the '90 data compared with measurements of Zhuchko. It can be seen that there is good agreement in both cases, though Zhuchko's data has insufficient resolution to show any real structure. Zhuchko's data are the only other comparable photofission

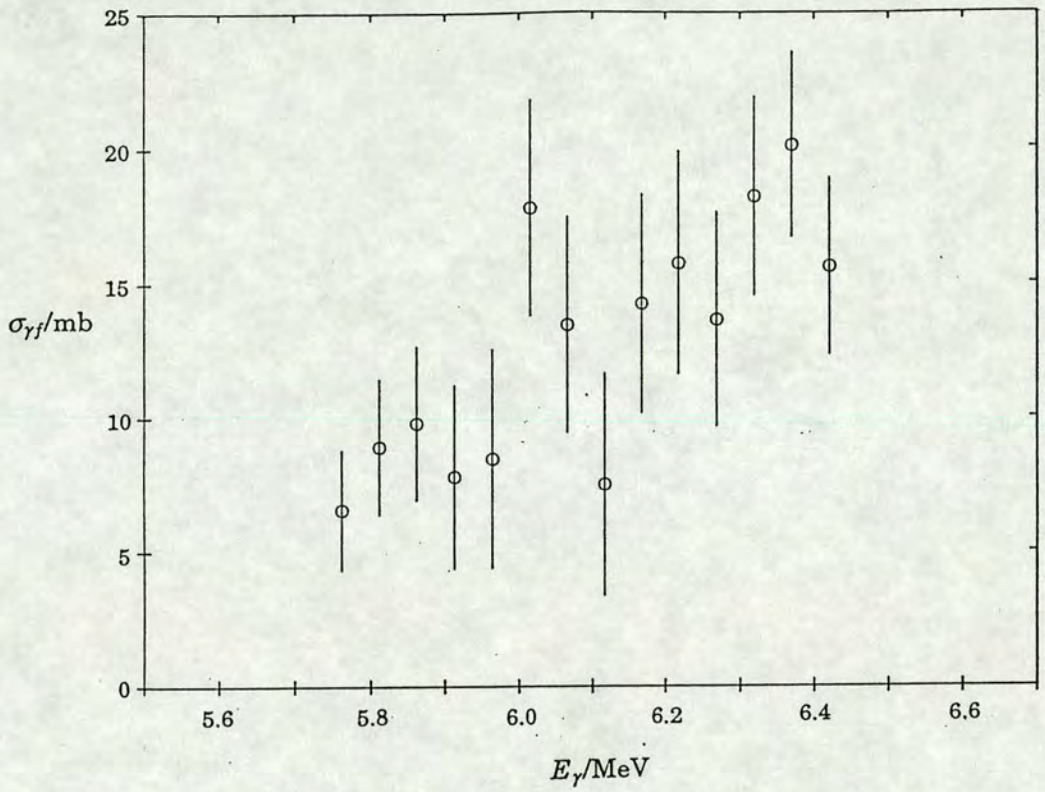

Figure 4.5: The photofission cross section from the 50 keV data.

measurements carried out on ^{241}Am in this region. However, charged particle induced fission of ^{241}Am has been studied by Back *et al.* [Back 74b]. Though charged particle induced fission excites far more reaction entrance channels and hence fission channels than in the case of photofission, (see Fig. 1.6) the two sets of results can nonetheless be compared by plotting the *fissility i.e.* the fission cross section divided by the total reaction cross section. As the total absorption cross section is not known over the range from the fission threshold to the neutron emission threshold, this cross section is approximated by the giant dipole resonance in the form of a double Lorentzian curve [Zhuc 78].(The use of two Lorentzians reflects the splitting of the GDR due to the non-spherical shape of the actinide nuclei). Note again Fig. 1.5.

The shape of the dipole photon absorption cross section across the actinides is known to change only very slowly, hence a fit can be made to the double Lorentzian for all available actinide data and used for the case

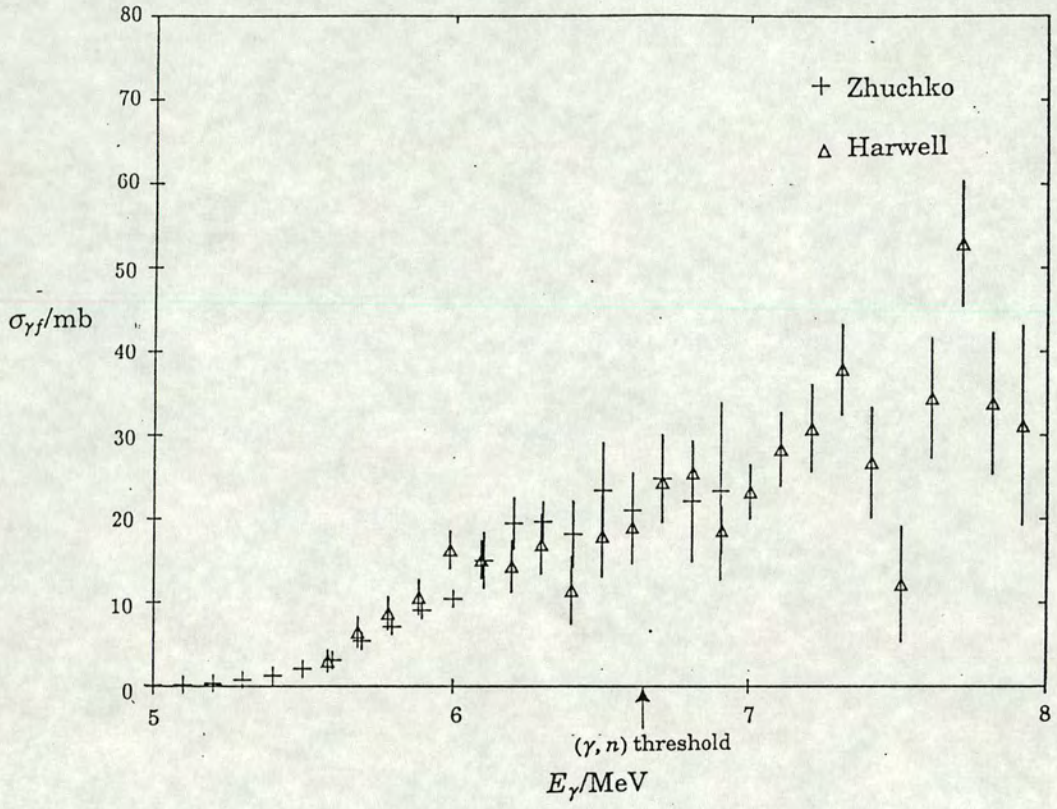

Figure 4.6: The photofission cross section from the '88 data compared with Zhuchko *et al.*

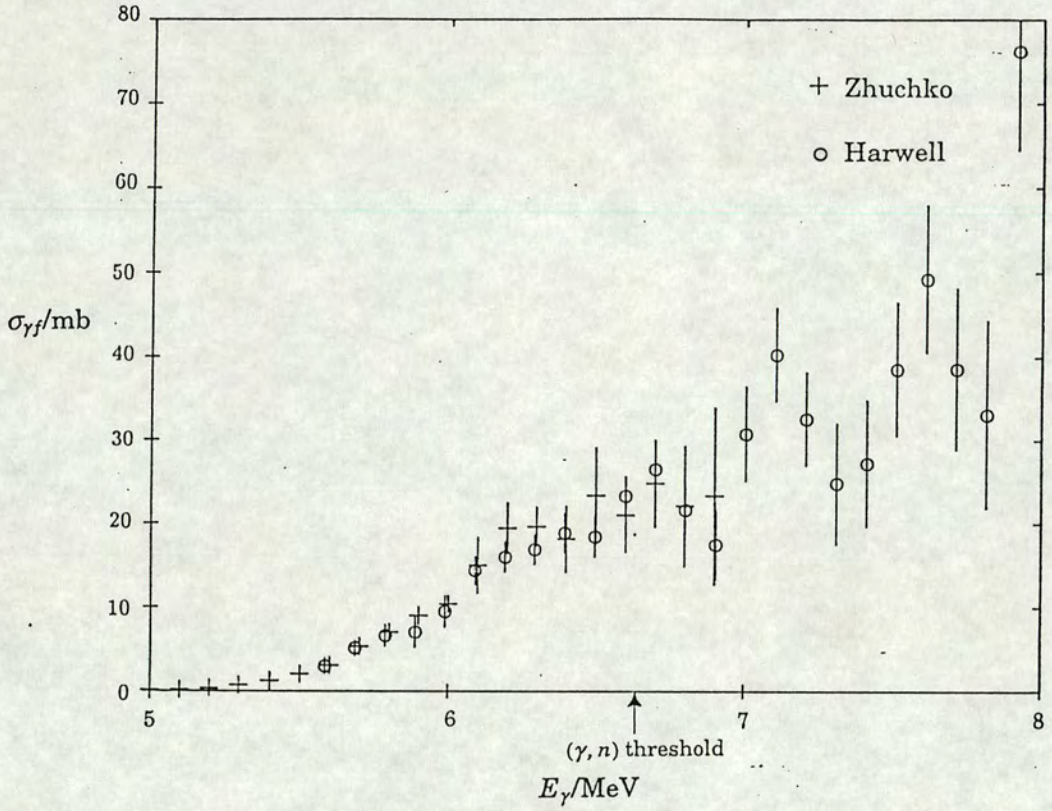

Figure 4.7: The photofission cross section from the '90 data compared with Zhuchko *et al.*

of ^{241}Am(see again [Zhuc 78]). The best fit between 6--10 MeV gives

$$\sigma_{\gamma a_1}(E_\gamma) = \sum_{i=1,2} \sigma_i \frac{(\Gamma_i E_\gamma)^2}{(E_\gamma^2 - E_i^2) + (\Gamma_i E_\gamma)^2)} \tag{98}$$

with the parameters $\sigma_1 = 250$ mb, $E_1 = 10.5$ MeV, $\Gamma_1 = 2.5$ MeV, $\sigma_2 = 300$ mb, $E_2 = 14$ MeV and $\Gamma_2 = 4.5$ MeV. The fissility is then

$$P_f = \frac{\sigma_{\gamma f}}{\sigma_{\gamma a_1}} \tag{99}$$

assuming predominantly dipole absorption. Fig. 4.8 shows the fissilities of the '88 data compared with Zhuchko and Back. Back's data was obtained from the reaction ^{240}Pu(^{3}He,df)^{241}Am where a large number of decay channels is involved above the fission threshold due to the varied angular momenta brought in by the incident ^{3}He ions giving the overall fissility as a function of energy E

$$P_f(E) = \sum_{J,\pi} \alpha(EJ\pi) P_f(EJ\pi) \tag{100}$$

where $P_f(EJ\pi)$ is the fissility of an individual fission channel with angular momentum J and parity π at energy E and $\alpha(EJ\pi)$ is the normalised probability of exciting a compound state $EJ\pi$ (see § 5.2.2). In the case of photon induced fission on an odd-A isotope such as ^{241}Am though the absorption is predominantly E1, one can still excite a broad set of fission channels because of the non-zero ground state spin. One would expect, therefore, to excite a similar broad spectrum of channels in photofission to those in particle induced fission. This explains the reasonably good agreement of the fissilities of the photofission data and the charged particle induced fission data, though obviously any resonant structure is still more likely to be seen in the photofission data.

4.2.2 $\sigma_{\gamma n}$

Fig. 4.9 shows the (γ, n) cross section for both the '88 and '90 data. The large spread of points from threshold to 8.0 MeV reflects the difficulty in extracting a cross section from data with a large background and a small

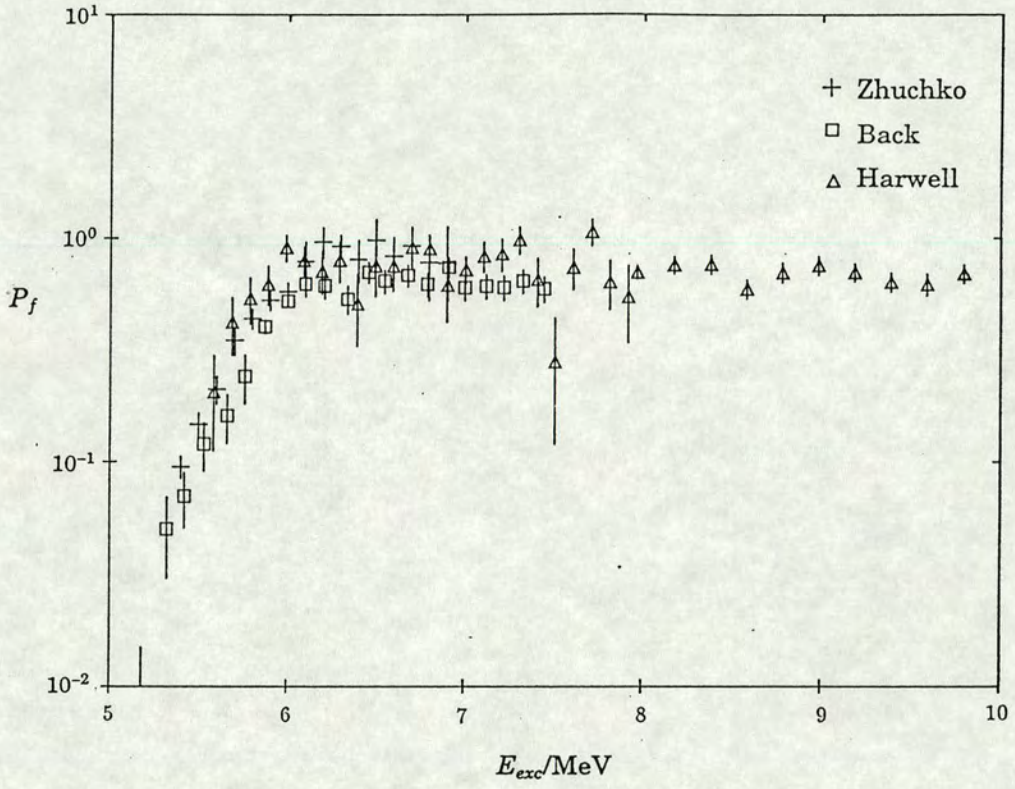

Figure 4.8: The fissility from the '88 data compared with that of Zhuchko *et al.* and Back *et al.*

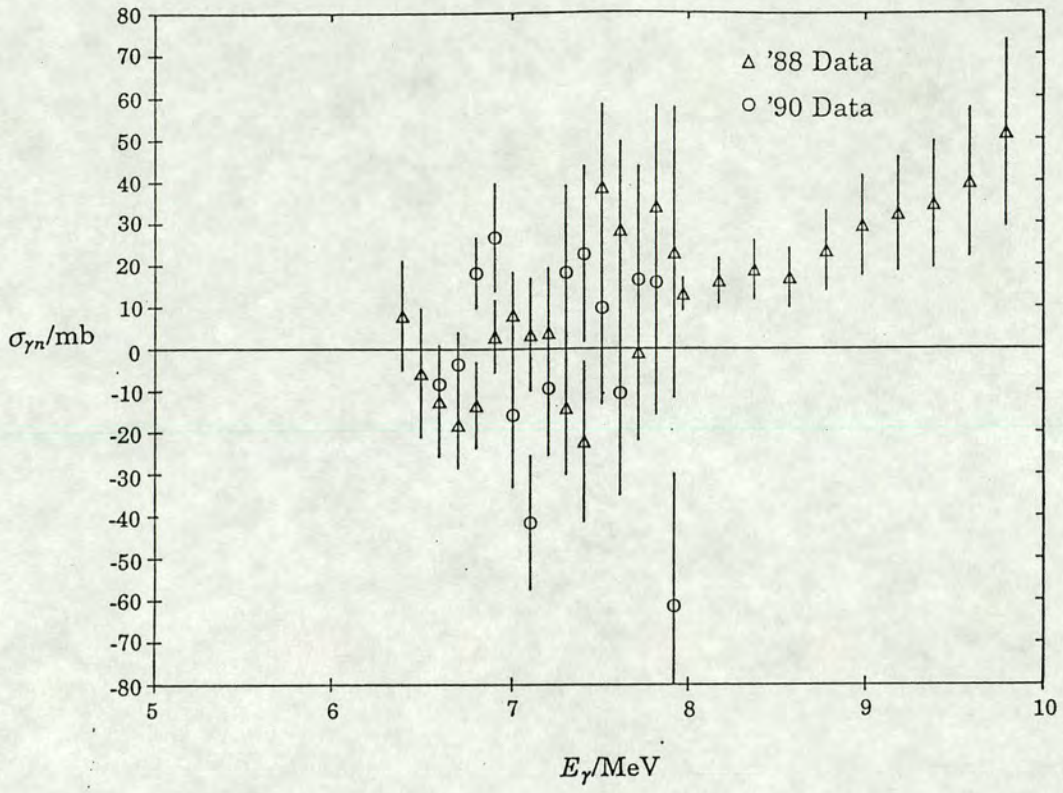

Figure 4.9: The photoneutron cross section obtained from the '88 and '90 data.

neutron emission width compared to fission width when using the TRDG. One can only say that these data points are not inconsistent with a (γ, n) threshold at 6.63 MeV [Elli 85].

The points above 8.0 MeV were calculated by using an average of the fits to the 500 keV data to give the ratio of (γ, n) to (γ, f) events over the range 8.0--10.0 MeV and should give a reliable estimate of the magnitude of the cross section over this range.

There are no other (γ, n) data with which to compare the present results.

4.2.3 $\overline{\nu}$

Fig. 4.10 shows a plot of the average number of prompt neutrons per fission against mean photon energy. As the data were fitted with the TRDG first, these points have not been unfolded but instead have been plotted as a

function of *mean* photon energy given by the expression

$$\bar{k} = \frac{\int_0^{E_e} N(E_e, k)\sigma_{\gamma f}(k)kdk}{\int_0^{E_e} N(E_e, k)\sigma_{\gamma f}(k)dk} \tag{101}$$

where all the quantities are defined as before. Note that the data is not interlaced.

The data show a small decrease in $\bar{\nu}$ with increasing energy for the 100 and 50 keV data between 5.5 and 6.8 MeV and an increase for the 500 keV data points between 7.0 and 8.0 MeV. There also appears to be a sudden jump at about 5.7 MeV which might be a problem with the analysis. The data were obtained by fixing W to a straight line fit to reduce errors. It is worth sounding a note of caution in reading too much into these data points. It was found that fitting the 50 keV data allowing both ν_p and W to vary freely resulted in unrealistically increasing values of $\bar{\nu}$ with decreasing energy. Once W is fixed to values obtained from the 100 keV data this goes away but makes one suspicious about believing the trend when fitting to data with poor statistics near threshold and a large background. Furthermore, the 500 keV points which are data taken over a broader range show a slight increase with increasing energy which is more as one would expect. Despite this however, the change over 5.7--8.0 MeV is comparatively small (the cross section data calculated were fitted with ν_p and W in this range) and any uncertainties in $\bar{\nu}$ make only a small (at most ~5%) uncertainty in the evaluated cross section. This coupled with the fact that the Zhuchko and Harwell data agree quite well leads one to believe that at least the magnitude if not the trend of $\bar{\nu}$ is correct, and therefore can be taken to be 3.05 ± 0.15 over the range of interest (neglecting the points below the jump at 5.7 MeV).

Again there are no other data with which the present results can be compared directly. However, $\bar{\nu}$ data for photofission of other actinides [Berm 86] show a trend of increasing $\bar{\nu}$ with energy ($d\bar{\nu}/dE \approx 1/7$ for neutron induced fission). Measurements on ^{232}Th and ^{238}U [Find 86, Find 87, Cald 80] have also shown increasing $\bar{\nu}$ with decreasing energy near fission threshold. Measurements by neutron induced fission of ^{233}U, ^{235}U [Bold 76] and ^{232}Th

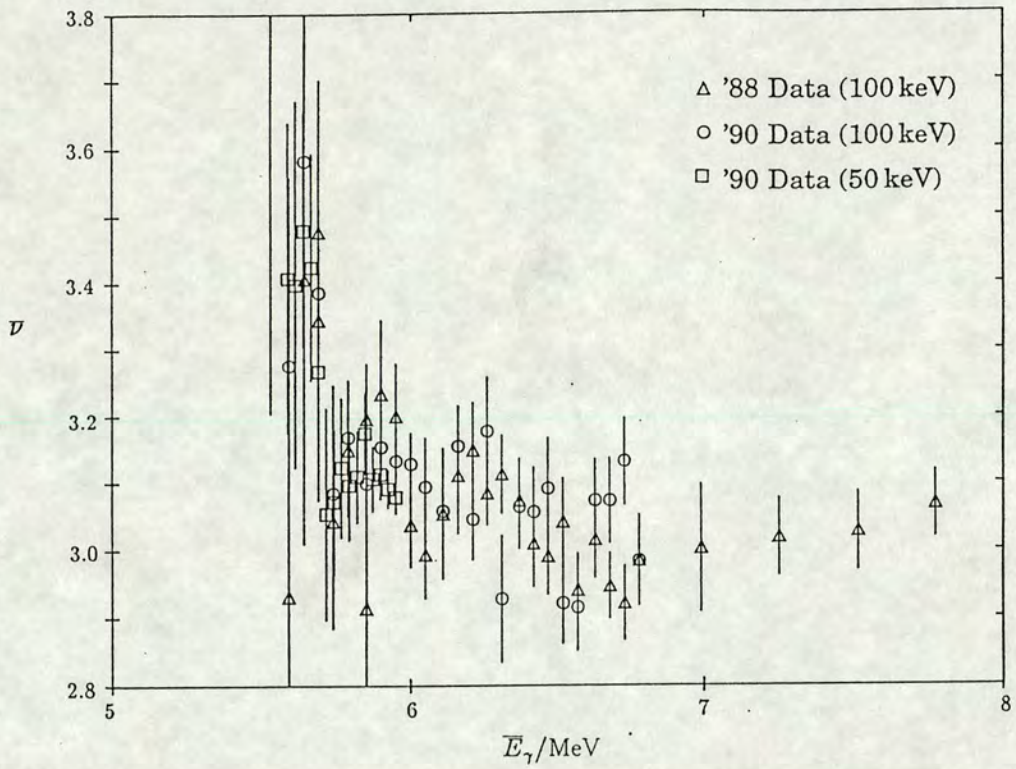

Figure 4.10: $\overline{\nu}$ obtained from the '88 and '90 data.

[Caru 77] also show an increase in $\overline{\nu}$ with decreasing energy near the fission threshold. These results suggest that further investigation in this region should be carried out.

4.2.4 The Delayed Neutron Yield

The evaluation described in § 3.6.3 gave a value for the delayed neutron yield of 0.43 ± 0.72 % per fission. This value, when plotted with similar data for other actinides [Wald 81] agrees with the general trend though the error is very large. This large error reflects the fact that the dominant contribution to the slope in Fig. 3.5 is the ratio of the background and spectrum gating factors (g_b/g_s)as can be seen from Eq. 95. The dotted line in Fig. 4.11 shows a least squares fit to the data assuming an exponential dependence on neutron excess *i.e.*

$$y_d(\text{per 100 fissions}) = \exp(16.698 - 1.144Z_c + 0.377A_c) \qquad (102)$$

where Z_c and A_c are the composite charge and mass of the fissioning nucleus so for example, neutron induced fission on the nucleus ${}^{A}_{Z}\mathrm{X}$ results in the composite fissioning nucleus ${}^{A+1}_{Z}\mathrm{X}$.

The error on the present result is quite large as the experiment was not designed to measure this value and was only possible due to the high-rate runs. Obviously, to reduce this error one would have to run at much higher yield rates to extend the plot shown in Fig. 3.5 in order to see the value of y_d more clearly above the factor of g_b/g_s. Reducing the ratio of the gating factors by having the background gate further away in time from the spectrum gate would be the best way to reduce g_b/g_s and make the delayed neutron yield stand out more clearly.

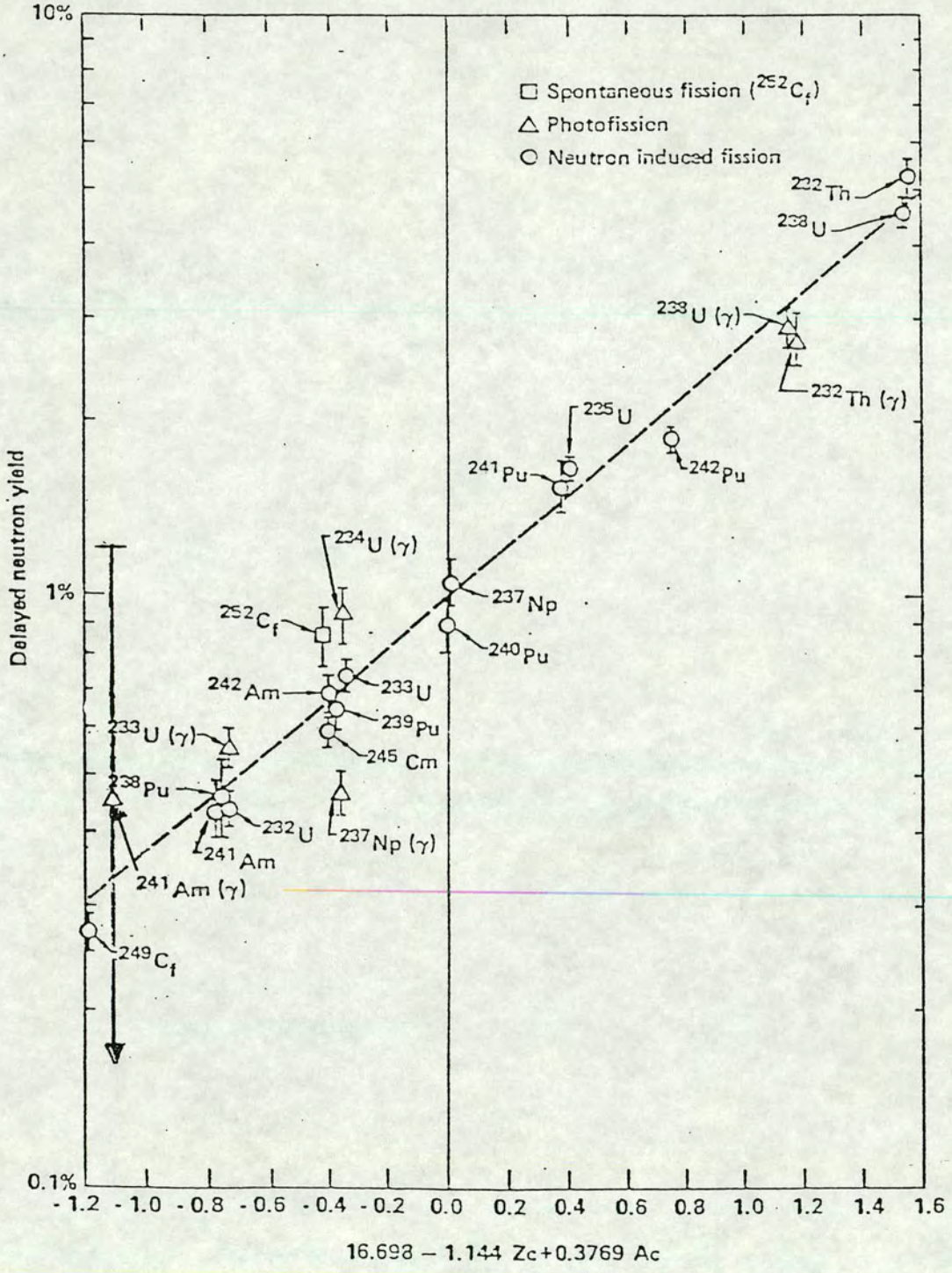

Figure 4.11: Comparison of the delayed neutron yield of ^{241}Am with other actinides.

Chapter 5

Theory

5.1 Introduction

Ever since the discovery of fission, people have tried to relate the shape of the fission barrier to the shape of the fission cross section. This chapter describes an attempt to try and fit a fission cross section to the three actinides studied at Harwell, *i.e.* ^{232}Th, ^{238}U and ^{241}Am. Fits are made using contemporary theory with the best experimentally deduced parameters for these isotopes. The resulting theoretical cross sections are compared with experiment and an attempt is made to explain any failings within the framework of the theory used.

5.2 The Fission Process

5.2.1 Decay of an Excited Actinide Nucleus

When an actinide nucleus is excited in a photonuclear process, it can decay in a number of ways. Fig. 5.1 shows a schematic diagram of the competing processes within the framework of the double-humped fission barrier hypothesis.

The nucleus is initially excited into some continuum state in the first well of the fission barrier. From there it can either γ-decay to a lower state

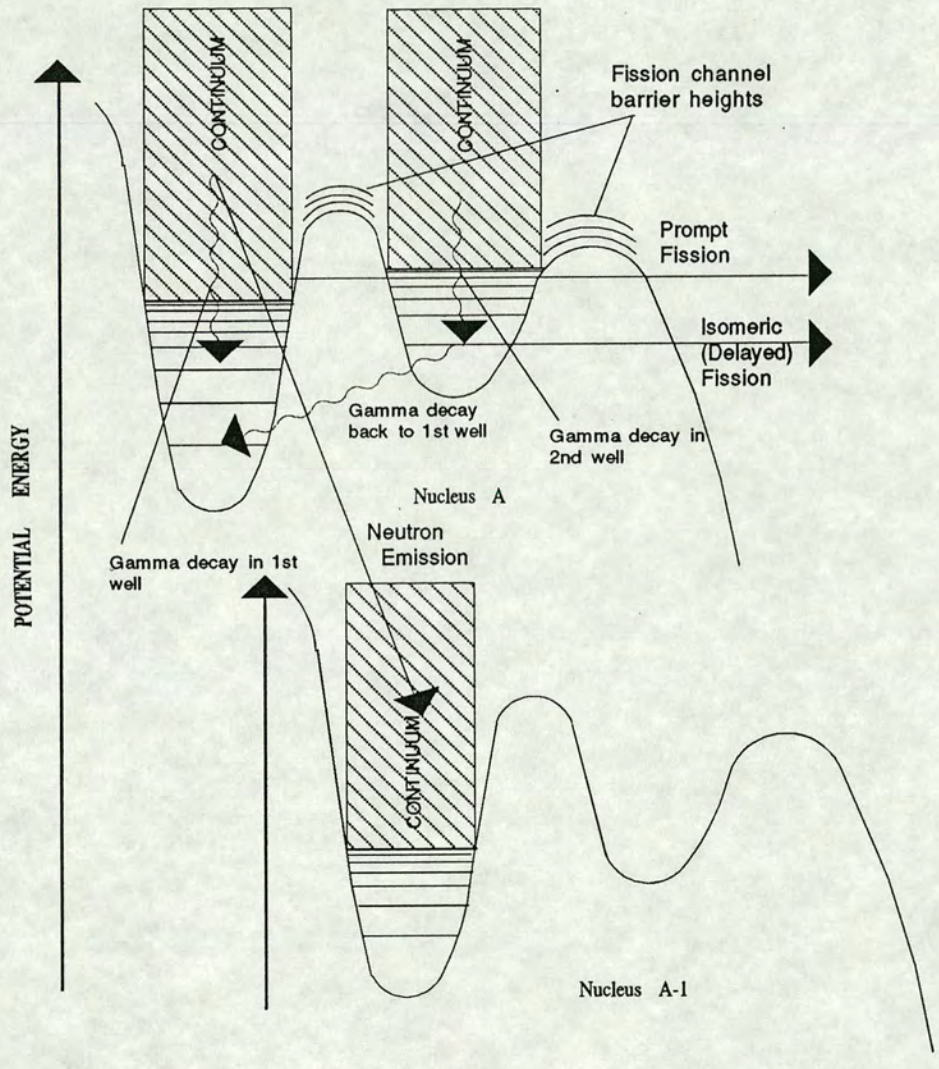

Figure 5.1: Competing processes in the decay of an excited actinide nucleus.

in the first well, emit a neutron to decay to an $A-1$ nucleus, fission directly by "tunnelling" through both humps of the fission barrier (in the form of a fission "wave" quantum-mechanically tunnelling through a barrier) or tunnel through the first hump into the second minimum of the fission barrier. In the final case, further decay can occur by γ-decay to a lower state in the second well, decay back to the first well by tunnelling through the first barrier or isomer fission following γ-decay in the second well by tunnelling through the second barrier.

The barrier height "seen" by the fission wave depends on the fission channel (represented by a series of peaks at the saddle points as shown in Fig. 5.1). The photofission cross section is given by the equation:

$$\sigma_{\gamma f} = \sum_{J\pi} \left[\alpha(EJ\pi) \frac{\sigma_{\gamma a_l} \sum_{\nu} T_f^{\nu}(EJ\pi)}{\sum_{\nu} T_f^{\nu}(EJ\pi) + \sum_{\mu} T_{\gamma}^{\mu}(EJ\pi) + \sum_{\xi} T_n^{\xi}(EJ\pi)} \right] \tag{103}$$

where $\alpha(EJ\pi)$ is the normalised probability for populating states with angular momentum J and parity π in the target nucleus, $\sigma_{\gamma a_l}$ is the photon absorption cross section corresponding to the multipole order l of radiation absorbed, T_f^{ν}, T_{γ}^{μ}, T_n^{ξ} are the fission, γ and neutron transmission coefficients respectively and ν, μ, ξ are summed over all available fission, γ emission and neutron emission channels for the populated state $EJ\pi$ in the target nucleus. These will be discussed in the following sections. Eq. 103 neglects any double-weighting of channels with $K \neq 0$.

5.2.2 The Compound Nucleus

Niels Bohr first proposed the compound nucleus theory, the development of which is described in a review article by Rüdinger and Peierls [Rudi 86]. He suggested that when a nucleus is excited by a particle or photon, the energy it receives can be shared by the entire nucleus, so it retains no memory of how it was formed. The only parameters which determine the nucleus's future are the imparted energy and angular momentum. The excited nucleus can then decay through a series of reaction channels,

including fission channels. As stated in the opening chapter, Niels Bohr's son, Aage Bohr proposed the channel theory of fission [Bohr 56], namely that fission occurs via a small number of states similar to those near the ground state of the nucleus, whereby most of the excitation energy is taken up in deformation leaving the nucleus thermodynamically cold. It is with this in mind that the even-even actinide isotopes have been studied in great detail by many groups.

The normalised probability $\alpha(EJ\pi)$ for populating states with spin J and parity π is given by the general normalised density of states factor:

$$\alpha(EJ\pi) = \frac{\frac{1}{2}(2J+1)\exp[-(J+\frac{1}{2})^2/2\sigma_A^2]}{\sum_{J\pi}\frac{1}{2}(2J+1)\exp[-(J+\frac{1}{2})^2/2\sigma_A^2]} \tag{104}$$

where σ_A is the spin cut-off factor for a nucleus of mass A and the summation is taken over all allowable excitations. In this analysis, only E1 and E2 excitations are considered (higher order excitations are too small in magnitude to contribute to the cross section significantly).

5.2.3 Low-Lying Even-Even Nuclei Fission Channels

Two of the most widely studied actinides, ^{232}Th and ^{238}U, (which both occur naturally) are even-even isotopes *i.e.* the protons and neutrons in these nuclei are all paired. This implies that the lowest lying excitations are collective and few in number until sufficient energy is imparted to the nucleus to break a pair to give rise to a continuum of particle excitations. The collective excitations are labelled by the *quantum* number "K". This is thought to be a good quantum number between saddle and scission. K is the projection of the angular momentum of the nucleus J on the fission axis (Fig. 5.2). Onto each collective excitation is built a rotational band to give the spectrum of levels shown schematically in Fig. 5.3. The quantities Y_l^m are Legendre polynomials in terms of which the nuclear shape is described. The energies of the rotational states are given by:

$$E_{rot}(J,K) = (\hbar^2/2\mathcal{I})[J(J+1) - K(K+1)] \tag{105}$$

where $\mathcal{I}$ is the moment of inertia of the nucleus.

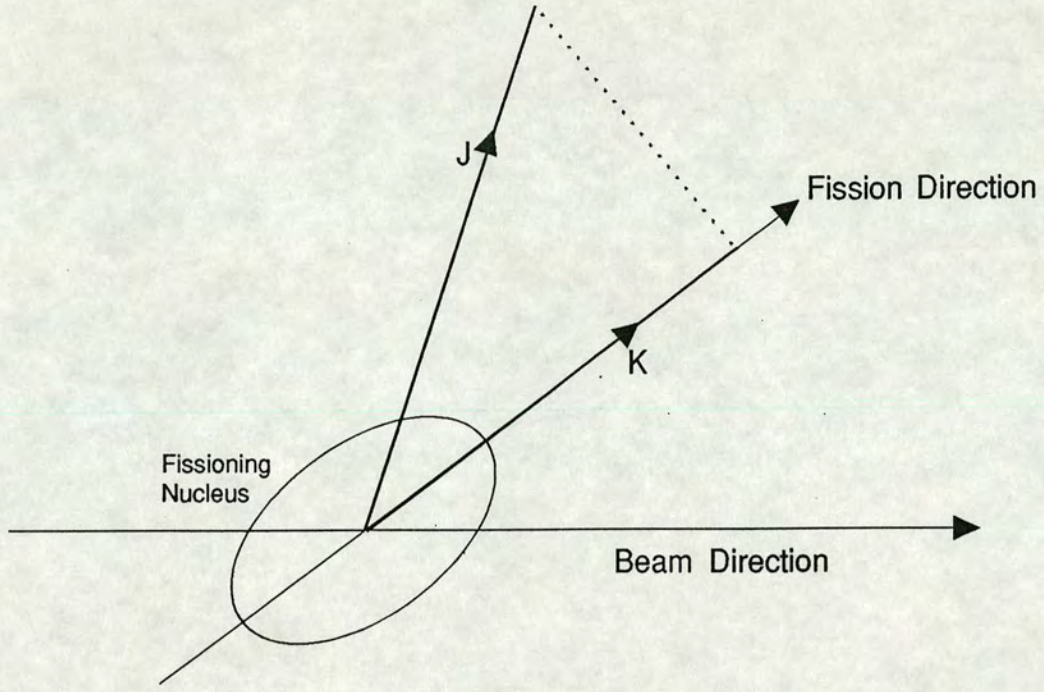

Figure 5.2: K: The projection of J onto the fission axis.

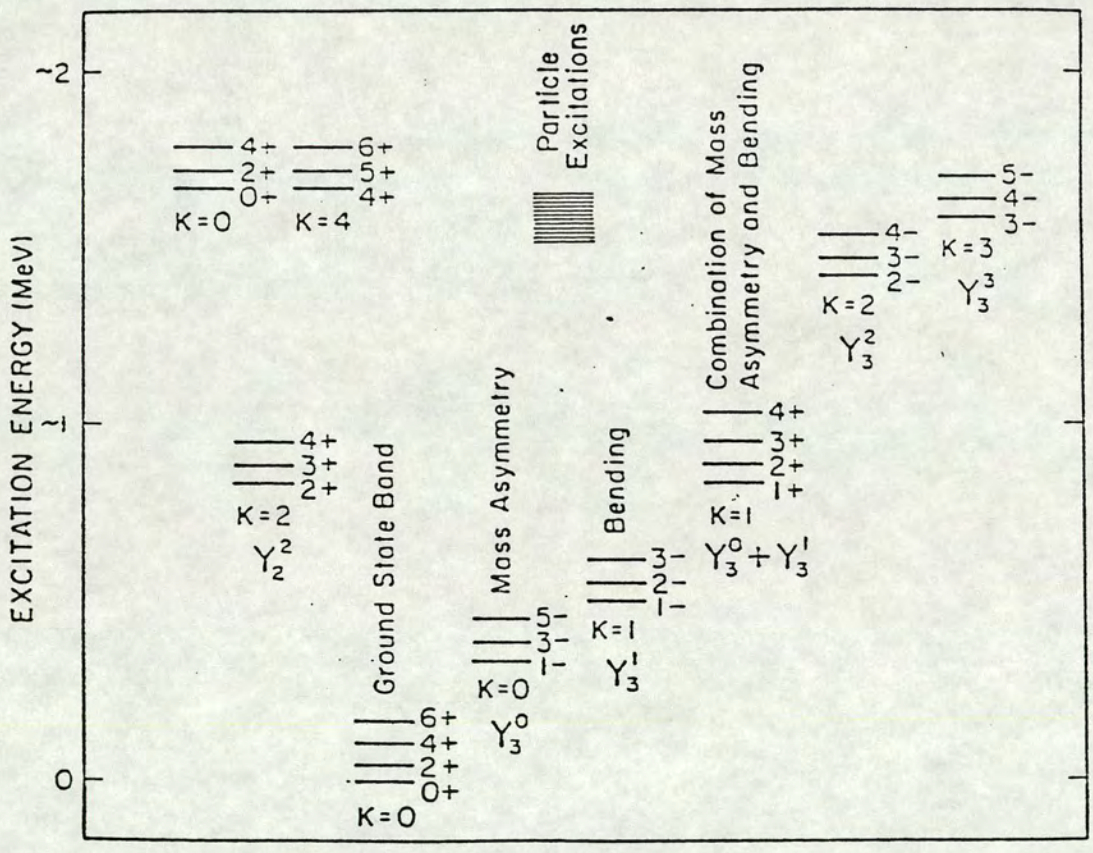

Figure 5.3: The spectrum of fission channels for an even-even nucleus.

Photon excitation excites predominantly dipole (E1) with some quadrupole (E2) moments in the nucleus. These moments are assumed to be in the fixed ratio of 0.98 : 0.02 over the range of interest though the ratio could be as high as 0.96 : 0.04 from studies involving the angular distribution of fission fragments [Zhuc 78]. This restricts the number of channels through which fission can occur and is a positive advantage in studying the fission process. An even-even nucleus has a $J = 0^+$ ground state, implying that only $J = 1^-$ and $J = 2^+$ states will be excited in photonuclear reactions. Fig. 5.3 shows these states for the K bands below the particle excitation threshold.

As explained in Chapter 1, the barrier to fission is thought to be double- or possibly triple-humped. For each saddle-point state shown in Fig. 5.3 there is a fission barrier shifted upwards in height by its excitation energy. In fact, the position of the levels shifts from the inner saddle-point to the outer, due to the increasing deformation of the nucleus. Figs. 5.4 and 5.5 show Nilsson diagrams indicating the shift in energy of proton and neutron levels as the nuclear potential is deformed [Gust 67] by the deformation parameter δ_{OSC}. Table 5.1 shows the upward displacements of the low-lying fission channel barrier heights approximated for an even-even nucleus (taken from [Ohsa 84]). The first barrier A is assumed to be axially asymmetric but reflection symmetric (γ-deformed) and the second barrier B is assumed to be axially symmetric but reflection asymmetric (octupole-deformed). The rotational levels built onto these so-called *band-head states* are assumed, for simplicity, to be degenerate in energy as for actinides, the value of $\hbar^2/2I$ in Equation 105 is a few 10's of keV at the most.

5.2.4 Low-Lying Odd-Even Nuclei Fission Channels

In the case of odd-even nuclei such as ^{241}Am, the situation is complicated by the existence of an unpaired proton. The spectrum of states at the saddle points have been approximated to quasi-particle states by Back *et al.* [Back 74b]. Using a Strutinsky-type calculation such as that by Larsson *et al.* [Lars 74] to find the single particle states, the quasi-particle energy

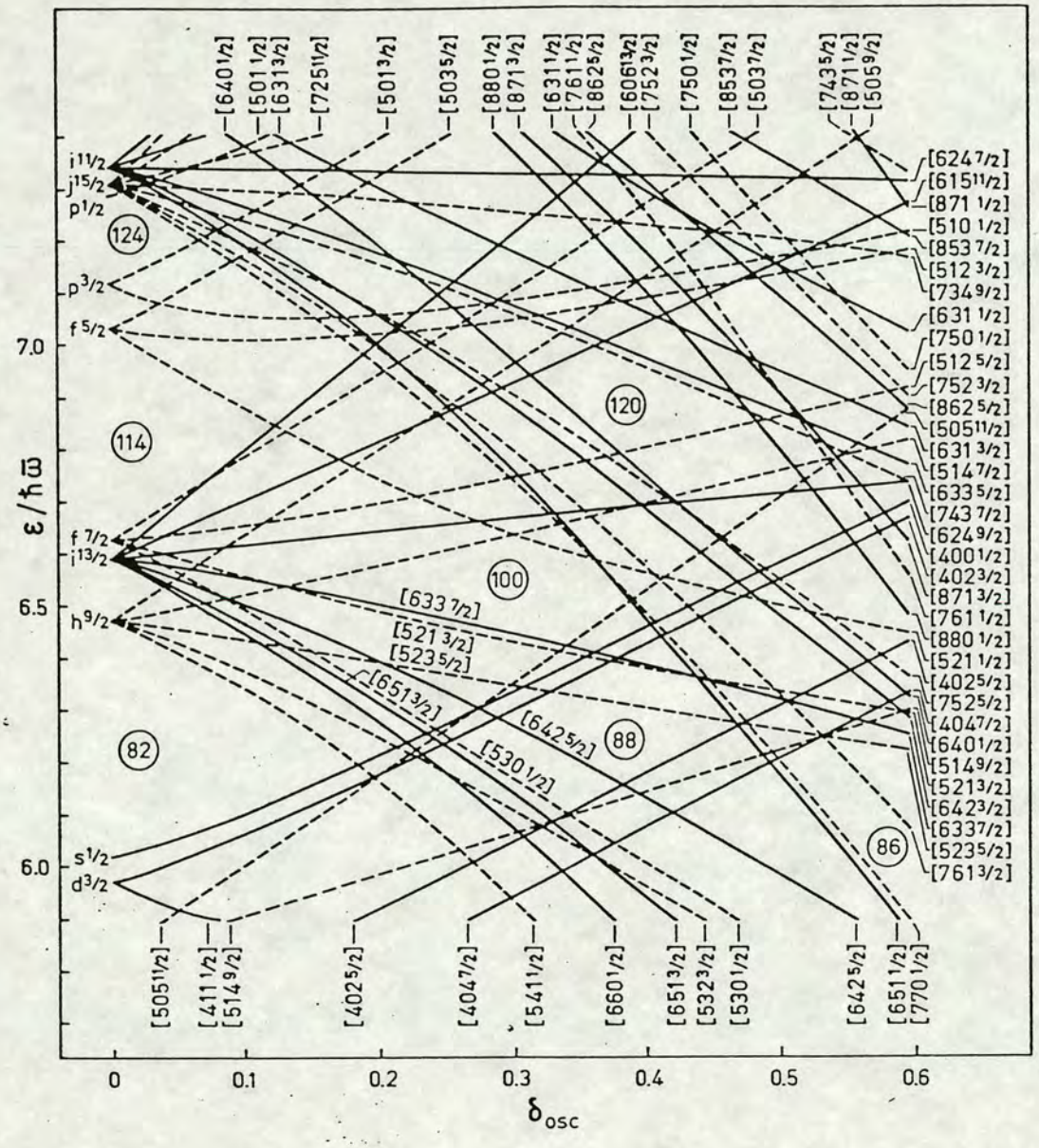

Figure 5.4: Proton single-particle levels.

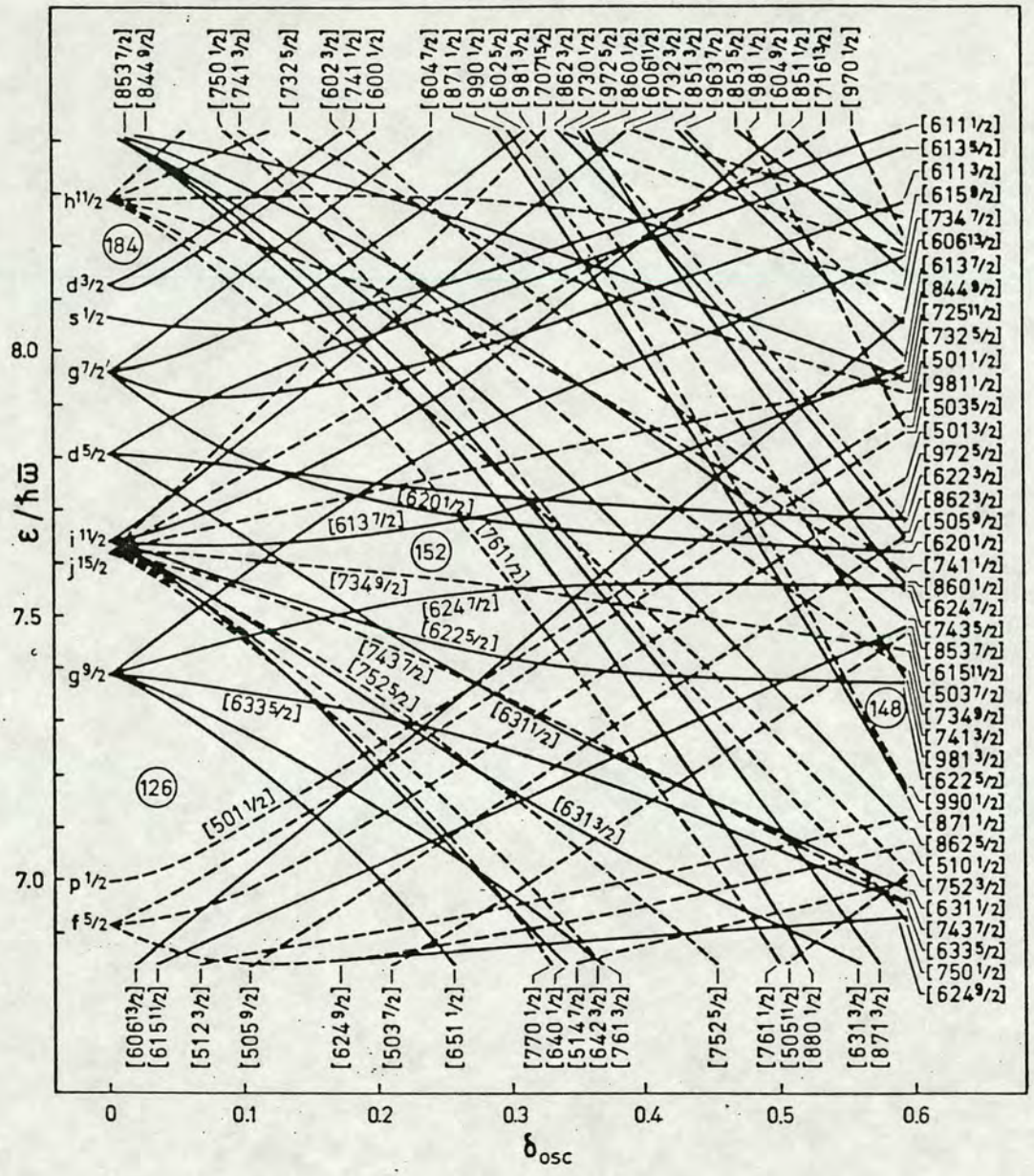

Figure 5.5: Neutron single-particle levels.

Vibration mode		Barrier A (γ-deformed)	Barrier B (octupole-deformed)
"Ground" state	E	0.0 MeV	0.0 MeV
$K = 0$	J^π	$0^+, 2^+, 4^+, 6^+$	$0^+, 1^-, 3^-, 4^+$
γ-vibration(Y_2^2)	E	0.05 MeV	0.7 MeV
$K = 2$	J^π	$2^+, 3^+, 4^+, 5^+$	$2^\pm, 3^\pm, 4^\pm, 5^\pm$
Mass-asymmetric vibration(Y_3^0)	E	0.3 MeV	0.05 MeV
$K = 0$	J^π	$0^-, 1^-, 2^-, 3^-, 4^-, 5^-$	$0^+, 1^-, 2^+, 3^-, 4^+, 5^-$
Bending vibration (Y_3^1)	E	0.9 MeV	0.9 MeV
$K = 1$	J^π	$1^-, 2^-, 3^-, 4^-, 5^-$	$1^\pm, 2^\pm, 3^\pm, 4^\pm, 5^\pm$

Table 5.1: Energies of low-lying even-even fission channels above ground state barrier.

levels E_j are given by:

$$E_j = \sqrt{(\varepsilon_j - \lambda)^2 + \Delta^2} - \Delta, \quad \pi = (-1)^l \tag{106}$$

where ε_j is the single-particle energy for spin j and orbital angular momentum l, λ the Fermi energy and Δ the pairing gap. For ^{241}Am this gives rise to the sequence of levels shown in Fig. 5.6 [Back 90] for the two saddles. Again, for each level there is a rotational band built on with the level acting as a band-head state. One can approximate the low-lying discrete levels using a continuous level density *e.g.* [Lynn 74], however, this significantly underestimates the number of low-lying states as demonstrated in Fig. 5.7 whereby there is a *condensation* of states *i.e.* an increase in states over and above an exponential dependence near zero excitation energy.

5.2.5 Fission Channels Above the Pairing Gap

Once the pairing gap has been exceeded, individual particle excitations give rise to a continuum of channels for even-even and odd-A nuclei. Indeed, for

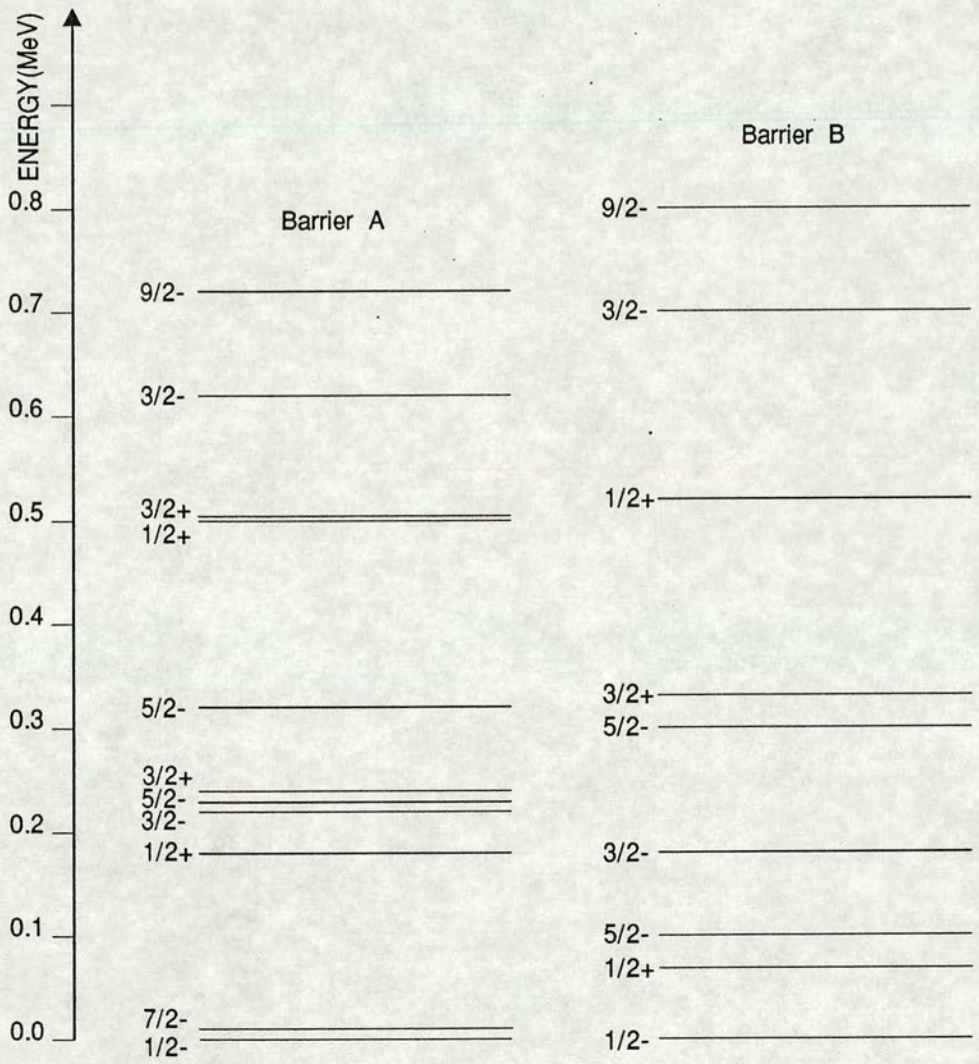

Figure 5.6: Spectrum of fission channels for ^{241}Am.

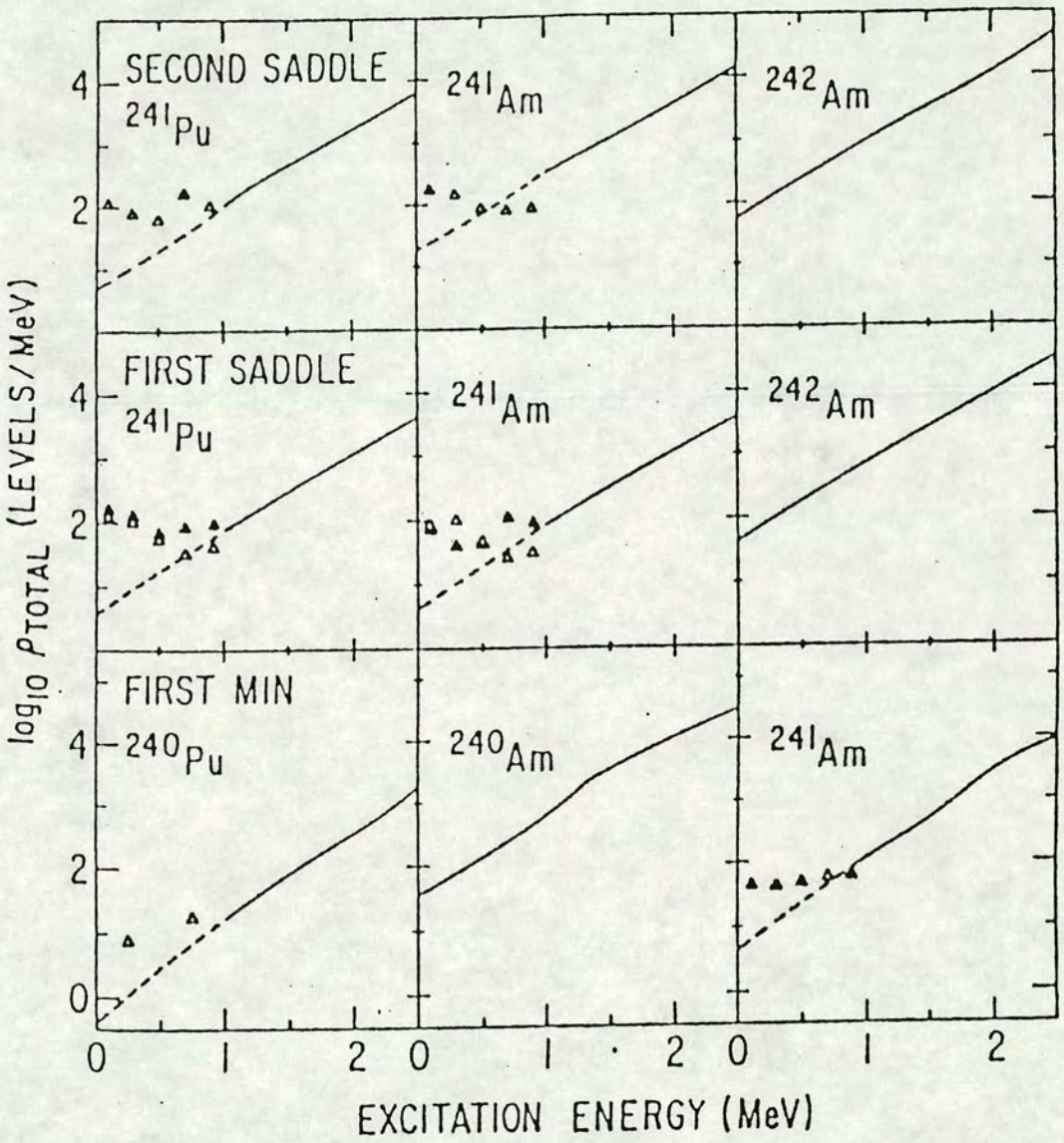

Figure 5.7: Comparison of a continuous level density approximation with discrete low-lying levels for ^{241}Am[Back 74b]. The lines represent a continuous level density approximation whereas the points represent the level density calculated from single-particle states.

odd-odd nuclei, as there is no pairing gap (there already exist two unpaired nucleons) the entire spectrum of states forms a continuum. Therefore, it just remains to find an expression to give the density of states of the various angular momenta in the continuum.

The equation adopted by Lynn [Lynn 74] assumes an exponential increase in states with energy, the nucleus having a fixed nuclear temperature *i.e.*

$$\rho_f(U,J) = (2J+1)\rho_{f_0} \exp^{\frac{-J(J+1)}{2\sigma_b^2}} \exp^{\frac{U}{\theta_f}} \tag{107}$$

where $U = E - \Delta$ (*i.e.* energy above the pairing gap), ρ_{f_0} is a value which depends on the density of states at the pairing gap and barrier $f = A, B$ of the fission channel, θ_f is the nuclear temperature at the each barrier and σ_b is the spin cut-off factor at the barrier height excitation which has approximately a linear dependence on energy *i.e.*

$$\sigma_b = \sigma_{b_0} + \sigma_{b_1} \times E \tag{108}$$

where σ_{b_0} and σ_{b_1} are constants.

5.2.6 A Note on the Addition of Fission Channels

It can be seen from Eq. 103 that any structure resulting from the penetrability of a fission barrier potential will be as a result of the superposition of several fission channels which are labelled ν in this calculation. Each ν corresponds to a different K band such as listed in Table 5.1. For simplicity each K-band or ν fission channel is assumed to have an equal weight. Hence the total fission transmission results from the sum of the direct transmissions of all the fission channels which are added together with equal weight. A more involved calculation might assume a more realistic weighting function for K. Values of K are assumed to be conserved for the direct fission component as this is the simplest method of calculating a transmission function for an individual channel. The damped fission strength which is re-emitted in the form of isomeric fission following γ-decay in the second well is not K conserved but undergoes K-mixing as described in § 5.2.8.

5.2.7 Barrier Penetration

For each fission channel, there is a barrier of a particular shape and height through which the fission wave must quantum-mechanically penetrate. Many authors have calculated penetrabilities for different actinides [Khan 72, Back 71, Back 74a, Brit 72, Cram 70, Lynn 74, Bhan 74].

By convention, the shape of the fission barrier is parameterised using three (or sometimes five if triple-humped) smoothly joined parabolas. Each parabola has a particular curvature and displacement. Hence, to specify a certain double-humped fission barrier requires just six parameters: the heights of the two saddles, the height of the bottom of the second well above the ground state and the curvatures of the saddles and the second well. This, of course, applies to just one fission channel. In general, all these parameters can change for a different channel. Usually, the barrier heights are varied but the curvatures kept constant for each channel. By using a three or five parabola approximation, an exact penetrability can be calculated [Cram 70, Jame 85]. Various other methods have been used to calculate penetrabilities and have been reviewed in an article by Bjørnholm and Lynn [Bjor 80]. For simplicity, the approach adopted in this case is to use an iterative process which can, in principle, be used to calculate transmission through *any* arbitrary shaped barrier, however the interjoining parabola parameterisation has been preserved to allow comparison with other analyses.

The Step-Wise Approximation

To calculate the transmission of a potential step is a relatively easy process and is described in any elementary quantum mechanics textbook *e.g.*[Davi 84]. Such a step is shown in Fig. 5.8.

If the region in step n, between x_{n-1} and x_n has a potential $V(x_n)$, the wave function in this region will be of the form:

$$\psi_n = \alpha_{\rightarrow}(n)e^{ik_n x} + \alpha_{\leftarrow}(n)e^{-ik_n x} \tag{109}$$

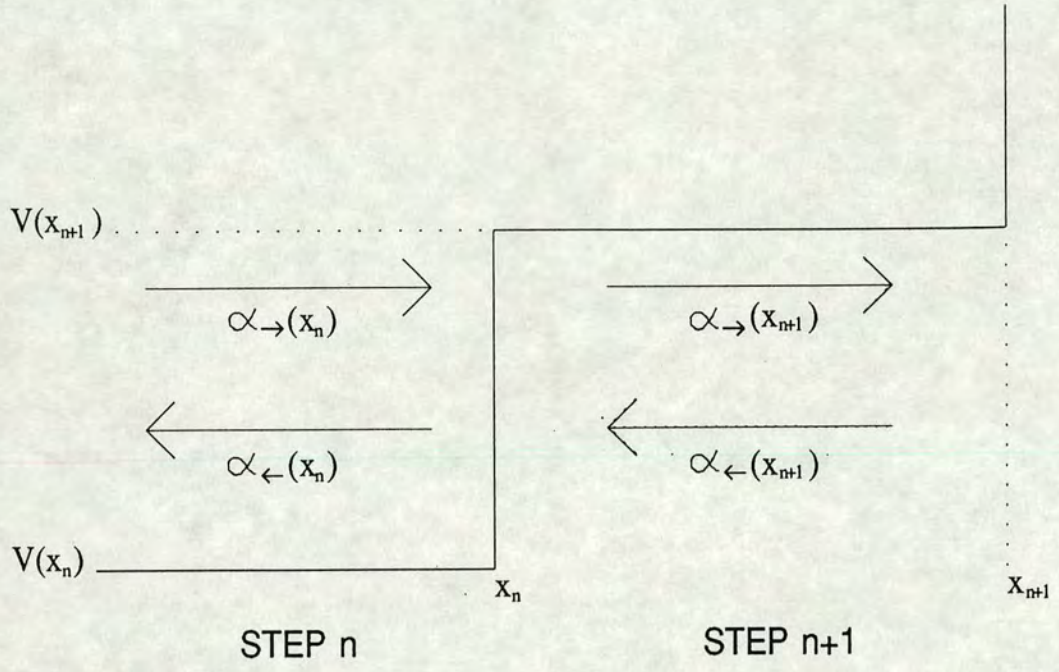

Figure 5.8: A potential step.

where

$$k_n = [2(E - V_n)B/\hbar^2]^{\frac{1}{2}} \tag{110}$$

E being the energy of the wave function and B being the inertial parameter such that $B \approx 0.0540A^{\frac{5}{3}}\hbar^2\,\mathrm{MeV}^{-1}$. $\alpha_{\rightarrow}$ and $\alpha_{\leftarrow}$ are the coefficients of the forward-going (transmitted) and backward-going (reflected) components of the wave function respectively. Similar expressions hold for the region in step $n+1$.

If this is the case, coefficients $\alpha_{\rightarrow}$ and $\alpha_{\leftarrow}$ are given by:

$$\alpha_{\rightarrow}(n) = \frac{(k_n + k_{n+1})\alpha_{\rightarrow}(n+1)e^{ik_{n+1}x_n} + (k_n - k_{n+1})\alpha_{\leftarrow}(n+1)e^{-ik_{n+1}x_n}}{2k_n e^{ik_n x_n}} \tag{111}$$

$$\alpha_{\leftarrow}(n) = \frac{(k_n - k_{n+1})\alpha_{\rightarrow}(n+1)e^{ik_{n+1}x_n} + (k_n + k_{n+1})\alpha_{\leftarrow}(n+1)e^{-ik_{n+1}x_n}}{2k_n e^{-ik_n x_n}} \tag{112}$$

Any arbitrary shaped barrier can be approximated by a series of such steps as shown in Fig. 5.9. If the barrier is split into m such steps then the fraction transmitted is given by:

$$T_{trans} = \frac{\alpha_{\rightarrow}(m)\alpha^*_{\rightarrow}(m)}{\alpha_{\rightarrow}(1)\alpha^*_{\rightarrow}(1)} \tag{113}$$

and the fraction reflected by:

$$T_{refl} = \frac{\alpha_{\leftarrow}(1)\alpha^*_{\leftarrow}(1)}{\alpha_{\rightarrow}(1)\alpha^*_{\rightarrow}(1)} \tag{114}$$

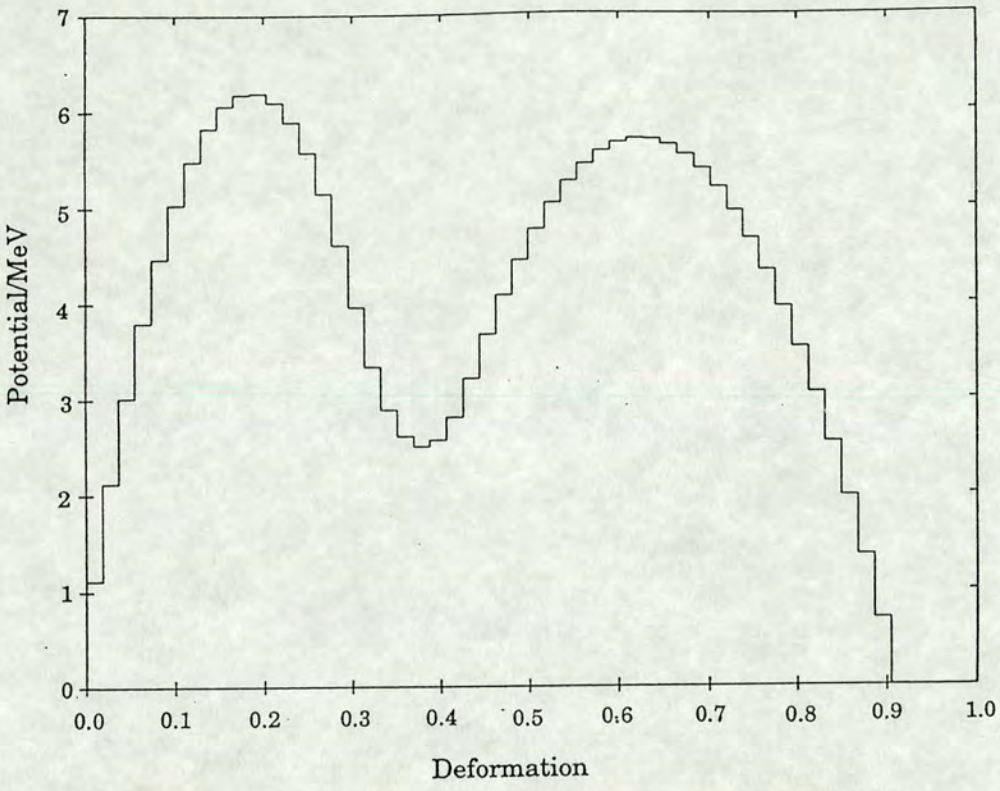

Figure 5.9: Barrier approximated by steps.

(N.B. This assumes that there is no reflected wave to the right of the barrier ($\alpha_{\leftarrow}(m) = 0$), for transmission from left to right and also that the phase velocities at the beginning and end of the barrier are the same.)

5.2.8 Structure in the Cross Section

For the double-humped barrier shown in Fig. 5.10, one obtains the transmission as a function of energy shown in Fig. 5.11 using a 500 step approximation. This transmission results from one fission channel. From now on each fission channel will be labelled ν with angular momentum J, parity π at a specific energy E. One can see quite sharp peaks in the steeply rising transmission coefficient. The peaks seen in the transmission function for the double-humped potential shown in Fig. 5.10 are just an extension of the standing wave or resonance effect observed in a simple square well potential in which standing waves are produced for an integral number

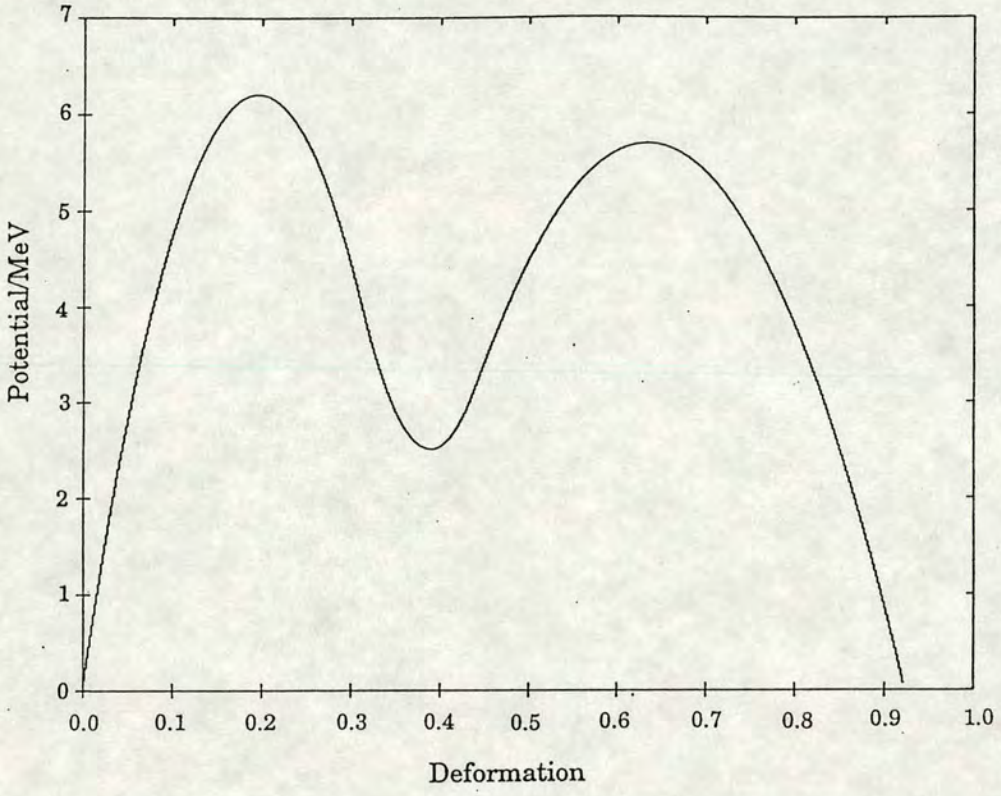

Figure 5.10: A double-humped barrier.

of half wavelengths. This is due to the fact that the fission wave at a particular wavelength (or energy) "fits" into the second well thus giving an increased probability of tunnelling through the second barrier. It is these "quasi-bound" quantum mechanical states which gives rise to the gross structure seen in photofission cross sections for actinides near threshold.

This calculation takes no account of physical nuclear states that might exist at the first and second well deformation other than to emulate their effect in the fission strength "damping" process. This calculation is a one-dimensional calculation and as such is only an approximation. A more complete calculation would include other degrees of freedom such as the effects of the physical nuclear levels but would involve very time consuming and lengthy calculations.

In reality, peaks in fission barrier transmission are not as sharp as shown in Fig. 5.11. This is due to the fission strength becoming damped by

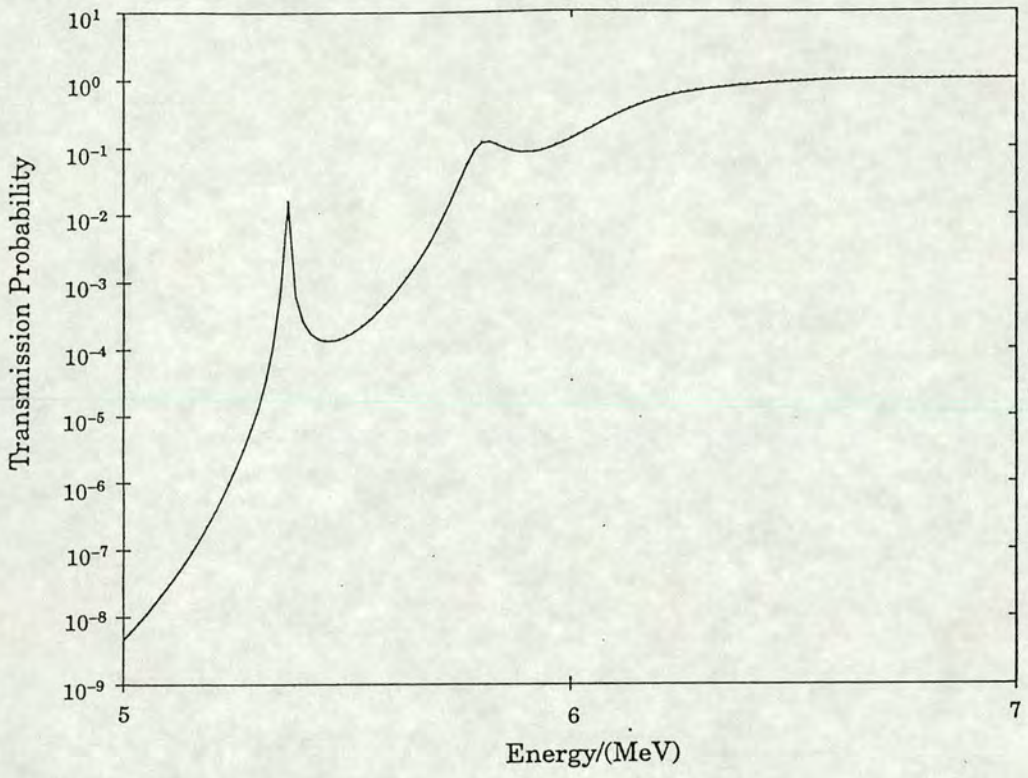

Figure 5.11: Transmission of the barrier in Fig. 5.10.

other modes of decay involving the physical nuclear levels at the second well deformation and the degree of damping depends on the density of levels at that well deformation. An even-even nucleus has fewest levels (for reasons mentioned before *i.e.* all nucleons paired, lowest excitations are few and collective in nature), an odd-A nucleus more and an odd-odd nucleus the most. For this reason the damping will be least for an even-even nucleus and greatest for an odd-odd thus implying that a large amount of structure will be seen for an even-even and increasingly less for an odd-A and odd-odd. This last statement is also true for the reason that more fission channels contribute for an odd-A and odd-odd nucleus than for an even-even nucleus therefore smoothing out these resonant structures.

This "damped" fission strength can appear in the forms shown in Fig. 5.1: it can decay in the second well, decay back to the first well or give rise to isomeric (or delayed fission) following γ-decay in the second well. In this calculation, this damping can be simulated by having a small imaginary

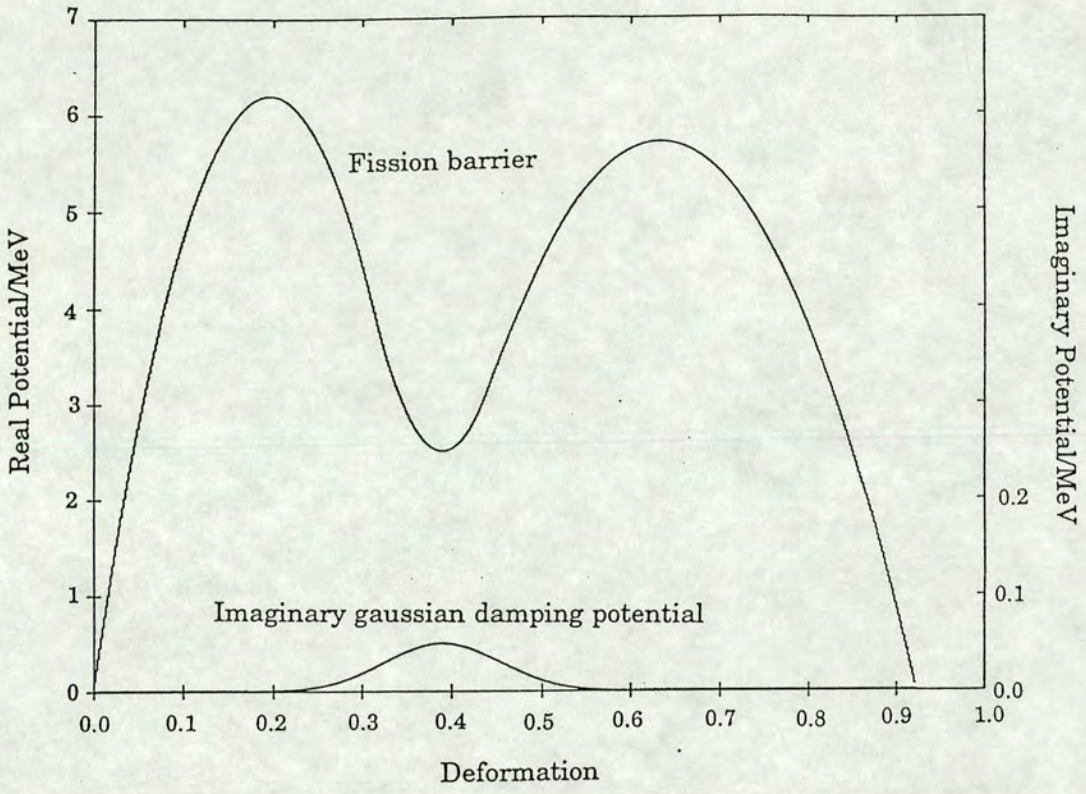

Figure 5.12: Imaginary potential in the second well to emulate damping.

gaussian potential V_{im} acting in the second well (see Figure 5.12) whereby the potential V_n in Eq. 110 becomes a complex number. The magnitude of the damping is assumed to be a linear function of energy such that

$$W_{im} = W_{im0} + W_{im1} \times E \tag{115}$$

with W_{im0} and W_{im1} as real constants and thus the imaginary potential becomes

$$V_{im} = iW_{im} \exp(-[\varepsilon - \varepsilon_0]^2/[2w^2]) \tag{116}$$

where w^2 is the variance of the gaussian in deformation space ε where ε represents deformation along the path of the minimum of the nuclear potential energy surface and ε_0 is the deformation which corresponds to the minimum of the second well.

This gives rise to an absorbed component for each channel $T^{\nu}_{abs}(EJ\pi)$ such that:

$$T^{\nu}_{abs}(EJ\pi) = 1 - T_{trans} - T_{refl} \tag{117}$$

Bondorf [Bond 70] assumed that this absorbed flux can change K value whilst in the second well *i.e.* undergo K mixing, whilst still preserving the quantum numbers J and π so that the total absorbed flux $A(EJ\pi)$ over all channels is given by:

$$A(EJ\pi) = \sum_{\nu} T^{\nu}_{abs}(EJ\pi) \tag{118}$$

The amount of this flux re-emitted back into the fission channel ν as delayed fission is then given by:

$$T^{\nu}_{delayed}(EJ\pi) = A(EJ\pi) \times \frac{T^{\nu}_{outer}(EJ\pi)}{\sum_{\nu}\left[T^{\nu}_{inner}(EJ\pi) + T^{\nu}_{outer}(EJ\pi) + T^{\nu}_{\gamma II}(EJ\pi)\right]} \tag{119}$$

where $T^{\nu}_{inner}(EJ\pi)$ and $T^{\nu}_{outer}(EJ\pi)$ are the transmissions of the inner and outer humps of the fission barrier respectively for the fission channel ν, reflecting the relative probabilities of delayed fission and decay back to the first well. $T^{\nu}_{\gamma II}(EJ\pi)$ is the probability of decay in the second well *i.e.* into *class II* states. This value is often neglected as being small relative to $T^{\nu}_{outer}(EJ\pi)$ and $T^{\nu}_{inner}(EJ\pi)$. For a double-humped barrier with the inner and outer humps approximated by parabolas, $T^{\nu}_{inner}(EJ\pi)$ and $T^{\nu}_{outer}(EJ\pi)$ are given exactly by the Hill-Wheeler formula [Hill 53]:

$$T_{par.\ bar.} = \frac{1}{1+\exp(2\pi(V_{barrier}-E)/\hbar\omega)} \tag{120}$$

where $V_{barrier}$ is the height of the parabolic barrier and $\hbar\omega$ is the curvature of the parabolic barrier for the fission channel ν. For a triple-humped barrier with a small shallow well in the outer hump, $T^{\nu}_{outer}(EJ\pi)$ is given by the formulae for transmission through a double-humped barrier (see Equations 111--113).

The total transmission over all channels ν is now given by:

$$\sum_{\nu} T^{\nu}_{f}(EJ\pi) = \sum_{\nu} T^{\nu}_{trans}(EJ\pi)\,(\text{prompt}) + \sum_{\nu} T^{\nu}_{delayed}(EJ\pi)\,(\text{isomeric}) \tag{121}$$

With a small amount of damping, the peaks in the transmission are smaller and the sub-barrier transmission greater (see Fig. 5.13), indicating the relative importance of isomeric fission in sub-barrier photofission.

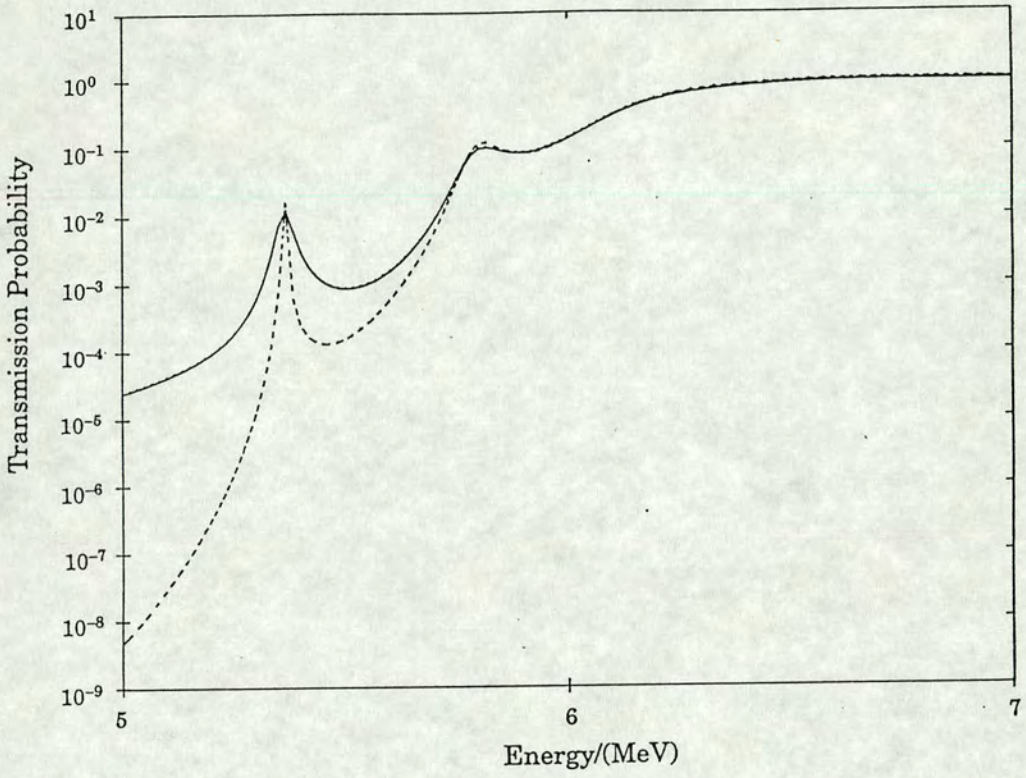

Figure 5.13: Comparison of double-humped barrier transmission with 50 keV damping (full curve) and without damping (dashed curve).

5.2.9 The Complete Damping Limit

In the complete damping limit (for example in an odd-odd nucleus or in the continuum region), the direct component tends to zero *i.e.*

$$\sum_{\nu} T^{\nu}_{trans}(EJ\pi) \rightarrow 0 \tag{122}$$

and the absorbed component becomes the total flux through the first barrier A:

$$\sum_{\nu} T^{\nu}_{abs}(EJ\pi) = \sum_{\nu} T^{\nu}_{A}(EJ\pi) \tag{123}$$

Using the density of states expression from § 5.2.5, the amount of flux transmitted by the first barrier A is given by:

$$\sum_{\nu} T^{\nu}_{A}(EJ\pi) = \sum_{\nu'} T^{\nu'}_{A}(EJ\pi) + \int_{0}^{E-E_A-\Delta} \frac{\rho_A(E-E_A-\varepsilon_k, J)}{1+\exp(-2\pi\varepsilon_k/\hbar\omega_A)} d\varepsilon_k \tag{124}$$

where ν' is summed over discrete states, E_A is the ground state height of barrier A, Δ is the pairing gap and ε_k is the kinetic energy available to the fissioning nucleus. A similar expression exists for the second barrier B. The total fission transmission in the complete damping limit is then

$$\sum_{\nu} T^{\nu}_{f}(EJ\pi) = \frac{\sum_{\nu} T^{\nu}_{A}(EJ\pi) \sum_{\nu} T^{\nu}_{B}(EJ\pi)}{\sum_{\nu} T^{\nu}_{A}(EJ\pi) + \sum_{\nu} T^{\nu}_{B}(EJ\pi)} \tag{125}$$

This expression is used in the continuum region of the nuclides studied in this chapter.

5.2.10 Photon Absorption Cross Section

The photon absorption cross section --- $\sigma_{\gamma a_l}$ in Equation 103 --- is generally approximated by the tail of the giant dipole resonance (GDR) [Axel 62, Know 82], as E1 transitions are the dominant excitations (l=1). Thus, $\sigma_{\gamma a_1}$ is thought to vary smoothly with energy and any structure in the photofission cross section is believed to be due to structure in T_f or T_n. This hypothesis seems to be borne out by experimental work done by Birenbaum *et al.* [Bire 87]. This group determined the photon elastic scattering cross section for ^{238}U. Fig. 5.14 shows the data compared with the extrapolated tail of the GDR, showing relatively good agreement.

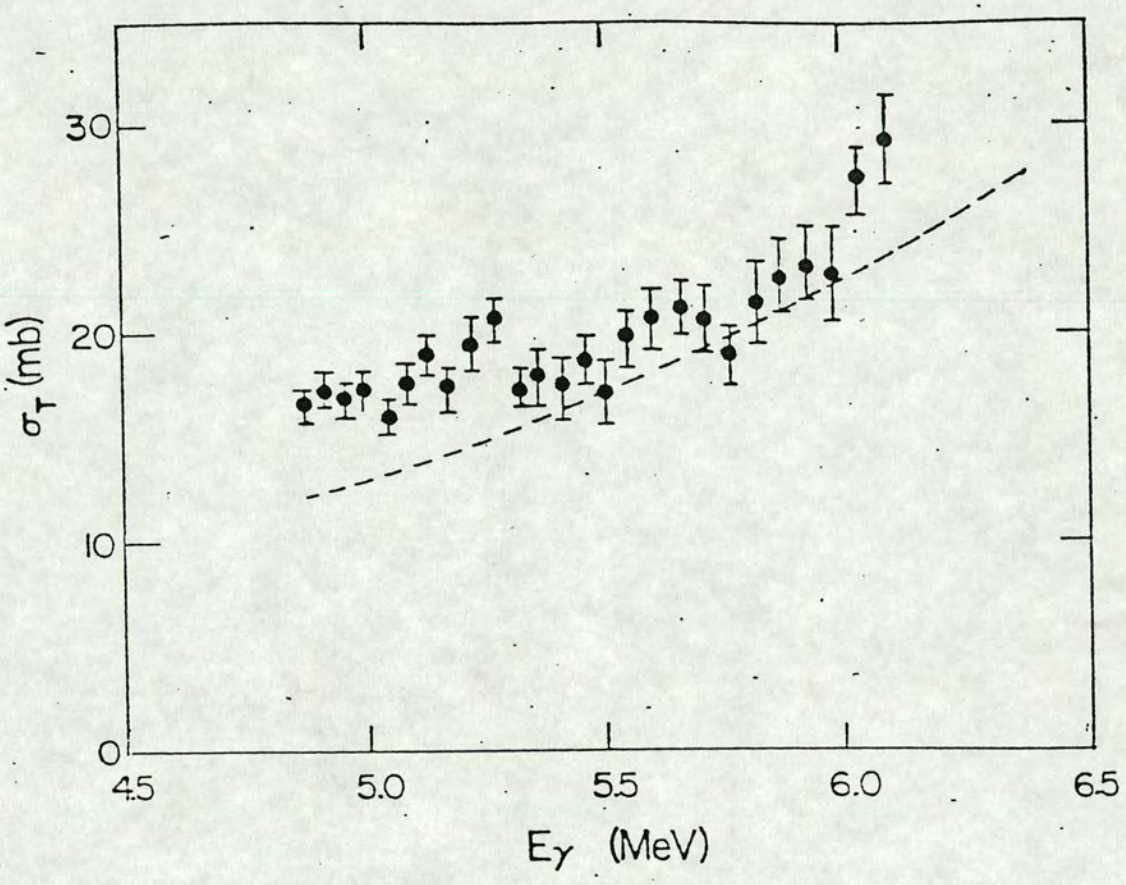

Figure 5.14: The tail of the GDR compared with experimental photon elastic scattering cross section for ^{238}U.

The GDR can be represented approximately by a Lorentzian or double Lorentzian (as in Eq. 98) and at energies well below the peak (*i.e.* at energies around 7 MeV) the photon absorption cross section for E1 absorption is given approximately by [Axel 62]:

$$\sigma_{\gamma a_1} = 5.2(E/7\,\mathrm{MeV})^3(0.01A)^{\frac{8}{3}}\,\mathrm{mb} \tag{126}$$

E2 absorption is assumed to have approximately the same dependence over the energy range studied but a magnitude ~ 0.02 less than for E1 so that:

$$\sigma_{\gamma a_2} \approx 0.02 \times \sigma_{\gamma a_1} \tag{127}$$

5.2.11 The γ Transmission Coefficient

Below the (γ, n) threshold, it can be seen from Equation 103 that T_n will be 0 and the only competition will be between fission and γ emission. Therefore, the low-energy slope of the photofission cross section will depend upon these competing processes.

Neglecting γ decay in the second well, only decay in the first well (*i.e.* decay into *class I*) states will be considered. A first approximation to the transmission function corresponding to γ-decay in the first well, T_{γ_I} is given by

$$T_{\gamma_I} = const \times \varepsilon_\gamma^3 \tag{128}$$

where ε_γ is the energy of the γ ray and *const* is a constant obtained from γ emission strengths obtained from thermal neutron capture on the nucleus $A-1$. This relies on the E_γ^3 dependence of the emission of dipole radiation [Blat 52b].

A more involved expression for $T_{\lambda\gamma}$ (the γ transmission for some compound state λ) is given by Vandenbosch and Huizenga [Vand 73a]:

$$\frac{2\pi < \Gamma_{\lambda\gamma}(E) >}{< D(J,\pi,E) >} \quad \text{or} \tag{129}$$

$$T_{\lambda\gamma}(J,\pi,E) = \underbrace{\frac{2\pi < \Gamma_{\lambda\gamma}(E') >}{< D(J',\pi',E') >}}_{k} \frac{X(E,a_A)}{X(E',a_A)} \frac{\rho(J,E)}{\rho(J',E')} \tag{130}$$

$$X(E, a_A) = x^4 - 10x^3 + 45x^2 - 105x + 105 \quad (131)$$

$$x = 2a_A^{\frac{1}{2}}(E-\Delta)^{\frac{1}{2}} \quad (132)$$

$$\rho(J,E) = C(2J+1)(E-\Delta)^{-2} \exp[2a_A^{\frac{1}{2}}(E-\Delta)^{\frac{1}{2}} - (J+1/2)^2/2\sigma_A^2] \quad (133)$$

where a_A and σ_A are the level density parameter and the spin-cutoff factor for the nucleus of mass A as described by Gilbert and Cameron [Gilb 65] and C is a constant. The quotient k is obtained experimentally from resonant neutron capture whereby the numerator is the average γ emission width and the denominator is the average level spacing for a particular state J', π', E'. Therefore, one can use this expression normalised to the neutron binding energy from resonant neutron capture on the isotope $Z, N-1$ if this feasible, otherwise the normalisation factor, k needs to approximated by theory. The expression in Eq. 131 is used to approximate $\sum_\mu T_\gamma^\mu(EJ\pi)$ assuming dominant dipole γ de-excitation in the first well of the fission barrier.

5.2.12 The Neutron Transmission Coefficient

Above the (γ, n) threshold, one needs to consider the form of the total neutron transmission function which appears in Eq. 103.

Following γ absorption by a nucleus in an initial ground state $J_i\pi$, the nucleus may decay from the excited compound state in the continuum $J\pi$, by emission of a neutron with spin $\frac{1}{2}$, coupling to a state in the residual $A-1$ nucleus $J_f\pi$ to give a particular $T_n^\xi(EJ\pi)$ for the neutron emission channel ξ. This is illustrated in Fig. 5.15. The emitted neutron has orbital angular momentum ℓ. If the initial nucleus has excitation energy E, the residual nucleus has excitation energy $E - \varepsilon_n$ and the neutron has kinetic energy ε_n (neglecting recoil energy of the nucleus which is small compared to the kinetic energy of the neutron from simple kinematic arguments as the mass of the nucleus is over 200 times that of the neutron) then the total neutron

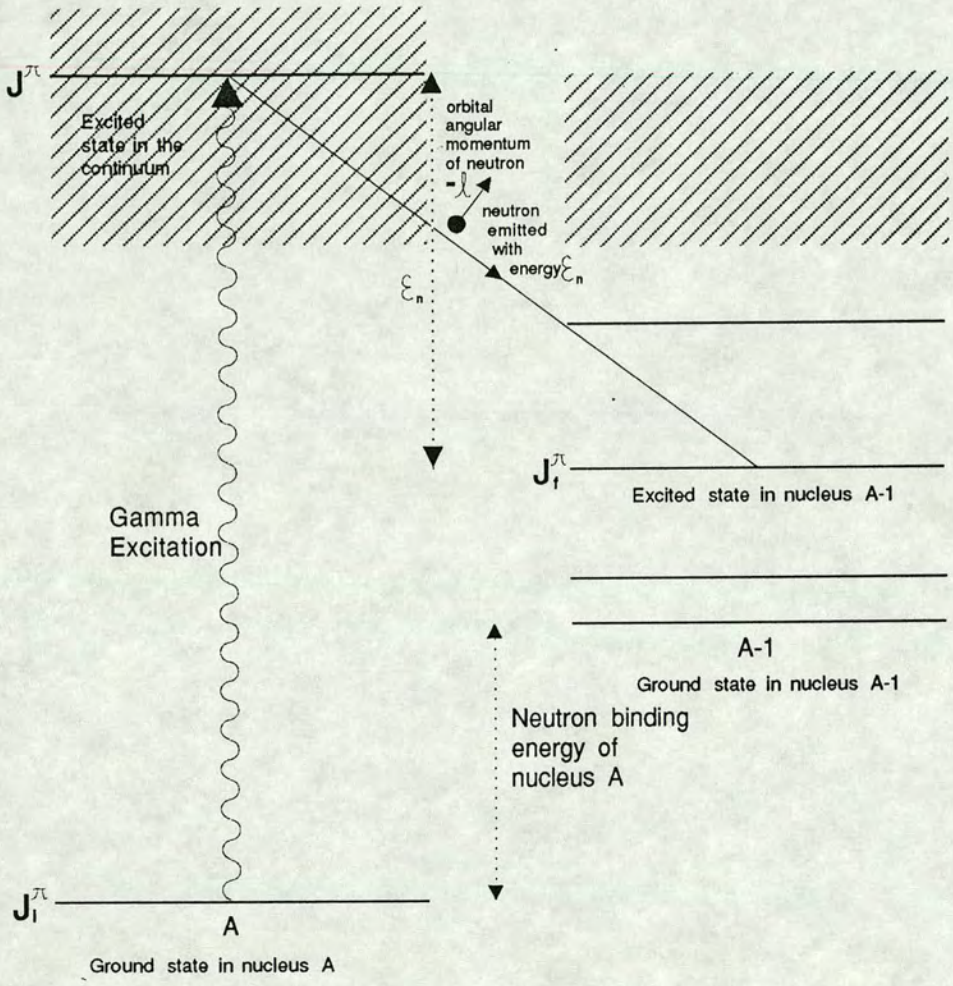

Figure 5.15: Decay of a nucleus of mass A by neutron emission.

transmission coefficient is given by the expression

$$\sum_{\xi} T_n^{\xi}(EJ\pi) = \sum_{\ell=0}^{\infty} \sum_{\kappa} T_\ell(E-E_\kappa) + \sum_{J_f} \int_{\delta}^{E-B_n} \rho^{(A-1)}(E-\varepsilon_n, J_f) \sum_{j=|J_f-1/2|}^{J_f+1/2} \sum_{\ell=|J-j|}^{J+j} T_\ell(\varepsilon_n)\, d\varepsilon_n \tag{134}$$

where the first term sums over all channels κ where angular momentum and parity are conserved for the discrete levels E_κ below the pairing gap in the residual nucleus and the second term sums over the continuum region above the pairing gap *i.e.* at energy δ above the ground state in the residual nucleus. The individual neutron transmission coefficient T_ℓ for a channel κ is calculated from the black nucleus with real square well potential model [Blat 52a] and $\rho^{(A-1)}(E-\varepsilon, J_f)$ is the level density of the residual nucleus of mass $A-1$ at ground state deformation in the continuum region, approximated by an expression given by Gilbert and Cameron [Gilb 65]

$$\rho^{(A-1)}(U,J) = \frac{\sqrt{\pi}}{12} \frac{\exp(2\sqrt{a_{A-1}U})}{a_{A-1}^{1/4} U^{5/4}} \frac{(2J+1)\exp[-(J+\frac{1}{2})^2/2\sigma_{A-1}^2]}{2\sqrt{2\pi}\sigma_{A-1}^3} \tag{135}$$

5.3 Modelling the Cross Sections

This section presents the best fit theoretical cross sections for ^{232}Th, ^{238}U and ^{241}Am. Whilst one should not pretend that these fits are ideal --- indeed several approximations are made to simplify the analysis --- they should nonetheless represent some approximation to the observed cross sections and hopefully give a little insight into the underlying structure.

In the cases of ^{232}Th and ^{238}U photofission the generated cross sections are compared with the Harwell data only. Though there have been a great deal of measurements made of these photofission cross sections, by comparing with Harwell data only, some consistency in the analysis can be obtained and the Harwell data is a good representative sample.

5.3.1 ^{232}Th Photofission Cross Section

Table 5.2 gives the parameters used and Table 5.3 gives the discrete fission barrier heights used to generate the cross section shown in Fig. 5.16

A	$J^{\pi}_{g.s.}$	S_n	$\sigma_A \approx \sigma_{A-1}$	Δ	$a_A \approx a_{A-1}$	$(T_\gamma)^{\dagger}_{eff}$
232	0^+	6.43 MeV	5.45	1.0 MeV	30 MeV^{-1}	1.0

ρ_{A_0}	ρ_{B_0}	θ_A	θ_B	σ_{b_0}	σ_{b_1}
1.6 MeV^{-1}	0.4 MeV^{-1}	0.44 MeV	0.44 MeV	3.4	1.2

Table 5.2: Parameters used to generate the ^{232}Th cross section. †This is the *effective* value of $2\pi < \Gamma_{\lambda\gamma}(6.43\,\text{MeV}) > / < D(2,+,6.43\,\text{MeV}) >$ used to fit the cross section.

K^{π}/MeV	E_A/MeV	E_{II}/MeV	E_B/MeV	$\hbar\omega_A$/MeV	$\hbar\omega_{II}$/MeV	$\hbar\omega_B$/MeV
0^+	5.82	2.00	6.22	1.00	0.90	0.75
0^-	6.12	2.18	6.27	"	"	"
2^+	5.87	2.38	6.92	"	"	"
1^-	6.72	2.90	7.12	"	"	"

W_{im0}/MeV	W_{im1}/MeV	FWHM/ε
-0.03	0.008	0.15

Table 5.3: Fission barriers used to generate the ^{232}Th cross section.

compared with the experimental cross section measured by Findlay *et al.* [Find 86]. The theoretical cross section is very lightly damped and represents effectively infinite experimental resolution.[1] The peaks seen in the generated cross section are marked depending on whether they are due to dipole or quadrupole fission. The dipole transmission is given a weight of 98 % and the quadrupole that of 2 % which represents the approximate ratio of E1/E2 absorption by the target nucleus. Note again that E1 absorption can only excite a 1^- state in the target nucleus and E2 absorption a 2^+ excited state as ^{232}Th has a ground state spin of 0^+.

The energy region between 5.0 and 6.43 MeV represents the competition between fission and γ emission and, assuming all the low-lying fission channels are accounted for, its slope and magnitude can only be adjusted by changing the damping or the value of $2\pi < \Gamma_{\lambda\gamma} > / < D >$. The value

[1] In fact, this is not strictly true due to the use of a 500 step approximation to the barrier.

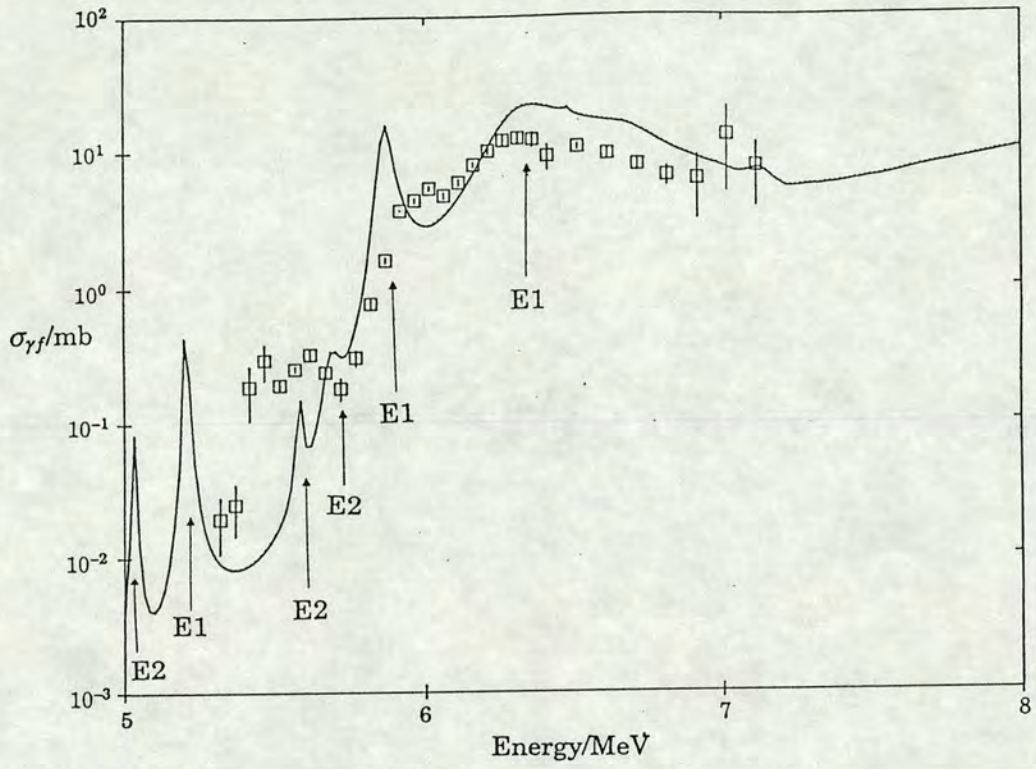

Figure 5.16: The ^{232}Th cross section compared with Harwell data [Find 86].

of this parameter needs to be somewhat higher than that quoted by, for example, Lynn [Lynn 74] who suggested a value of 0.135. The value used is a compromise between achieving the correct magnitude and the correct slope. It is possible that the slope of the γ transmission function is steeper than that calculated using Eq. 131. In fact, Bhandari used a steeper function of energy than that used in this analysis [Bhan 74]. Resonant structure is suggested at 5.55, 5.7, 5.85 and 6.3 MeV and while this is not at the *exact* position of structure in the actual cross section it might conceivably indicate how this structure arises. Slight changes in the barrier parameters could perhaps produce a better fit. The two peaks between 5 and 5.3 MeV are rather large in magnitude and there is no experimental evidence to back them up (recent measurements by Zhang *et al.* [Zhan 86] do not go to low enough energies and neutron capture γ ray measurements by Varhue and Williamson [Varh 87] and Williamson *et al.* [Will 90] are spaced too far apart to show structure). It could in fact be that the theoretical E1 resonance

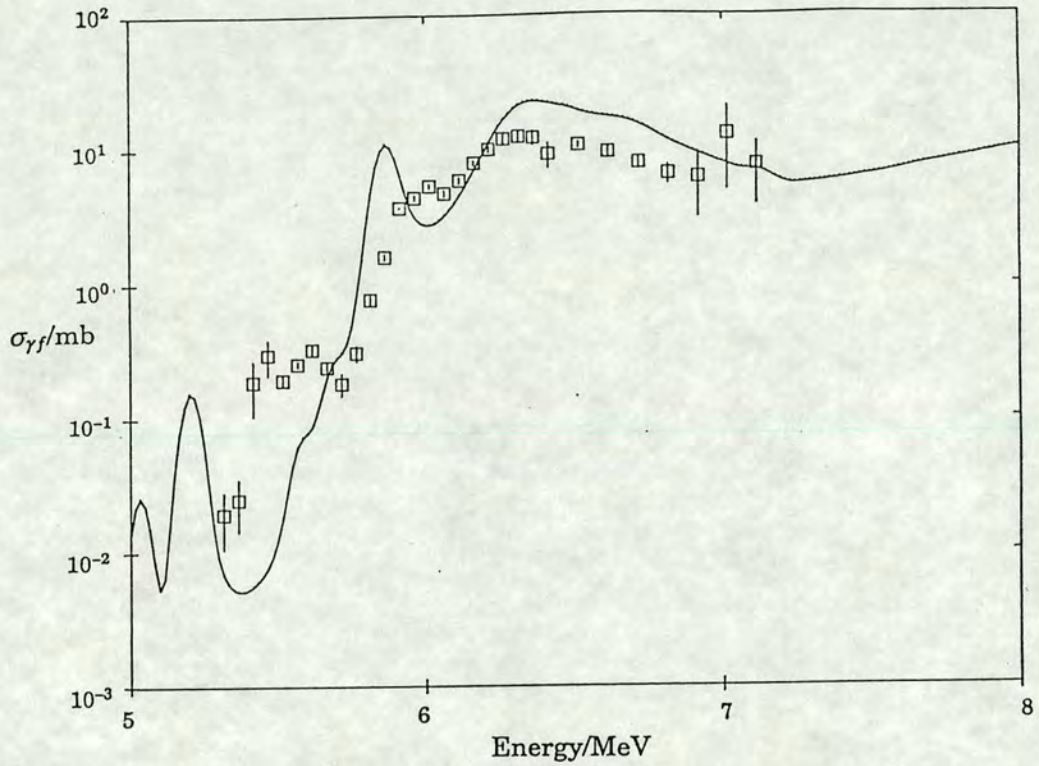

Figure 5.17: As Fig. 5.16 but the theoretical cross section has 80 keV smearing.

at 5.2 MeV should be at 5.5 MeV, as one would expect E2 resonances to be less noticeable in a light actinide where the outer barrier is thought to be somewhat higher than the inner barrier and so any lowering of the outer barrier for E2 fission channels less noticeable. However, reports by Arruda-Neto [Arru 84a, Arru 84b] did indicate a significant E2 strength in the resonances at 5.5 MeV from work done on photofission and electrofission angular distribution data.

Fig. 5.17 shows the same calculated cross section with 80 keV gaussian smearing to represent finite resolution. The smearing simply takes an average over a gaussian function of the theoretical cross section where the gaussian has a FWHM appropriate to the photon resolution. Obviously, the structure becomes less pronounced and only just visible between 5.55 and 5.7 MeV.

Though this is by no means any proof that the observed structure can

A	$J^{\pi}_{g.s.}$	S_n	$\sigma_A \approx \sigma_{A-1}$	Δ	$a_A \approx a_{A-1}$	$(T_\gamma)^{\dagger}_{eff}$
238	0^+	6.15 MeV	5.45	1.0 MeV	30 MeV^{-1}	0.2

ρ_{A_0}	ρ_{B_0}	θ_A	θ_B	σ_{b_0}	σ_{b_1}
1.6 MeV^{-1}	0.4 MeV^{-1}	0.44 MeV	0.44 MeV	3.4	1.2

Table 5.4: Parameters used to generate the ^{238}U cross section. †This is the *effective* value of $2\pi < \Gamma_{\lambda\gamma}(6.15\,\text{MeV}) > / < D(1, -, 6.15\,\text{MeV}) >$ used to fit the cross section.

be accounted for by a double-humped barrier it does demonstrate that the addition of several channels could introduce extra structure into the cross section.

5.3.2 ^{238}U Photofission Cross Section

Table 5.4 gives the parameters used and Table 5.5 gives the discrete fission barrier heights used to generate the cross section shown in Fig. 5.18 in comparison with the Harwell experimental cross section [Hawk 86]. Fig. 5.19 shows the same generated cross section but with 80 keV gaussian smearing. Again this uses a double-humped barrier parameterisation. It does reproduce the resonance seen at 6.1 MeV and also the two peaks observed in the 50 keV resolution data which appear as the broad shelf in the 80 keV resolution data shown in the figure between 5.6 and 5.9 MeV (though not of the correct relative magnitude). However, the slope of the cross section is too steep.

Bhandari and Al-Kharam [Bhan 89] stated that a triple-humped barrier penetrability saturates more slowly than that for a double-humped barrier. The cross section could be made less steep by increasing the damping at the expense of smearing out the structure which is clearly very apparent in the experimental cross section. This suggests that a triple-humped parameterisation is worth investigation.

Between the opening of the (γ, n) threshold and the upper limit of the discrete fission states the cross section dips too much. This might

K^π/MeV	E_A/MeV	E_{II}/MeV	E_B/MeV	$\hbar\omega_A$/MeV	$\hbar\omega_{II}$/MeV	$\hbar\omega_B$/MeV
0^+	5.90	2.00	6.10	1.00	0.90	0.60
0^-	6.20	2.18	6.15	"	"	"
2^+	5.95	2.38	6.80	"	"	"
1^-	6.80	2.90	7.00	"	"	"

W_{im0}/MeV	W_{im1}/MeV	FWHM/ε
-0.03	0.008	0.15

Table 5.5: Fission barriers used to generate the ^{238}U cross section.

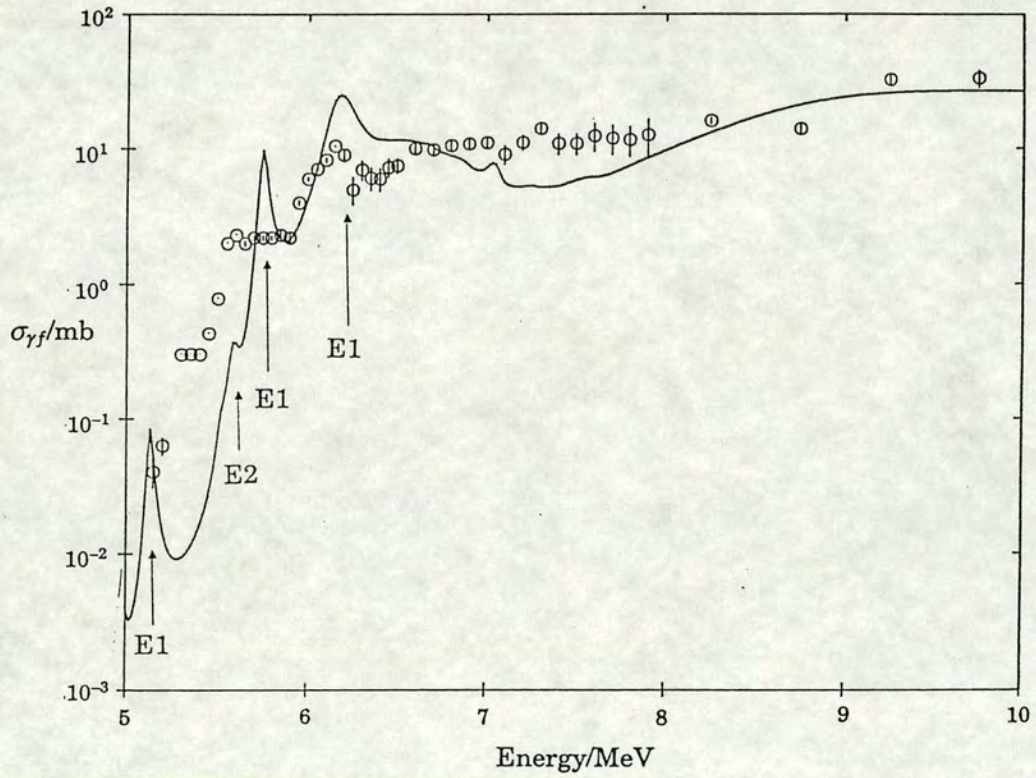

Figure 5.18: The ^{238}U cross section compared with Harwell data [Find 87].

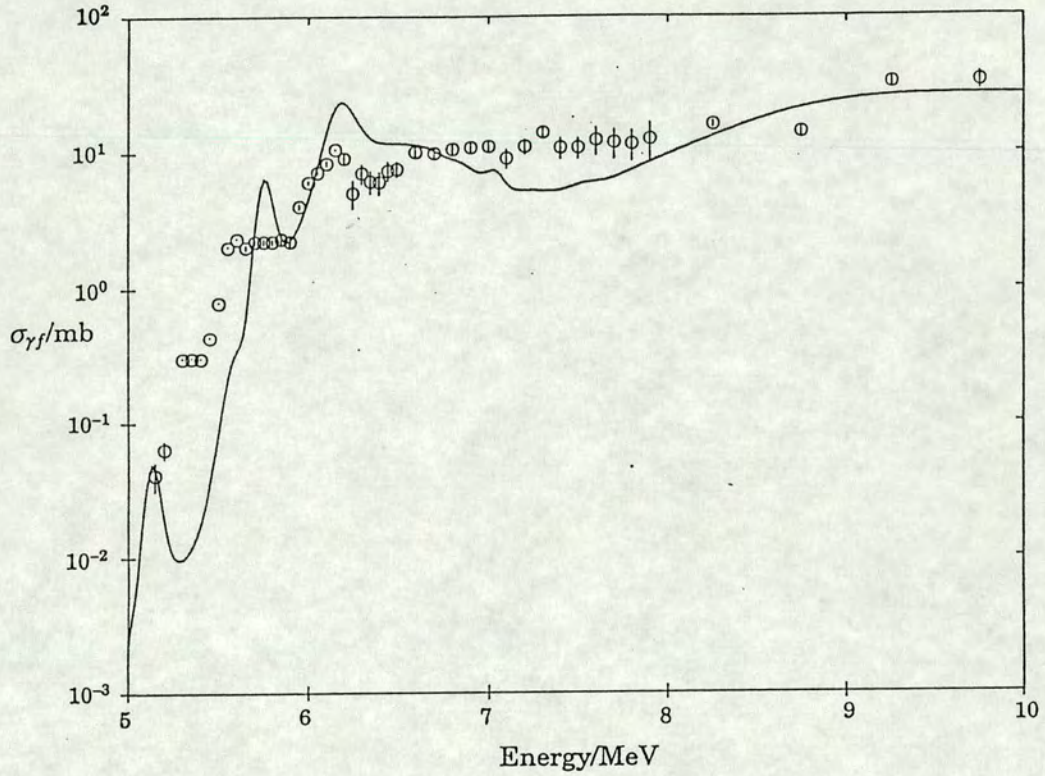

Figure 5.19: As Fig. 5.18 but the theoretical cross section has 80 keV smearing.

A	$J^{\pi}_{g.s.}$	S_n	$\sigma_A \approx \sigma_{A-1}$	Δ	$a_A \approx a_{A-1}$	$(T_\gamma)^{\dagger}_{eff}$
241	$5/2^-$	6.63 MeV	5.45	0.7 MeV	30 MeV^{-1}	0.576

ρ_{A_0}	ρ_{B_0}	θ_A	θ_B	σ_{b_0}	σ_{b_1}
6.8 MeV^{-1}	3.4 MeV^{-1}	0.35 MeV	0.35 MeV	4.1	1.2

Table 5.6: Parameters used to generate the ^{241}Am cross section. †This is the *effective* value of $2\pi < \Gamma_{\lambda\gamma}(6.63\,\text{MeV}) > / < D(3/2, +, 6.63\,\text{MeV}) >$ used to fit the cross section.

possibly suggest further discrete fission channels. However, above 7 MeV, the continuum of fission channels comes into effect. This assumes complete damping whereas the discrete region is only lightly or moderately damped. Also, the present calculation assumes that the fission wave "knows" nothing of the continuum states until the excitation energy is above the discrete region. In reality, the penetrability should be rising faster in this region. Hence, the region where the discrete and continuum fission channels meet is not strictly correct and the change should be smoother with less of a dip.

5.3.3 ^{241}Am Photofission Cross Section

Though it is generally accepted that odd-A and odd-odd nuclides should be modelled using the complete damping model (due to the larger density of states in the second well compared with even-even nuclides), because possible structure is seen in the cross section measured in this experiment, an incomplete damping model is used to model the ^{241}Am cross section as for the two nuclides above.

Table 5.6 shows the parameters used to calculate the theoretical cross section. Table 5.7 shows the discrete fission barriers taken from the quasi-particle states shown in Fig. 5.6. Each K^{π}-band at barrier A was assumed to "link" with the same value of K^{π} at barrier B without crossing another K^{π}-band with deformation. Any state which appears in barrier A but not in barrier B (or *vice versa*) is assumed to have the effect of a single humped barrier whereby the change in deformation forces the state up into the

K^π/MeV	E_A/MeV	E_{II}/MeV	E_B/MeV	$\hbar\omega_A$/MeV	$\hbar\omega_{II}$/MeV	$\hbar\omega_B$/MeV
$1/2^-$	6.200	2.500	5.700	0.80	1.00	0.52
$1/2^+$	6.385	2.628	5.770	"	"	"
$3/2^-$	6.417	2.670	5.882	"	"	"
$5/2^-$	6.428	2.759	5.990	"	"	"
$3/2^+$	6.443	2.671	5.799	"	"	"
$5/2^-$	6.514	2.802	5.990	"	"	"
$1/2^+$	6.704	3.016	6.227	"	"	"
$3/2^-$	6.815	3.157	6.398	"	"	"
$9/2^-$	6.910	3.252	6.493	"	"	"

W_{im0}/MeV	W_{im1}/MeV	FWHM/ε
-0.25	0.065	0.15

Table 5.7: Fission barriers used to generate the ^{241}Am cross section.

continuum region or down below the ground state barrier. Thus in the present analysis they are ignored as they cannot contribute structure to the cross section only magnitude. Fig. 5.20 shows the generated cross section with light to moderate damping and "infinite" resolution, compared with the '88 and '90 data as well as the Zhuchko data down to 5.1 MeV. This does produce a small peak at ~6 MeV due to dipole fission. With 220 keV (see Fig. 5.21) smearing, the peak becomes a change in slope, much as seen in the actual cross section and the slope of the generated cross section agrees with experiment reasonably well though with a smaller magnitude. The peak at ~5.4 MeV is still visible with 220 keV smearing though there seems to be no evidence for such a peak in the Zhuchko data. However, if one examines the Zhuchko data on a compressed energy scale as in Fig. 5.24 there is the suggestion of a change in slope at ~ 5.6 MeV. A similar change in slope exists at 5 MeV. It is probable that this theoretical peak is more greatly damped than calculated here. Fig. 5.22 shows the calculated cross section with increased damping and Fig. 5.23 shows the calculated cross section in Fig. 5.22 with 220 keV smearing. The peak at 5.4 MeV is still

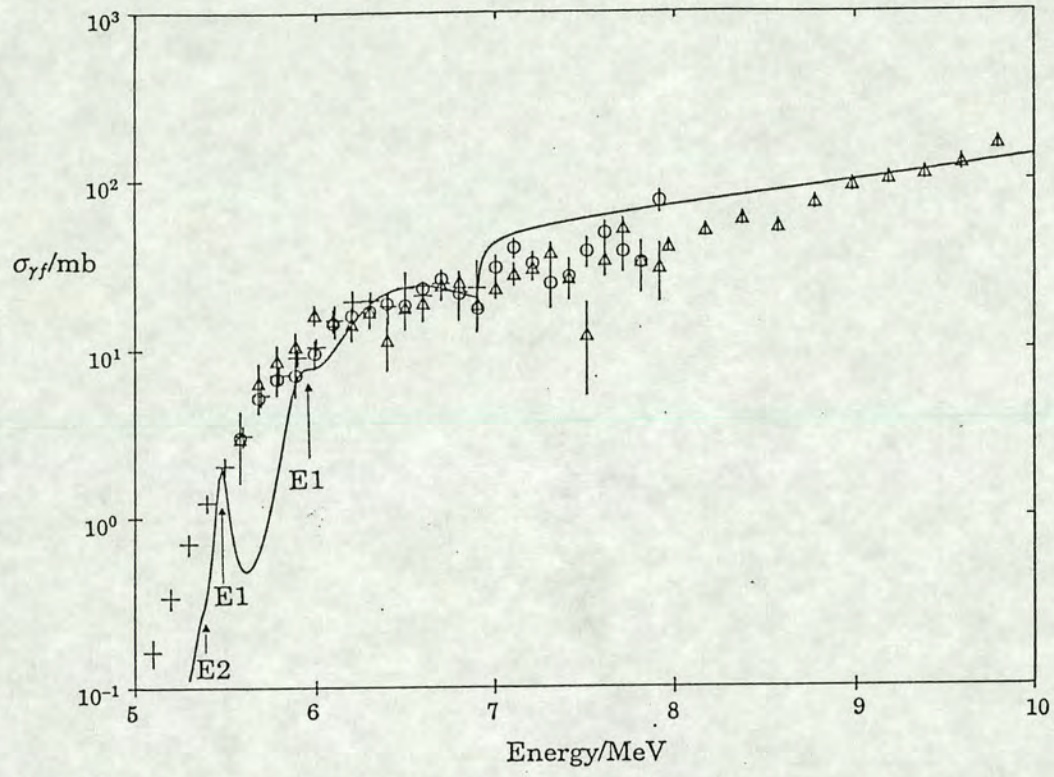

Figure 5.20: The ^{241}Am cross section compared with Harwell '88/'90 data and the Zhuchko data [Zhuc 78].

visible. The change in slope at 6 MeV has almost disappeared which might imply a damping component of between 150 and 300 keV at 6 MeV to see the observed structure in the cross section. So, although there might possibly be a resonance at ~6 MeV, further work would need to be done to confirm this.

Again, similar comments to the ^{238}U cross section apply to the region immediately above the discrete channel region at around 7 MeV. This could be improved if the analysis were to be taken further. Furthermore, the ordering of the quasi-particle states below the pairing gap may be different and if a state at one barrier is shifted significantly more than presumed with deformation this could make a slight difference to the position of structure in the cross section (always assuming that the structure is due to incompletely-damped resonances).

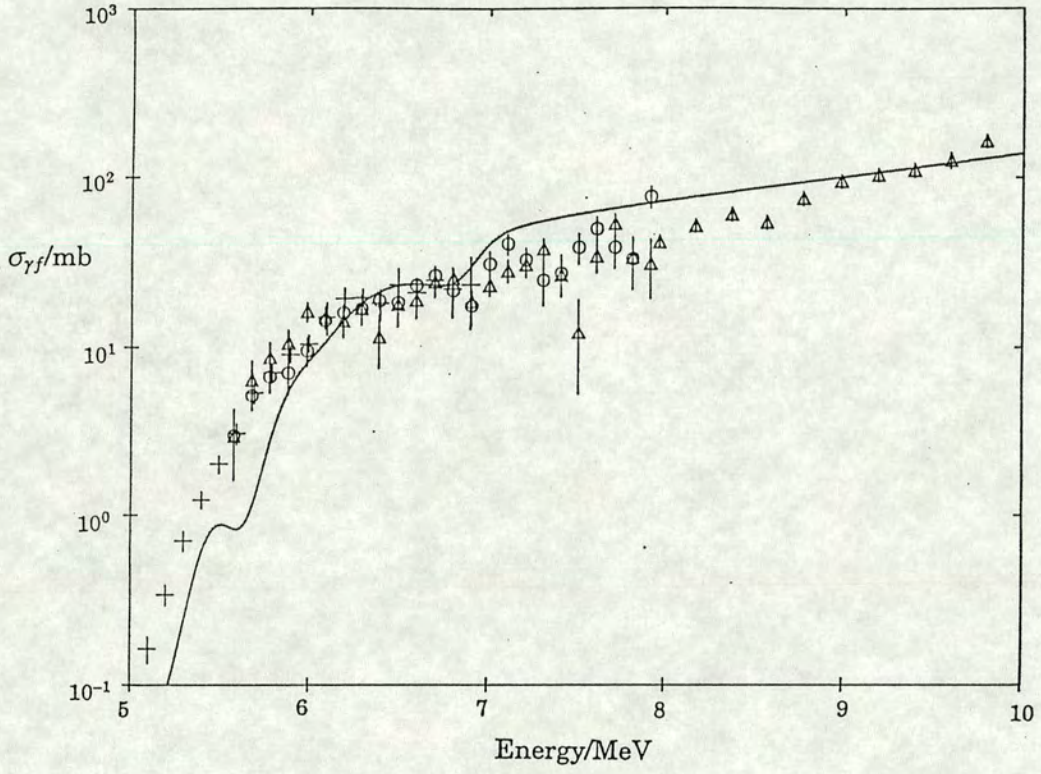

Figure 5.21: As Fig. 5.20 but the theoretical cross section has 220 keV smearing.

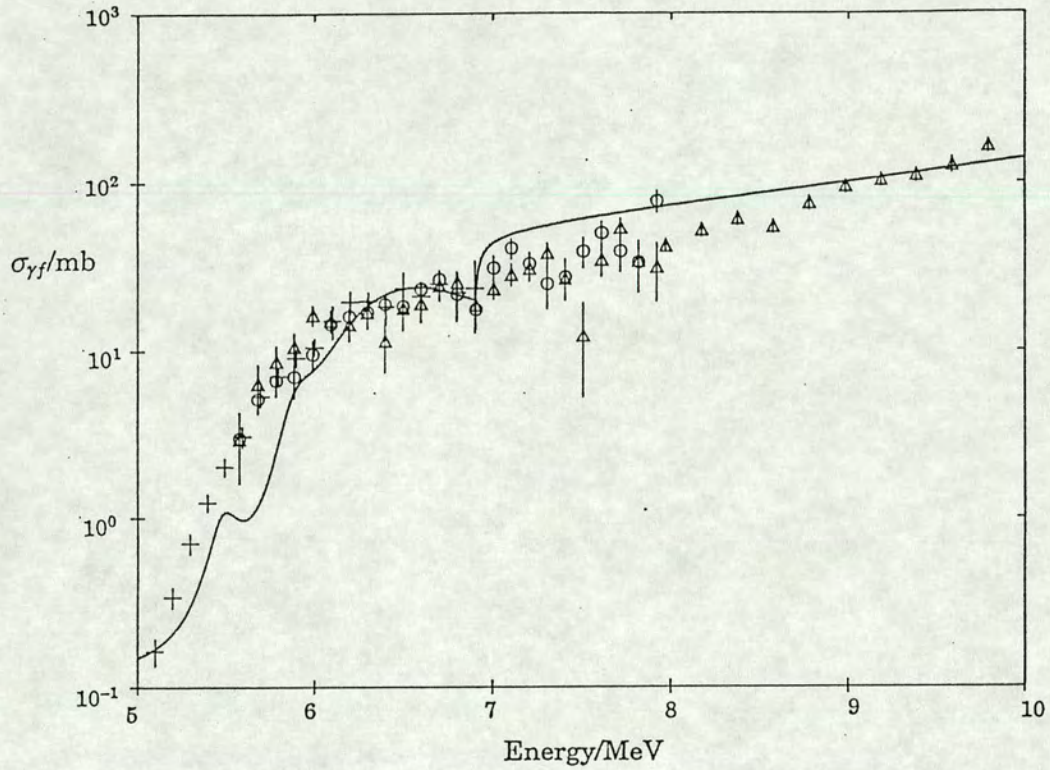

Figure 5.22: As Fig. 5.20 but with uniform damping of 300 keV in the second well (W_{im0}=300 keV, W_{im1}=0 keV).

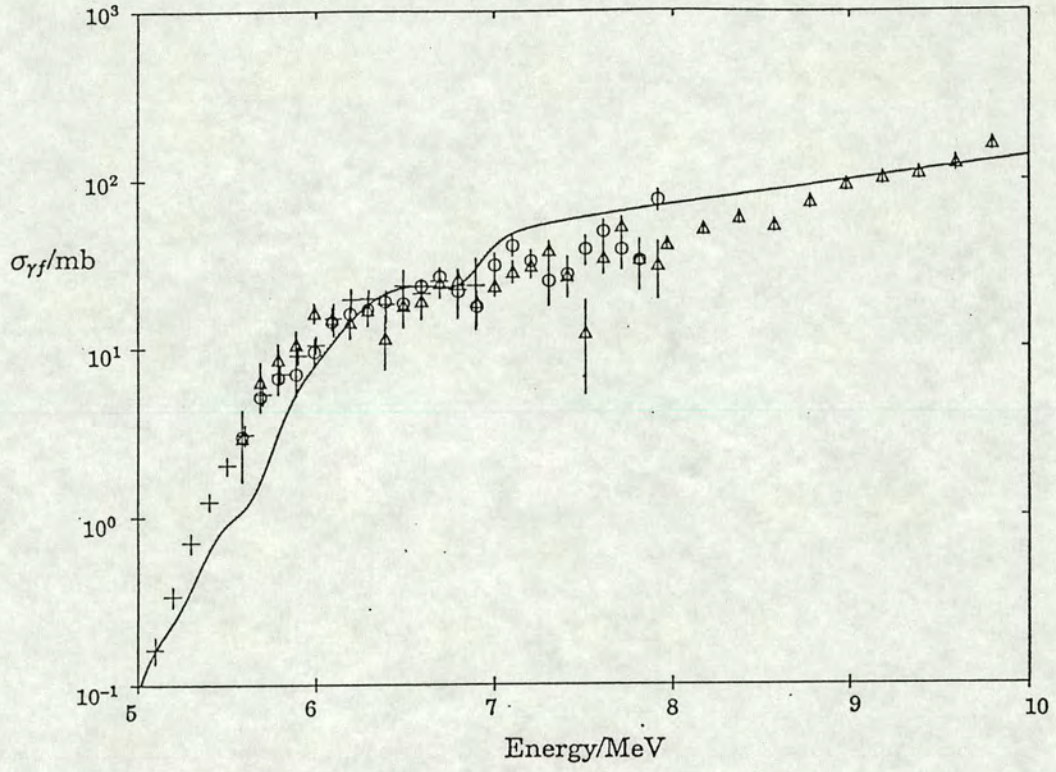

Figure 5.23: As Fig. 5.22 but the theoretical cross section has 220 keV smearing.

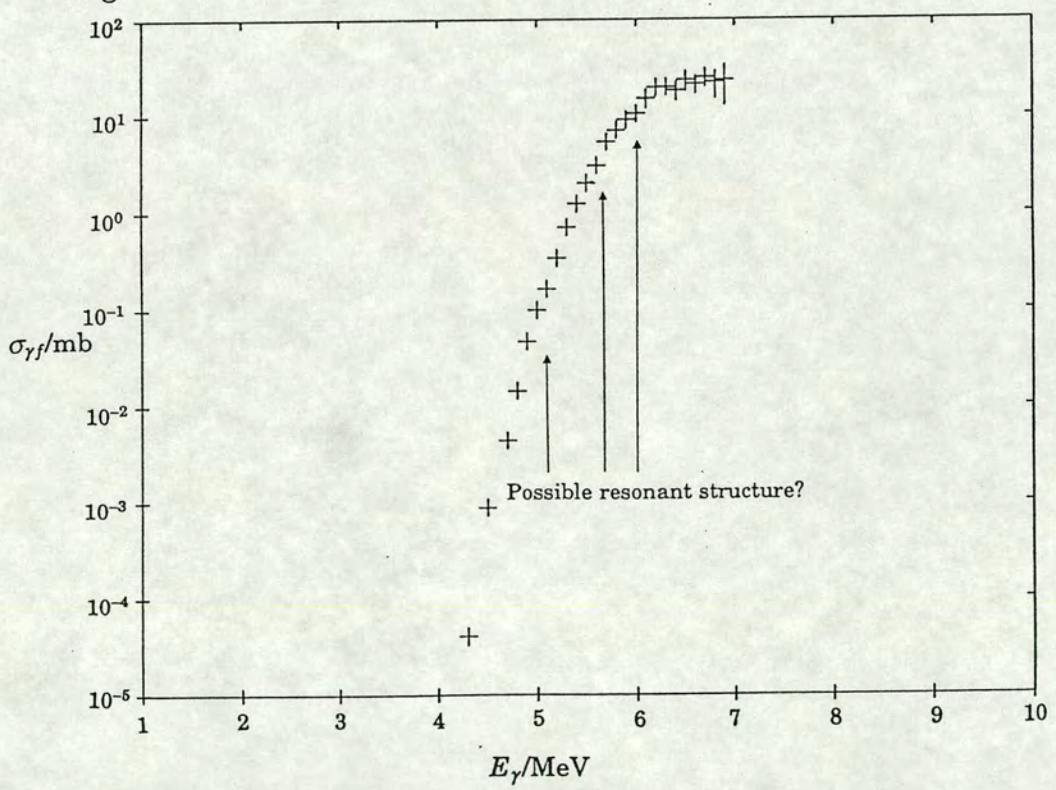

Figure 5.24: *Possible* resonances in the Zhuchko data.

Chapter 6

Conclusions and Discussions

6.1 The Experimental Set-up

The set-up as it stands is able to measure the photofission and photoneutron cross section with fairly good resolution. The photoneutron cross section becomes harder to measure using the multiplicity method if its magnitude is significantly less than that of the photofission cross section. This could obviously be improved with further statistics. On top of this was the large (α, n) contaminant background which degraded the data. This was unavoidable. To measure the photoneutron cross section more accurately would involve detecting fast neutrons in coincidence with both fission fragments and beam pulses which obviously involves an entirely different set-up. To this you have the added problem of the α activity of the target.

In order to measure the cross section at lower energies (maybe even as low as the isomeric shelf region) would require a far more intense beam of photons and/or a variety of available target thicknesses. Assuming the latter is not feasible, this could be achieved by relocating the detector much closer to beam which in turn would require less stringent collimation. An increase in beam flux of up 2 orders of magnitude could be achieved in this way.

To distinguish between contributing fission channels, one could use a polarised bremsstrahlung beam by varying the angle at which the beam

hits the radiator though unfortunately this would also have the effect of cutting down the beam flux.

Using tagged photons could increase the resolution of measurements but this method has the disadvantage of lower intensity than bremsstrahlung without tagging and so would be less useful for sub-threshold and deep sub-threshold measurements.

6.2 The Measured Cross Sections

6.2.1 The Photofission Cross Section

The photofission cross section has been measured in 100 keV steps then interlaced and unfolded to give 220 keV resolution over the range 5.6--10 MeV indicating possible though not statistically significant structure at ~6 MeV which was then re-investigated with 50 keV steps then interlaced and unfolded to give 150 keV resolution. The fine resolution measurements could indicate no definite structure. It would be desirable to measure this region again with still greater resolution and better statistics to see if there is any structure in the ^{241}Am photofission cross section which might be a resonance, or possibly several resonances, resulting from the structure of the barrier. It would also be interesting to see whether there might be structure in the photofission cross sections of other odd-*A* nuclides and high resolution photofission measurements on actinides such as ^{237}Np and ^{239}Pu might help to clarify this. ^{239}Pu has a small ground state spin ($1/2^+$) thus reducing the number of available E1 fission channels. Measurements by Zhuchko *et al.* [Zhuc 78] show structure in the cross section for this nuclide. Berman *et al.* [Berm 86] have measured the photofission cross sections of ^{233}U, ^{237}Np and ^{239}Pu using photons from positron annihilation in flight, reporting a smooth variation with energy over the low energy region (5--10 MeV) However, these measurements were made at too large intervals to hope to see any clear structure and it would have been interesting to repeat these measurements at Harwell with increased resolution and beam flux.

6.2.2 The Photoneutron Cross Section

The photoneutron cross section has been measured from threshold to 10 MeV with 220 keV resolution though due to inherent difficulties, the cross section is not accurate in the range from threshold up to 8 MeV. To increase this accuracy would require better statistics and a purer target sample. A knowledge of the photoneutron cross section allows one to measure the neutron-to-fission branching ratio (Γ_n/Γ_f) with its dependence on the nuclear fissionability Z^2/A. From the low yield 500 keV runs between 8 and 10 MeV, the present data suggest a value of Γ_n/Γ_f of 0.31±0.097. This is plotted as a function of fissionability in Fig. 6.1 compared with other measurements [Berm 86]. Though the other measurements were performed at 11 MeV, the comparison is valid as the neutron-to-fission branching ratio tends to a constant value above about 8 MeV. This can be seen from the equation derived by Vandenbosch and Huizenga [Vand 73c] where the fission barrier and the neutron emission energy are roughly the same. Note that all the measured values above Z^2/A = 36.5 lie above the line. This implies a deviation from a simple exponential decrease in Γ_n/Γ_f with fissionability at higher values of fissionability.[1] Fig. 6.2 shows the present data point plotted against mass number compared with other data [Vand 73b]. There does seem to be good agreement with other Am isotopes. As pointed out in the previous chapter, the fission cross section above the (γ, n) threshold is a result of the competition between fission and neutron emission which in turn is a function of the density of states at the saddle points and the density of states near the ground state of the residual $A-1$ nucleus. Therefore, ultimately, measuring the photoneutron cross section as well as the photofission cross section should help to determine the behaviour of the density of fissioning states at the saddle points.

[1] Berman *et al.* proposed the need for a surface-symmetry correction term to the fissionability to explain this.

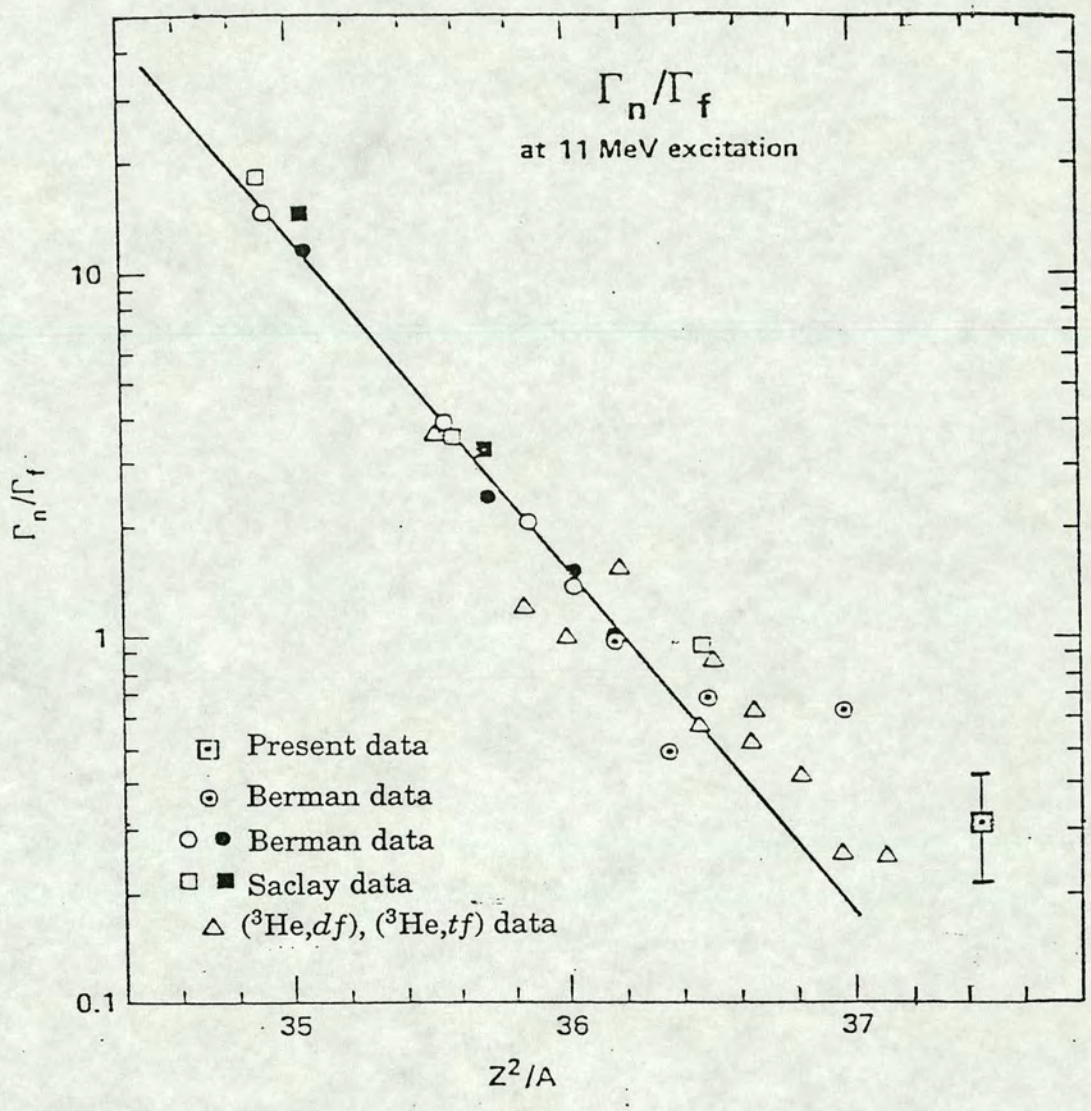

Figure 6.1: Neutron emission to fission width plotted as a function of fissionability. The present data point is an average of data at bremsstrahlung end-points between 8 and 10 MeV.

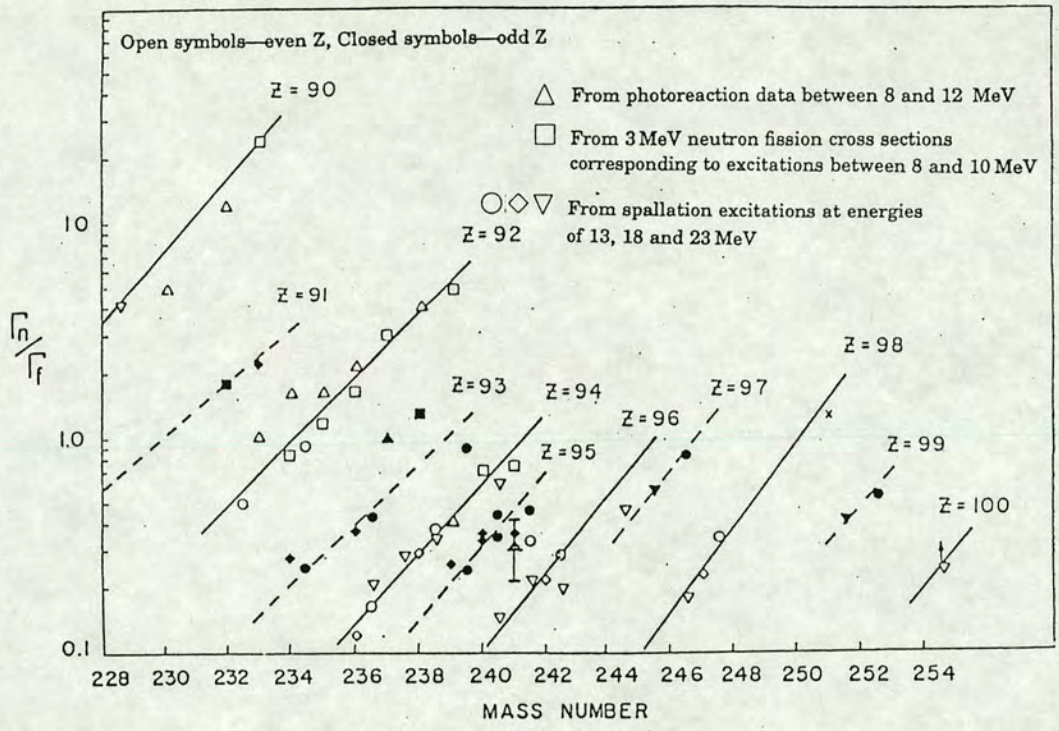

Figure 6.2: Neutron emission to fission width plotted as a function of mass number. The present data point is shown as a solid triangle with error bars.

6.2.3 $\overline{\nu}$

The value of $\overline{\nu}$ has been measured as a function of the average bremsstrahlung energy between 5 and 8 MeV. There appears to be a deviation from a simple linear increase with energy especially at low photon energies. It should be stressed however, that a note of caution was mentioned in the Results chapter about the overall validity of the observed trend after analysis due to difficulties with the analysis. Nevertheless, measurements of other actinides have shown deviations from the expected trend and clearly the kinematics of fission are more complicated than expected from present models. This indicates a need to measure $\overline{\nu}$ with good resolution for a greater number of nuclides to help fill gaps in present understanding.

6.3 Fission Barrier Analysis

More work on the theoretical shape of the fission cross section is required than is allowable within the constraints of writing this report. The present analysis attempted to fit cross sections over several orders of magnitude and as such is bound to expose any failings in the assumed theory. However, the analysis attempted to include all the main features of a full calculation and whilst striving to be physically feasible did not attempt to do this in an unnecessarily complex manner. The following discussion points out failings and improvements that might be made to the theoretical analysis had more time been available.

6.3.1 The Shape of the Fission Barrier

In the present analysis, the shape of the fission barrier was assumed to be double-humped for all the actinides. There has been increasing evidence for a third minimum in the outer barrier of the lighter actinides, and possibly in the inner barrier of the heavier actinides, especially from neutron induced fission experiments (see *e.g.* review by Lynn [Lynn 89]). The analysis could easily be extended to include triple-humped barriers.

The present analysis assumed barriers constructed from parabolic sections to allow parameters from previous analyses to be used. There is no physical reason why the barrier should be shaped thus and the fission barrier might indeed deviate significantly from this simple smooth dependence. By using the stepped barrier approximation, in principle any barrier shape could be analysed --- though the absorption and re-emission of flux would be more complicated --- and the analysis could be extended to investigate the penetrability of barriers obtained from theoretically calculated potential energy surfaces. This might change substantially the shape and/or the position of the peaks observed using the parabolic section parameterisation.

The present analysis assumed that the inertial parameter B is a constant. In reality, this quantity is almost certainly some function of the deformation.

If information were available giving the behaviour of B with deformation then this could be easily included in the analysis. A large variation in B could significantly affect the fission transmission.

Recent literature by Arruda-Neto [Arru 88] and Dias *et al.* [Dias 89] has indicated the possible importance of the Giant Quadrupole Resonance in the fission decay of photo-excited nuclei. If the GQR is greater in magnitude than thought previously, then this might increase the likelihood of E2 resonances in the cross section of *e.g.* ^{232}Th. *However*, care should be taken over this issue as the calculations of Arruda-Neto and Dias involve virtual-photon formalism and the predictions are by no means confirmed.

6.3.2 The Damping of Resonances

In the previous chapter it was assumed that damping increases linearly with excitation energy. This is not unreasonable as a higher excitation energy implies a greater density of states into which the fission wave function can be damped. Whether the damping is simply linear or whether it shows fluctuations with energy is uncertain. Fluctuations in the damping might explain the observed structure in the ^{241}Am cross section though there is no firm evidence to support this.

6.3.3 The Density of States at the Saddle Point and in the Residual $A-1$ Nucleus

The density of states function used when the excitation energy exceeds the discrete state energies is assumed to have an exponential dependence and a constant temperature over a range of about 3--4 MeV. This constant temperature dependence over a limited range is backed up by neutron induced fission of heavy elements. In the case of ^{241}Am particularly, this temperature should probably be a little lower than that quoted by Lynn [Lynn 74] to make the slope of the generated photofission cross section steeper though it is difficult to obtain an accurate value as fitting the best

slope involves changing the values of ρ_{f_0} as well. The fitting of the cross section above the pairing gap of the fissioning nucleus was included for completeness and by no means represents a detailed analysis over this region. Further work could be done to improve this. The value of Γ_n/Γ_f quoted in § 6.2.2 could help to obtain a better fit if further work were to be done on this.

6.3.4 Normalisation of the Calculated Cross Sections

It was pointed out in the Chapter 5 that the magnitudes of the calculated cross sections were not exactly the same as those of the experimental cross sections. Below the (γ, n) threshold the magnitude of the cross section can be adjusted by altering the value of $2\pi < \Gamma_{\lambda\gamma} > / < D >$ in the γ transmission coefficient (see Eq. 131). However, for measured values of this parameter this is not strictly correct. Bhandari [Bhan 74] suggested that the incorrect value of the γ transmission function arises due to the fact that the expression in Eq. 131 takes account only of dipole emission and that there might be evidence for a significant quadrupole emission component. Furthermore, the neutron transmission function seems to be too large in the case of ^{238}U resulting in the dip in the calculated cross section which is not seen in the observed cross section. Back *et al.* introduced normalisation factors G_γ and G_n to multiply the γ and neutron transmission functions respectively in order to get over the difficulties in certain cases of estimating the absolute values of the transmission functions [Back 74b]. The values that they quote for these normalisation factors show a trend whereby G_γ is normally larger than 1 and G_n is normally smaller than 1. This fits in with the present calculations. This is an area that could be looked at if further work were to be carried out.

Appendix A

Tabulations of the Experimental Data

This appendix gives tables of the cross sections plotted in the Results chapter for the convenience of the reader. Both the $\sigma_{\gamma f}$ and the $\sigma_{\gamma n}$ data points quoted are those calculated with both ν_p and W fixed. Note that all errors refer to 1 standard deviation.

A.1 The $\sigma_{\gamma f}$ Cross Sections

The data points quoted for both the 100 keV and 50 keV runs (Table A.1 and Table A.2) are calculated using 2-fold interlacing in the range 5.50 to 7.95 MeV and no interlacing for the 200 keV data points above 7.95 MeV.

A.2 The $\sigma_{\gamma n}$ Cross Sections

The cross section values below 7.95 MeV in Table A.3 have large errors. This is as a consequence of unfolding quite small yield difference values which fluctuate. Small yield difference fluctuations about what are already quite small yield differences are then "amplified" in the unfolding process.

Interlacing is as for the $\sigma_{\gamma f}$ values.

	The '88 100 keV data		The '90 100 keV data	
E_γ/MeV	$\sigma_{\gamma f}$/mb	$\pm\delta\sigma_{\gamma f}$/mb	$\sigma_{\gamma f}$/mb	$\pm\delta\sigma_{\gamma f}$/mb
5.58	2.95	1.35	2.97	0.98
5.68	6.39	1.90	5.14	1.00
5.79	8.62	2.06	6.65	1.37
5.89	10.57	2.17	7.01	1.87
5.99	16.27	2.29	9.50	1.92
6.10	15.10	2.35	14.35	1.74
6.19	14.30	3.14	15.98	1.86
6.29	16.91	3.60	16.88	1.84
6.40	11.43	4.11	18.84	2.41
6.50	17.89	4.91	18.37	2.45
6.60	18.99	4.46	23.24	2.42
6.70	24.33	3.44	26.47	2.63
6.80	25.51	3.35	21.63	2.88
6.90	18.66	2.88	17.47	4.24
7.00	23.21	3.31	30.78	5.76
7.11	28.26	4.48	40.25	5.64
7.21	30.72	5.27	32.56	5.67
7.31	37.78	5.50	24.78	7.34
7.41	26.67	6.65	27.21	7.66
7.51	12.18	6.99	38.52	7.99
7.61	34.37	7.28	49.21	8.74
7.72	52.83	7.54	38.53	9.72
7.82	33.75	8.54	33.09	11.32
7.92	31.15	11.95	76.21	11.80
7.97	41.42	3.12		
8.17	51.31	4.91		
8.37	59.89	6.13		
8.58	53.88	5.52		
8.78	74.26	8.01		
8.98	93.60	9.44		
9.19	102.43	10.12		
9.39	109.53	11.14		
9.59	126.00	14.97		
9.80	163.16	16.38		

Table A.1: The $\sigma_{\gamma f}$ 100 keV data (2-fold interlaced)

A.3 The $\overline{\nu}$ Data

The numbers quoted in Table A.4, Table A.5 and Table A.6 are with W fixed to a linear straight line fit to the data from the previous fit where both ν_p and W were allowed to vary. The data are not unfolded and hence are quoted as a function of mean photon energy. The data are also not interlaced.

E_γ/MeV	$\sigma_{\gamma f}$/mb	$\pm\delta\sigma_{\gamma f}$/mb	E_γ/MeV	$\sigma_{\gamma f}$/mb	$\pm\delta\sigma_{\gamma f}$/mb
5.76	6.54	2.24	6.12	7.48	4.14
5.81	8.88	2.54	6.17	14.19	4.09
5.86	9.76	2.88	6.22	15.71	4.16
5.91	7.78	3.44	6.27	13.62	4.02
5.96	8.45	4.09	6.32	18.20	3.70
6.01	17.77	4.03	6.37	20.09	3.43
6.07	13.42	4.03	6.42	15.59	3.30

Table A.2: The '90 $\sigma_{\gamma f}$ 50 keV data (2-fold interlaced)

	The '88 100 keV data		The '90 100 keV data	
E_γ/MeV	$\sigma_{\gamma n}$/mb	$\pm\delta\sigma_{\gamma n}$/mb	$\sigma_{\gamma n}$/mb	$\pm\delta\sigma_{\gamma n}$/mb
6.60	-12.43	13.52	-8.36	7.17
6.70	-18.06	10.72	-3.65	7.74
6.80	-13.44	10.43	18.20	8.58
6.90	3.02	8.73	26.68	13.02
7.00	8.19	10.27	-15.84	17.45
7.11	3.42	13.54	-41.60	16.15
7.21	3.89	15.70	-9.38	16.32
7.31	-14.18	16.14	18.21	20.86
7.41	-22.23	19.37	22.61	21.15
7.51	38.54	19.83	9.68	23.10
7.61	28.35	21.25	-10.68	24.61
7.72	-0.91	21.24	16.41	27.29
7.82	33.89	24.23	15.78	31.73
7.92	22.86	34.79	-61.48	31.58
7.97	13.04	4.05		
8.17	16.16	5.67		
8.37	18.86	7.26		
8.58	16.97	7.29		
8.78	23.38	9.74		
8.98	29.48	12.18		
9.19	32.26	13.78		
9.39	34.49	15.31		
9.59	39.68	17.87		
9.80	51.38	22.26		

Table A.3: The $\sigma_{\gamma n}$ 100 keV data (2-fold interlaced)

	The '88 100 keV data		The '90 100 keV data	
$\overline{E}_\gamma$/MeV	$\bar{\nu}$	$\pm\delta\bar{\nu}$	$\bar{\nu}$	$\pm\delta\bar{\nu}$
5.53	4.605	1.403	4.260	0.904
5.59	2.931	0.396	3.275	0.283
5.64	3.405	0.397	3.582	0.216
5.69	3.343	0.214	3.385	0.199
5.74	3.042	0.159	3.084	0.162
5.79	3.148	0.100	3.168	0.086
5.85	3.195	0.083	3.098	0.063
5.90	3.232	0.112	3.153	0.052
5.95	3.199	0.079	3.132	0.037
6.00	3.037	0.064	3.128	0.047
6.05	2.994	0.067	3.094	0.073
6.11	3.054	0.098	3.058	0.071
6.16	3.110	0.087	3.154	0.061
6.21	3.148	0.072	3.045	0.061
6.26	3.085	0.049	3.177	0.082
6.31	3.112	0.059	2.928	0.094
6.37	3.074	0.064	3.064	0.063
6.42	3.009	0.065	3.056	0.067
6.47	2.991	0.058	3.091	0.076
6.52	3.042	0.065	2.921	0.060
6.57	2.941	0.055	2.914	0.065
6.63	3.016	0.058	3.073	0.062
6.68	2.946	0.049	3.131	0.066
6.73	2.921	0.056	2.984	0.056
6.78	2.985	0.068		

Table A.4: The 100 keV $\bar{\nu}$ data

$\overline{E}_\gamma$/MeV	$\overline{\nu}$	$\pm\delta\overline{\nu}$	$\overline{E}_\gamma$/MeV	$\overline{\nu}$	$\pm\delta\overline{\nu}$
5.59	3.406	0.234	5.79	3.096	0.082
5.61	3.396	0.275	5.82	3.108	0.069
5.64	3.478	0.175	5.85	3.173	0.061
5.66	3.423	0.171	5.87	3.105	0.049
5.69	3.266	0.193	5.90	3.112	0.038
5.72	3.054	0.158	5.92	3.090	0.028
5.74	3.071	0.107	5.95	3.078	0.024
5.77	3.122	0.105			

Table A.5: The '90 $\overline{\nu}$ 50 keV data

$\overline{E}_\gamma$/MeV	$\overline{\nu}$	$\pm\delta\overline{\nu}$
6.99	3.003	0.096
7.25	3.019	0.058
7.51	3.027	0.059
7.77	3.068	0.050

Table A.6: The '88 $\overline{\nu}$ 500 keV data

Bibliography

[Arru 84a] Arruda-Neto J.D.T. 1984 *Phys. Rev. C* **29** 1905

[Arru 84b] Arruda-Neto J.D.T. 1984 *Z. Phys. A* **315** 247

[Arru 88] Arruda-Neto J.D.T. 1988 *Phys. Rev. C* **37** 1326

[Axel 62] Axel P. 1962 *Phys. Rev.* **126** 671

[Back 71] Back B.B., Bondorf J.P., Otroschenko G.A., Pedersen J. and Rasmussen B. 1971 *Nucl. Phys.* **A165** 449

[Back 72] Back B.B., Britt H.C., Garrett J.D. and Hansen O. 1972 *Phys. Rev. Lett.* **28** 1707

[Back 74a] Back B.B., Hansen O., Britt H.C. and Garett J.D. 1974 *Phys. Rev. C* **9** 1924

[Back 74b] Back B.B., Britt H.C., Hansen Ole, Leroux B. and Garrett J.D. 1974 *Phys. Rev. C* **10** 1948

[Back 90] Back B.B. 1990 private communication

[Bair 79] Bair J.K. and Gomez del Campo J. 1979 *Nucl. Sci. Eng.* **71** 18

[Baro 66] Baron E., Fréhaut J., Ouvry F. and Soleilhac M. 1966 *Nuclear Data for Reactors - Proceedings of a conference on nuclear data - Microscopic cross sections and other data basic for reactors* Vol. II I.A.E.A. (Paris) 57

[Bell 79] Bellia G., Del Zoppo A., Migneco E., Barnà R.C. and De Pasquale D. 1979 *Phys. Rev. C* **20** 1059

[Bell 82] Bellia G., Del Zoppo A., Migneco E., Russo G., Calabretta L., Barnà R.C. and De Pasquale D. 1982 *Z. Phys.* **A308** 149

[Berm 75] Berman B.L. and Fultz S.C. 1975 *Rev. Mod. Phys.* **47** 713

[Berm 86] Berman B.L., Caldwell J.T., Dowdy E.J., Dietrich S.S., Meyer P. and Alvarez R.A. 1986 *Phys. Rev. C* **34** 2201

[Bhan 74] Bhandari B.S. 1974 Ph.D. thesis (unpublished)

[Bhan 89] Bhandari B.S. and Al-Kharam A.S. 1989 *Phys. Rev. C* **39** 917

[Bire 87] Birenbaum Y., Alarcon R., Hoblit S.D., Laszewski R.M. and Nathan A.M. 1987 *Phys. Rev. C* **36** 1293

[Bjor 80] Bjørnholm S. and Lynn J.E. 1980 *Rev. Mod. Phys.* **52** 728

[Blat 52a] Blatt J.M. and Weisskopf V.F. *Theoretical Nuclear Physics* (New York:Wiley) p.361

[Blat 52b] Blatt J.M. and Weisskopf V.F. *Theoretical Nuclear Physics* (New York:Wiley) p.584ff

[Blon 86] Blons J., Fabbro B., Hisleur J.M., Mazur C., Patin Y., Paya D. and Ribrag M. 1986 Fission Meeting, Arcarchon (France) Report No. CEA-DPh-N-S--2399

[Bohr 39] Bohr N. and Wheeler J.A. 1939 *Phys. Rev.* **56** 426

[Bohr 56] Bohr A. 1956 *Proc. Int. Conf. on Peaceful Uses of Atomic Energy* 951

[Bold 76] Boldeman J.W., Bertram W.K. and Walsh R.L. 1976 *Nucl. Phys.* **A265** 337

[Bond 70] Bondorf J.P. 1970 *Phys. Rev. Lett.* **31B** 1

[Brit 72] Britt H.C., Bolsterli M., Nix J.R. and Norton J.L. 1972 *Phys. Rev. C* **7** 801

[Cald 80] Caldwell J.T., Dowdy E.J., Alvarez R.A., Berman B.L. and Meyer P. 1980 *Nucl. Sci. Eng.* **73** 153

[Caru 77] Caruana J., Boldeman J.W. and Walsh R.L. 1977 *Nucl. Phys.* **A285** 217

[Cram 70] Cramer J.D. and Nix J.R. 1970 *Phys. Rev. C* **2** 1048

[Davi 84] Davies P.C.W. 1984 *Quantum Mechanics* (London: Routledge and Kegan Paul) p.39ff

[Dias 89] Dias H., Arruda-Neto J.D.T., Carlson B.V. and Hussein M.S. 1989 *Phys. Rev. C* **39** 564

[Dowd 74] Dowdy E.J., Caldwell J.T. and Worth G.M. 1974 *Nucl. Instrum. Methods* **115** 573

[Edwa 81] Edwards G., Findlay D.J.S. and Lees E.W. 1981 *Ann. Nucl. Energy* **8** 105

[Edwa 82] Edwards G., Findlay D.J.S. and Lees E.W. 1982 *Ann. Nucl. Energy* **9** 127

[Elli 85] Ellis-Akovali Y.A. 1985 *Nuclear Data Sheets* **44** 439

[ENDF **] ENDF/B-V

[Find 83a] Findlay D.J.S. 1983 *Nucl. Instr. Methods* **206** 507

[Find 83b] Findlay D.J.S. 1983 *Nucl. Instr. Methods* **213** 353

[Find 86] Findlay D.J.S., Hawkes N.P. and Sené M.R. 1986 *Nucl. Phys.* **A458** 217

[Find 87] Findlay D.J.S., Hawkes N.P. and Sené M.R. 1987 *Proc. 6th Conf. Capture Gamma-Ray Spectroscopy, Leuven, Belgium, 31st August to 4th September 1987* 693

[Fler 64] Flerov G.N. and Polikanov S.M. 1964 *Compt. Rend. Cong. Int. Phys. Nucl.* (Paris) **1** 407

[Freh 76] Fréhaut J. 1976 *Nucl. Instr. Methods* **135** 511

[Gers 67] Gerstenberg H.M. and Fuller E.C. 1967 *U.S. Department of Commerce --- National Bureau of Standards* NBS 416

[Gilb 65] Gilbert A. and Cameron A.G.W. 1965 *Can. J. Phys.* **43** 1446

[Gold 48] Goldhaber M. and Teller E. 1948 *Phys. Rev.* **74** 1046

[Gust 67] Gustafson C., Lamm I.L., Nilsson B. and Nilsson S.G. 1967 *Arkiv. Fysik* **36** 613

[Hawk 86] Hawkes N.P. 1986 Ph.D. thesis (unpublished)

[Hill 53] Hill D.L. and Wheeler J.A. *Phys. Rev.* **89** 1102

[Jame 85] James G.D. 1985 *Exact Calculation of the Penetrability Through Triple-Hump Barriers* UKAEA Report AERE-R11872, Harwell

[Khan 72] Khan A.M. and Knowles J.W. 1972 *Nucl. Phys.* **A179** 333

[Know 82] Knowles J.W., Mills F.W., King R.N., Pich B.O., Yen S., Sobie R., Watt L., Drake T.E., Cardman L.S. and Gulbranson R.L. 1982 *Phys. Lett.* **116B** 315

[Lanc 84] Lancman H. 1984 Report U.S. Research and Development Administration DOE/ER/10452--13 DE84 006831

[Lars 72] Larsson S.E., Ragnarsson I. and Nilsson S.G. 1972 *Phys. Lett.* **B38** 263

[Lars 74] Larsson S.E. and Leander G. 1974 *Physics and Chemistry of Fission,* Proceedings of a conference at Rochester (IAEA, Vienna), Vol. 1 p.177

[Lees 78] Lees E.W. and Lindley D. 1978 *Ann. Nucl. Energy* **5** 133

[Lees 80] Lees E.W., Patrick B.H. and Bowey E.M. 1980 *Nucl. Instrum. Methods* **171** 29

[Lisk 77] Liskien H. and Paulsen A. 1977 *Atomkernenergie* **30** 59

[Lynn 74] Lynn J.E. 1974 *Systematics for Neutron Reactions of the Actinide Nuclei* UKAEA Report AERE-R7468, Harwell

[Lynn 89] Lynn J.E. 1989 *Proceedings of the Conference:* "Fifty Years with Nuclear Fission" Vol. I p.418 (Gaithersburg, Maryland, U.S.A. April 25--28, 1989)

[Meit 39] Meitner L. and Frisch O.R. 1939 *Nature* (London) **143** 239

[Moll 70] Möller P. and Nilsson S.G. 1970 *Phys. Lett.* **B31** 283

[Moll 72] Möller P. 1972 *Nucl. Phys.* **A192** 259

[Myer 69] Myers W.D. and Swiatecki W.J. 1969 *Ann. Phys.* (New York) **55** 395

[Myer 77] Myers W.D. 1977 *Droplet Model of Atomic Nuclei* (IFF/Plenum, New York)

[Ohsa 84] Ohsawa T., Shigemitsu Y., Masao O. and Kazuhiko K. 1984 *J. Nucl. Sci. Technol.* **21** 887

[Owen 82] Owen J.G., Weaver D.R. and Walker J. 1982 *Proc. Int. Conf. Nuclear Data for Science and Technology, 6^{th} to 10^{th} September 1982, Antwerp* 492

[Pash 69] Pashkevich V.V. 1969 *Nucl. Phys.* **A133** 40

[Penf 59] Penfold A.S. and Leiss J.E. 1959 *Phys. Rev.* **114** 1332

[Poli 62] Polikanov S.M., Druin V.A., Karnauchov V.A., Mikheev V.L., Pleve A.A., Skobelev N.K., Subotin V.G., Ter-Akapian G.M. and Formichev V.A. 1962 *Zh. Eksp. Teor. Fiz.* **42** 1016

[Powe 64] Powell M.J.D. 1964 *Comput. J.* **7** 155

[Prui 62] Pruitt J.S. and Domen S.R. 1962 *U.S. Department of Commerce --- National Bureau of Standards* NBS 48

[Rayl 78] Rayleigh J.W. 1878 *Proc. London Math. Soc.* **10** 4

[Rudi 86] Rüdinger E. and Peierls R. 1986 *Nucl. Phys.* **9** "Niels Bohr Collected Works"

[Schu 71] Schultheiss H. and Schultheiss R. 1971 *Phys. Lett.* **B34** 245

[Stru 67] Strutinsky V.M. 1967 *Nucl. Phys.* **A95** 420

[Terr 57] Terrell J. 1957 *Phys. Rev.* **108** 783

[Tsen 79] Tseng H.K. and Pratt R.H. 1979 *Phys. Rev.* **A10** 1525

[Vand 73a] Vandenbosch R. and Huizenga J.R. 1973 *Nuclear Fission* (New York: Academic Press) p.122

[Vand 73b] Vandenbosch R. and Huizenga J.R. 1973 *Nuclear Fission* (New York: Academic Press) p.227

[Vand 73c] Vandenbosch R. and Huizenga J.R. 1973 *Nuclear Fission* (New York: Academic Press) p.232ff

[Vanp 84] Vanpraet G. 1984 private communication

[Varh 87] Varhue W.J. and Williamson T.G. 1987 *Appl. Radiat. Isot.* **38** 561

[Wald 81] Waldo R.W., Karam R.A. and Meyer R.A. 1981 *Phys. Rev. C* **23** 1113

[Will 90] Williamson T.G., Lamaze G.P., Gilliam D.M. and Eisenhauer C.M. 1990 *Nucl. Sci. Eng.* **104** 46

[Zhan 84] Zhang H.X., Yeh T.R. and Lancman H. 1984 *Phys. Rev. Lett.* **53** 34

[Zhan 86] Zhang H.X., Yeh T.R. and Lancman H. 1986 *Phys. Rev. C* **34** 1397

[Zhuc 78] Zhuchko V.E., Ostapenko Yu. B., Smirenkin G.N., Soldatov A.S. and Tsipenyuk Yu. M. 1978 *Sov. J. Nucl. Phys.* **28** 602